


12-2018

Examining the Use of Idealized Granular Material in Validated DEM Simulations

Anjana Thoroppady Kittu
University of Arkansas, Fayetteville

Follow this and additional works at: <https://scholarworks.uark.edu/etd>

 Part of the [Civil Engineering Commons](#), and the [Geotechnical Engineering Commons](#)

Recommended Citation

Thoroppady Kittu, Anjana, "Examining the Use of Idealized Granular Material in Validated DEM Simulations" (2018). *Theses and Dissertations*. 3042.

<https://scholarworks.uark.edu/etd/3042>

This Dissertation is brought to you for free and open access by ScholarWorks@UARK. It has been accepted for inclusion in Theses and Dissertations by an authorized administrator of ScholarWorks@UARK. For more information, please contact scholar@uark.edu, ccmiddle@uark.edu.

Examining the Use of Idealized Granular Material in Validated DEM Simulations

A dissertation submitted in partial fulfillment
of the requirements for the degree of
Doctor of Philosophy in Engineering

by

Anjana Thoroppady Kittu
Mahatma Gandhi University
Bachelor of Technology in Civil Engineering, 2007
Oklahoma State University
Master of Science in Civil Engineering, 2013

December 2018
University of Arkansas

This dissertation is approved for recommendation to the Graduate Council.

Michelle L. Bernhardt-Barry, Ph.D., P.E.,
Committee Chair

Richard A. Coffman, Ph.D., P.E., P.L.S.
Committee Member

Paul Millett, Ph.D.
Committee Member

Clinton M. Wood, Ph.D., P.E.
Committee Member

ABSTRACT

Discrete element method (DEM) modeling, is becoming widely used for understanding the micro-mechanical behavior of granular materials at the particle level. This dissertation presents important considerations regarding the experimental boundary conditions and idealized granular materials used in DEM validations.

A common issue in DEM validation studies for direct shear and direct simple shear is selecting top and bottom cap boundary conditions that allow for shear transmission while also being efficiently modeled in the DEM simulations. While the traditional grid boundary types used in the laboratory can be replicated in the numerical models, researchers have also used fixed-particle boundaries, sawtooth boundaries, and high friction boundaries with no projections. To examine any effects from these boundaries at the macro-scale, direct shear tests on physical specimens of dense and loose sand, and dense and loose steel ball bearings were conducted. The influence of friction on the boundary was further examined at the particle scale using two simple DEM simulations replicating the physical steel ball bearing specimens with a high and a low friction coefficient on the top and bottom boundaries. The DEM stress-displacement responses are compared to the laboratory results for tests using the boundary plates with no projections and then the particle-scale results of the validated simulations are analyzed.

In addition to boundary effects, the idealized materials used in validation studies were also examined. Commonly used steel ball bearings or glass ballotini restrict the direct comparison of DEM simulations to spherical particles, thus limiting understanding of real materials with more complex shapes. This study shows that additive manufacturing (AM) can be used to create analogue soils with a variety of shapes which can be used for DEM validations. The AM particles were characterized to ensure their suitability for laboratory testing and to

determine the material properties to input into future DEM models. The second part of the dissertation describes the determination of material properties and surface characteristics of two AM materials. Because a Hertzian contact law is typically used in DEM models, a comparison of the materials' response under uniaxial compression and the theoretical response for Hertzian behavior was carried out.

DEDICATION

This thesis is dedicated to my loving husband, Vivek Kuttappan and my sweet little girl, Dhwani

Vivek.

ACKNOWLEDGEMENT

First and foremost, I would like to thank Dr. Michelle Bernhardt for offering me an opportunity to work with her and the valuable feedback and guidance provided to me throughout the research. Apart from the tremendous academic support, I greatly value the personal rapport that Dr. Bernhardt and I have forged over these four years. I am thankful to my wonderful committee members, Dr. Richard Coffman, Dr. Clint Wood and Dr. Paul Millett, for their feedback and support throughout the process. Their wisdom and advice has made me a better geotechnical engineer. I would also like to thank Dr. Ignazio Cavarretta, for his time and guidance for the research collaboration. I would like to thank my friend and colleague Matthew Watters, for his friendship and help in research. I thank Anibal Santos, for his friendship and help, and being a listening ear regardless of his busy schedule. I would like to acknowledge Behdad Mofarraj, Everton Vincente, Ana Bernado for their help in the lab during the summer semesters. I would like to express my gratitude to Chris Boyd, for the technical support for the computers. I would like to thank University of Arkansas for the financial support provided for this research. I am thankful for the High-Performance Computing Center (HPCC) at the University for providing me with the resources required to run the simulations for this research. I am grateful to Dr. Pawel Wolinski for answering my ten thousand emails about LIGGGHTS. I would like to acknowledge Steve Geer, for his help in coding with LIGGGHTS.

I would like to thank Rohit Kumar, a friend and a fellow graduate student at Purdue University for his valuable input about coding. I thank my Friends, Sruthi Mantri and Spandana AnnamRaju, for their moral support and positive energy throughout my graduate student life. I greatly appreciate their words of encouragement during the stressful times. I owe a great deal to my husband, Vivek Kuttappan, for his love, appreciation and care all these years and setting the

standards so high! I am forever grateful to my beloved daughter, Dhvani Vivek, and I can't thank her enough for the unconditional love and the little notes she left me every day on my desk. I express my deepest gratitude to my family, mother-in-law and late father-in-law for their encouragement and prayers. Above all, I thank God for giving me the health and strength to pursue my goals and keep going when harder times came and guiding me to the successful completion.

TABLE OF CONTENTS

CHAPTER 1: INTRODUCTION.....	1
1.1 Background and Motivation for Research	1
1.2 Research Hypothesis and Objectives	4
1.3 Dissertation overview.....	5
CHAPTER 2: LITERATURE REVIEW	6
2.1 Granular material behavior and discrete element method (DEM) modeling	6
2.2 Overview of DEM modeling.....	8
2.2.1 Hertz Mindlin contact model.....	11
2.2.2 Methods for specimen preparation in DEM	13
2.3 Direct shear	19
2.3.1 Previous experimental direct shear studies.....	19
2.3.2 Previous Direct shear DEM Studies	23
2.4 Additive manufacturing of granular material.....	28
2.5 Characterizing Idealized Granular Material.....	32
CHAPTER 3: EXPERIMENTAL EVALUATION OF THE INFLUENCE OF DIRECT SHEAR BOUNDARY TYPES ON GRANULAR MATERIAL RESPONSE.....	37
3.1 Introduction	37
3.2 Verification tests on sand specimens with metal and AM grid inserts	42
3.3 Response of dense sand specimens	46
3.4 Response of loose sand specimens.....	51
3.5 Response of dense ball bearing specimens	55
3.6 Response of loose ball bearings	59
3.7 Conclusions	62
CHAPTER 4: DEM DIRECT SHEAR VALIDATION STUDY	65
4.1 Introduction	65
4.2 Specimen preparation.....	65
4.3 Results and discussions	70

4.3.1 Comparison of overall behavior of specimens with experimental data	70
4.3.2 Micro-scale analysis of DEM specimens	73
4.3.3 Contact force network	78
4.4 Conclusions	79
CHAPTER 5: CHARACTERIZATION OF ADDITIVE MANUFACTURED PARTICLES FOR DEM VALIDATION STUDIES.....	81
5.1 Introduction	81
5.2 Specimen preparation.....	82
5.3 Determination of Poisson’s ratio, surface roughness and hardness	84
5.4 Results and discussion.....	87
5.4.1 Shape parameters	87
5.4.2 Surface characteristics	89
5.4.3 Material properties.....	94
5.5 Conclusions	102
CHAPTER 6: CONCLUSIONS	104
6.1 Summary	104
6.2 Recommendations for future work.....	107
REFERENCES.....	109
Appendix A. AM Material Characterization Data	115
CURRICULUM VITAE.....	127

LIST OF FIGURES

Fig 1.1 Bonded spheres and rods (a) Yan and Ji, 2009, (b) Itasca, 2015.....	3
Fig. 2.1 Shear banding (Wang, et al., 2007)	8
Fig. 2.2 Steps in the calculation phase of DEM simulations	9
Fig. 2.3 Hard particle and soft particle approach in DEM.....	10
Fig. 2.4 Components of Hertz contact model (Itasca consulting Group, 2014)	13
Fig. 2.5 Steps in the elimination of overlaps in the specimen preparation (Jodrey and Tory (1979; 1985)	14
Fig. 2.6 (a) The general progression of the algorithm; (b) unstable and (c) stable position of a new particle (Bagi, 1993).....	14
Fig. 2.7 Schematic of the closed form algorithm (Feng et al., 2003)	15
Fig. 2.8 Schematic of open form algorithm	16
Fig. 2.9 (a) Preparation of initial front for the inward packing method in a 3D assembly by placing the particles along the outer boundaries and (b) final front, (Bagi, 2005)	16
Fig. 2.10 (a) Pluviation of spheres to create a granular assembly for direct shear test.....	18
Fig. 2.11 Dense specimen preparation by moving the walls inwards.....	18
Fig. 2.12 Dense specimen preparation by radius expansion of particles	18
Fig. 2.13 Direct shear device (www.tankonyvtar.hu).....	20
Fig. 2.14 Influence of aspect ratio on determination of friction angle (Cerato and Lutenegeger (2006)).....	22
Fig. 2.15 Hryciw and Irsyam (1993).....	23
Fig. 2.16 DEM and experimental data compared by Ni et al. (2000).....	25
Fig. 2.17 Direct shear test by Yan and Ji (2009)	26
Fig. 2.18 2D simulation of sawtooth boundary with glass ballotini for direct shear testing (Wang, Dove, & Gutierrez, 2007)	27
Fig. 2.19 Shear banding (Wang, Dove, & Gutierrez, 2007)	27
Fig. 2.20 Side view of PBBJ printing process (https://all3dp.com/)	29
Fig. 2.21 Examples of applications of AM in geotechnical engineering	30
Fig. 2.22 (a) Comparison of printed and simulated grains (Hanaor et. al, (2016)) (b) Models of Bonded spheres, (Miskin and Jaeger (2013))	31

Fig. 2.23 Definition of Feret diameters (Cavarretta, 2009)	33
Fig. 2.24 (a) Viker's indenter (b) Indentation made on a specimen (c) Plastic zone.....	36
Fig. 3.1 Particle size distribution of (a) Ottawa 20-30 sand, and (b) steel ball bearings	38
Fig. 3.2 Schematics of the AM boundaries (a) grid plate (R1.5) (b) wide spaced grid (R4.8) (c) grid plate with taller projections (T1.5) (d) wide grid plate with taller projections (T4.8) (e) sawtooth (S) (f) fixed particles (F).....	40
Fig. 3.3 Photographs of printed boundaries (a) regular grid plate (R1.5) (b) AM grid plate (c) sawtooth (d) wide grid plate with taller projections (T4.8) (e) grid plate with taller projections (T1.5) (f) fixed particles (F).....	42
Fig. 3.4 Results of dense sand specimen configuration V-M-50-D and V-P-50-D.....	45
Fig. 3.5 Results of verification tests at vertical stresses of 50 kPa, 100 kPa and 150kPa.	46
Fig. 3.6 Comparison of peak shear stress at select normal stresses for specimens with metal grid plates and PBBJ boundaries.....	46
Fig. 3.7 Results of dense sand specimen configurations N, R, S, T and W, (a) stress-displacement response, and vertical displacements at (b) 50 kPa, (c) 100 kPa, and (d) 150 kPa. 50	
Fig. 3.8 Average peak angle of shearing resistance of dense sand specimens with different boundaries.	51
Fig. 3.9 Results of loose sand specimen configuration R, S, T and W, (a) stress-displacement response, and vertical displacements at (b) 50 kPa, (c) 100 kPa, and (d) 150 kPa.	53
Fig. 3.10 Average peak angle of shearing resistance of loose sand specimens with different boundaries.	54
Fig. 3.11 Results of dense ball bearing specimens, configurations N, R, S, T and F (a) stress-displacement response, and vertical displacements at (b) 50 kPa, (c) 100 kPa, (d) 150 kPa.	56
Fig. 3.12 Average peak angle of shearing resistance of dense ball bearing specimens with different boundaries	58
Fig. 3.13 Results of loose ball bearing specimen configuration R, S, T and F (a) stress-displacement response, and vertical displacements at (b) 50 kPa, (c) 100 kPa, and (d) 150 kPa. 61	
Fig. 3.14 Average peak angle of shearing resistance of loose ball bearing specimens with different boundaries.	62
Fig. 4.1(a) Cloud of non-contacting particles, and (b) particles settled into direct shear box in PFC 3D.....	67
Fig. 4.2 Specimen set up in LIGGGHTS before starting shearing	69

Fig. 4.3 (a) Shear stress - displacement and (b) vertical displacement of DEM Fric10.0 and DEM Fric0.0	72
Fig. 4.4 Locations of five measurement spheres.....	73
Fig. 4.5 Void ratio of DEM Fric10.0	75
Fig. 4.6 Void ratio of DEM Fric0.0	75
Fig. 4.7 Incremental displacements of particles in DEM Fric10.0	77
Fig. 4.8 Incremental displacement of particles in DEM Fric0.0.....	77
Fig. 4.9 Contact force network of dense DEM Fric10.0 at shearing displacement 0.0 and at shearing distance 6.0mm.....	79
Fig. 4.10 Contact force network of DEM Fric0.0 at shearing displacement 0.0 and at shearing distance 6.0mm	79
Fig. 5.1 (a) Surface of a steel ball bearing and (b) Surface of a gypsum sphere under scanning electron microscope (SEM) at same magnification power	82
Fig. 5.2 AM printed spheres of 4mm, 6mm and 10mm diameters (a) gypsum and (b) photopolymer	83
Fig. 5.3 Compression testing on a 10mm diameter cylinder: (a) gypsum (b) photopolymer	85
Fig. 5.4 Uniaxial compression testing machine	86
Fig. 5.5 Inter-particle friction testing on 4mm diameter photopolymer spheres	86
Fig. 5.6 Rockwell testing on: (a) gypsum cube; (b) gypsum sphere.....	87
Fig. 5.7 Inter-particle friction test of 4mm gypsum sphere	91
Fig. 5.8 Inter-particle friction test of 4 mm photopolymer sphere.....	92
Fig. 5.9 Interferometric view of 10 mm gypsum sphere (a) surface (b) profile before shearing .	92
Fig. 5.10 Interferometric view of 10 mm gypsum sphere (a) surface (arrow represents direction of shearing) (b) roughness profile after shearing.....	93
Fig. 5.11 Interferometric view of 10 mm photopolymer sphere (a) surface (b) roughness profile before shearing.....	93
Fig. 5.12 Interferometric view of 10 mm photopolymer sphere (a) surface (b) profile after shearing	94
Fig. 5.13 DIC calculated strain from 10 mm diameter gypsum cylinder in uniaxial compression	95
Fig. 5.14 DIC calculated strain from 10 mm diameter photopolymer cylinder in uniaxial compression	95

Fig. 5.15 (a)-(j) Uniaxial compression test on gypsum spheres	98
Fig. A.1 SEM image of 10 mm diameter gypsum sphere.....	115
Fig. A.2 SEM image of steel ball bearing.....	115
Fig. A.3 Aspect ratio and True sphericity variation of gypsum sphere.	116
Fig. A.4 Aspect ratio and True sphericity variation of photopolymer sphere.	116

LIST OF TABLES

Table 3.1 Properties of the precision steel ball bearings used in the direct shear experiments	39
Table 3.2 Minimum and maximum void ratio of the specimens tested.....	39
Table 3.3 Details of the verification experiments on sand specimens	44
Table 3.4 Details of the experiments on dense sand specimens	49
Table 3.5 Details of the experiments on loose sand specimens	52
Table 3.6 Details of the experiments on dense ball bearings.....	57
Table 3.7 Details of the experiments on loose ball bearing specimens	60
Table 4.1 Sample size and particle diameters for DEM Fric10.0 and DEM Fric0.0.....	67
Table 4.2 Material properties used in the DEM Simulation	69
Table 5.1 Shape parameters for AM spheres	88
Table 5.2 Inter-particle friction and surface roughness values of gypsum spheres.....	89
Table 5.3 Inter-particle friction and surface roughness values for photopolymer spheres before shearing.	90
Table 5.4 Parameters influencing the deformation and response of gypsum specimens.....	102
Table 5.5 Rockwell hardness values	102
Table A.1 Post shear surface roughness of gypsum and photopolymer material from confocal microscope for a scan area 50 μm x 50 μm	117
Table A.2 Post shear surface roughness of gypsum and photopolymer material from interferometer for a scan area 50 μm x 50 μm	117
Table A.3 Diameter and aspect ratios of gypsum spheres used in the hardness test	118
Table A.4 Crushing load details and hardness of gypsum spheres.....	119
Table A.5 Shape parameter calculation for 4 mm gypsum specimen.....	120
Table A.6 Shape parameter calculation for 6 mm gypsum specimen.....	121
Table A.7 Shape parameter calculation for 10 mm gypsum specimen.....	122
Table A.8 Shape parameter calculation for 12 mm gypsum specimen.....	123
Table A.9 Shape parameter calculation for 4 mm photopolymer specimen.....	124
Table A.10 Shape parameter calculation for 6 mm photopolymer specimen.....	125
Table A.11 Shape parameter calculation for 10 mm photopolymer specimen.....	126

CHAPTER 1: INTRODUCTION

1.1 Background and motivation for research

Granular soil response has been studied extensively over the past years. Most commonly, laboratory tests such as direct shear, direct simple shear, and triaxial shear are utilized for understanding the overall response of granular soils. This overall response is typically defined based on the shear stress response during shearing, as well as the volumetric response obtained from the tests. The behavior of granular soil depends on the applied stress, as well as different factors that control the interlocking and micromechanical rearrangements of the individual particles such as void ratio, particle characteristics (e.g., shape, surface friction, mineralogy), and fabric (i.e., particle arrangements and contact forces). Understanding granular behavior at the particle level is important since the design of structures is based on strength, as well as deformation characteristics of the soil.

Laboratory experiments, even with advanced instrumentation, do not provide detailed information on particle-scale granular behavior. Hence, various numerical models have been developed to understand the complex nature of granular materials. One such approach is continuum modeling, which uses constitutive laws for modeling soil response. While it gives valuable insight into material response overall, this method is not as effective when there is stress or strain localization, especially in granular soils (Coetzee and Els, 2009, Potyondy and Cundall, 2004). With the emergence of powerful computers, the discrete element method (DEM) modeling originally proposed by Cundall and Strack (1979) has gained popularity because of its ability to model individual soil particles and obtain information at the particle-scale.

The information from DEM simulations can be used to examine numerous features of soil behavior difficult to obtain in experimental testing (e.g., analyzing the soil fabric, determine and monitor the principal stresses and strains and the rotation of the principal axes during shearing. Some form of calibration or validation of DEM simulations with physical laboratory tests is important to provide confidence that the response from the DEM model matches the response of the same material under similar conditions in laboratory. As a calibration approach, micro-parameters such as stiffness, friction coefficients, damping coefficients, and in some cases bond strength are varied in the DEM simulations until the macro-scale response matches with the experimental response (Barla and Barla, 2005; Coetzee and Els, 2009; Potyondy and Cundall, 2004). Generally, for validation studies, the DEM simulations use idealized granular materials with simple geometry (e.g. disks or spheres) for computational efficiency. To validate these DEM simulations in the laboratory, spherical particles such as glass ballotini or metal ball bearings are typically used in the experiments (Bernhardt et al., 2016; Cui and O’Sullivan, 2006; O’Sullivan and Cui, 2009; Roubtsova et al., 2011).

Although it is more time intensive, DEM research has made a shift towards modeling more accurate particle shapes because of its large influence on granular response. Validation of these types of models, however, is very difficult. The particle shapes are typically simplified in the DEM models to reduce the computational demand (Fig. 1.1). Therefore, a comparison with laboratory results on the actual material is not a one-to-one comparison and ends up being more of a calibration than a validation. While manufactured glass ballotini and ball bearings are available, there is no similar consistent manufactured product with more complex shapes.

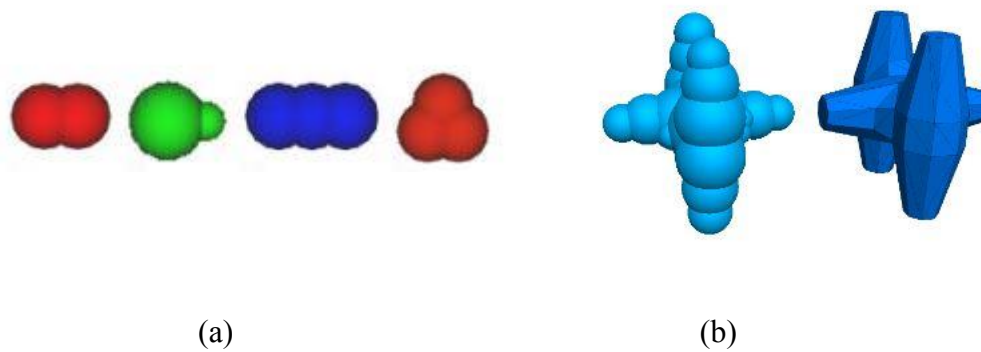


Fig. 1.1 Bonded spheres and rods (a) Yan and Ji, 2009, (b) Itasca, 2015

Recently, additive manufacturing (AM), often termed 3D printing, has gained popularity due to its ability to create 3D parts with a variety of complexity from 3D models. In order to use AM particles as analogue soil for validation studies, the characterization of the AM material is essential to ensure its suitability for laboratory testing.

The proposed research is focused on two main areas related to the validation of DEM models. First, boundary effects caused by the typical shear inserts used in direct shear tests are investigated using laboratory testing and validated DEM simulations. This serves as an example of the use of idealized granular material (i.e. metal spheres) in a laboratory study and DEM validation study. In the second portion of the research, the use of AM materials as an analogue soil for laboratory testing is investigated. As a first step in studying AM materials for their use in DEM validation studies, the material properties and surface characteristics of two different materials are evaluated. This characterization serves to examine the use of novel materials (i.e. AM particles) in future validation studies.

1.2 Research hypothesis and objectives

The main objective of this research was to test the hypothesis that *the use of suitable idealized granular material can lead to a better understanding of granular behavior in laboratory studies and in DEM validation studies*. As a first step, laboratory direct shear tests on Ottawa sand and commercially available precision steel ball bearings were used to analyze the effects of boundary shear inserts on the macro-scale response. Two simple DEM simulations comprised of spheres were also used to investigate the effects of boundary friction on the macro- and micro-scale response.

When non-spherical shapes of granular particles are used in DEM simulations, validation materials other than steel ball bearings or glass ballotini are needed. AM granular particles are an alternative way to reproduce the DEM samples in the laboratory, especially when different shapes of particles are to be recreated in large numbers. The mechanical properties of these AM particles need to be obtained in order to determine the suitability for laboratory tests. These properties are also needed as inputs in the DEM models. Secondly in this research, two AM technologies and corresponding materials were examined to determine their suitability for DEM validation studies. The parameters needed in future DEM simulations were also determined for these materials.

The objectives of this research were to:

- 1) Examine the influence of different shear boundaries in direct shear tests using laboratory results and validated DEM simulations
- 2) Characterize AM materials for use in future laboratory tests and DEM simulations

1.3 Dissertation overview

This dissertation is comprised of seven chapters. This chapter presents motivation and objectives of the research. Chapter 2 contains a summary of previous research that includes DEM modeling of direct shear tests, experimental testing of direct shear tests, as well as background on the properties of idealized granular materials suitable for experimental validation of DEM simulations. Chapter 3 encompasses the experimental direct shear testing results and discussion of specimens with sand and steel ball bearings with various shear boundaries to understand the effect of using different shear insert boundaries on the overall response of the specimens. Stress-strain responses, as well as the contractive and dilative behavior of the specimens are discussed. Chapter 4 compares DEM simulations of direct shear tests with two different boundary friction coefficients and the laboratory experiments on specimens without any projections on the boundary plates. Micro-scale analyses of the DEM simulations with the different boundaries are also discussed in Chapter 4. Chapter 5 describes the characterization study of AM spheres for their use in laboratory validation of DEM simulations and Chapter 6 summarizes the main findings of the research and provides recommendations based on the findings. The additional supporting data for the results discussed in Chapters 3, 4, 5, and 6 are provided in the Appendix.

CHAPTER 2: LITERATURE REVIEW

This research focuses on two main areas: laboratory testing and validated DEM modeling to analyze the response of granular material and boundary effects in a direct shear apparatus, and evaluation of the use of AM particles in experimental tests to validate DEM simulations. This literature review will provide a brief overview of earlier research related to granular material behavior, followed by a summary of the origin, progress, and recent research using DEM. Previous studies on direct shear testing, modifications, and limitations are also discussed. Finally, a brief discussion on AM technologies and general properties of granular material are presented.

2.1 Granular material behavior and discrete element method (DEM) modeling

Granular material behavior is important to researchers in a variety of disciplines such as civil engineering, geology, chemical engineering, physics, geophysics, and molecular dynamics. When a granular soil is subjected to shear stress, the resulting strength is directly tied to the volumetric response (i.e. dilation or contraction). Many experimental studies have examined this relationship (Taylor, 1948; Wroth, 1958; Bolton, 1986; Houlsby, 1991). In general, the volumetric response depends on particle morphology, the geometrical arrangement of the particles (i.e. fabric), contact bonds or force chains, external stresses, and specimen density. In other words, the macro-scale response is governed by the micro-scale or particle-level mechanics of the material. Nonlinearity, loading path dependency, stress dilatancy, anisotropy, non-coaxiality, failure and jamming transition are some of the complex responses that are exhibited by the granular material under confined or unconfined loading.

Translation and rotation of particles cause the deformation of the granular material, while the elastic deformation of individual particles has little influence in the overall deformation (O'Sullivan, 2002). Other factors influencing the overall granular response are crushing and breaking of the individual particles. Particle breakage has been a subject of study for several researchers (Hardin, 1985; McDowell et al., 1996; Coop et al., 2004). It is noted here that particle crushing will not be examined as a part of this dissertation work. The models will consider only elastic behavior of the particles, which further signifies the need to ensure a similar behavior is mimicked in the laboratory testing.

For several years, geotechnical engineers have been using a Mohr coulomb failure criterion, which is justified in majority of cases and is extensively applied in the macroscopic response of granular soils. Developments in numerical methods such as Finite element method, Granular element method, Distinct element method or Discrete element method, etc. have also provided insights into granular behavior. Soil has been treated as a continuum in many earlier studies and finite element analyses have been used to study aspects of granular material such as shear banding, dilatancy, anisotropy and strain localization. Shear banding is the localized zone of deformations (Fig. 2.1), which are experimentally studied by plane strain loading conditions. Particle morphology, applied stresses, boundary conditions and soil stresses play an important role in the failure state of soils. Initial studies investigated shear bands to determine the inclination of the band as well as the comparison to Mohr coulomb solutions (Mandl et al., 1977; Vardoulakis 1980; Bardet & Proubet, 1991). Other studies considered the internal structure of shear bands and the dimensions of the shear band by making use of various imaging techniques such as optical microscopy, radiography and X-ray computed tomography (CT) (Alshibli & Hasan, 2008; Halls et al., 2010). Although many experimental and finite element method (FEM)

studies of granular materials have been conducted, many of the particle-scale observations have been derived through DEM studies.

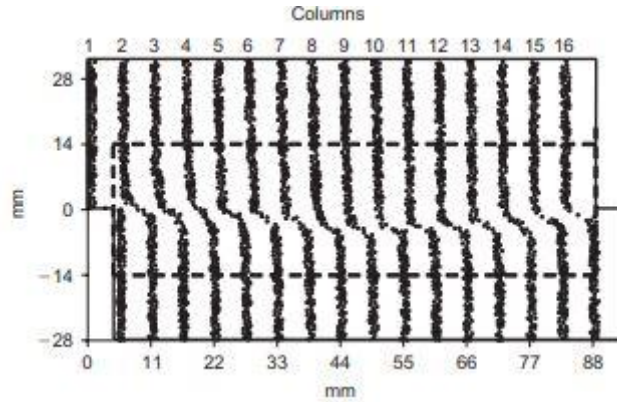


Fig. 2.1 Shear banding (Wang, et al., 2007)

2.2 Overview of DEM modeling

DEM simulations have been used in geotechnical engineering, chemical engineering, the mining industry, and powder technology industries to study the behavior of particulate materials. DEM is defined as a simulation method that models the displacements and interactions of individual particles. Simple numerical contact models are used to govern individual particle contacts and capture the granular behavior. The advantage of DEM over continuum methods is that individual or discrete particles can be modeled and are allowed to make or break contacts. DEM generally uses simplified particle geometries, such as spheres or clumps of spheres for computational efficiency.

Geotechnical researchers became more interested in DEM simulations after the DEM study published by Cundall and Strack (1979) comparing DEM results with laboratory results using photo elastic disks. DEM allows the application of forces and deformations to virtual particles, and the overall behavior of the material can be explored. Unlike physical testing, the

evolution of contact forces, particle rotations and contacts of the particles can be effectively monitored in DEM simulations. The method is based on an explicit time stepping algorithm where equations of motion are solved for a finite time interval to determine the incremental displacements and rotations (O’Sullivan, 2011). To calculate inter-particle forces, a force displacement law is used, and the results are fed back into equations of motion until equilibrium is reached (Itasca, 2014). There are numerous computational platforms available for DEM simulations. This research uses commercially available PFC3D 5.0 developed by Itasca Consulting Group, Inc and LIGGGHTS for the simulation of direct shear tests. Fig. 2.2 shows the calculation sequence in a DEM system.

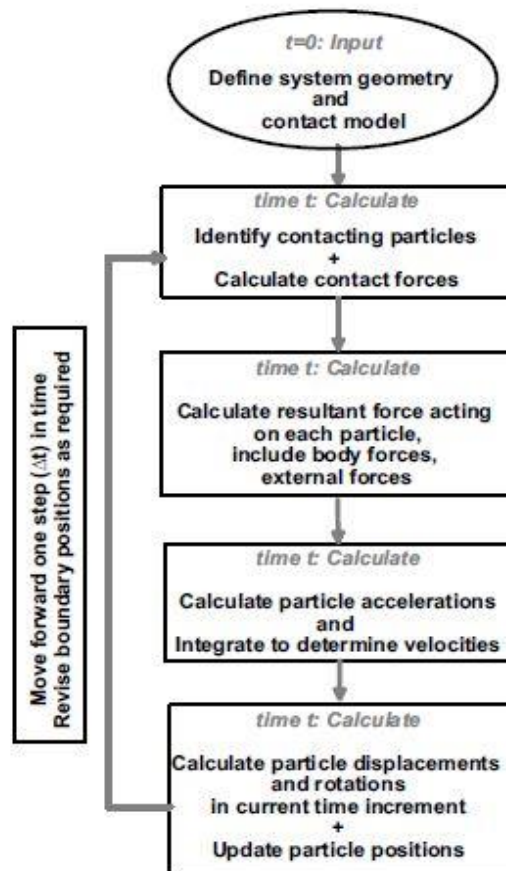


Fig. 2.2 Steps in the calculation phase of DEM simulations

In DEM, contact detection and contact resolution are the two stages that analyzes the determined contact forces or inter-particle reactions by identifying the contacting particles. Contact forces are calculated using a contact constitutive model from relatively simple contact geometry. One of the most computationally demanding calculations is the calculation of contact forces in a DEM simulation (O' Sullivan, 2011). Soft-particle and hard-particle approaches are the two most common approaches in DEM (Fig. 2.3). For the soft-particle approach, the rigid particles are allowed to overlap one another over a small area to simulate the plastic deformation that would occur at the physical contact. The hard-particle approach does not allow this overlap. In the soft-particle approach, multiple particle contacts are handled simultaneously, whereas in the hard-particle simulations only one instantaneous collision is modeled at a time (Zhu et. al, 2007). The soft-particle approach is the most common approach used for capturing the particle interaction and therefore it is the focus of this dissertation.

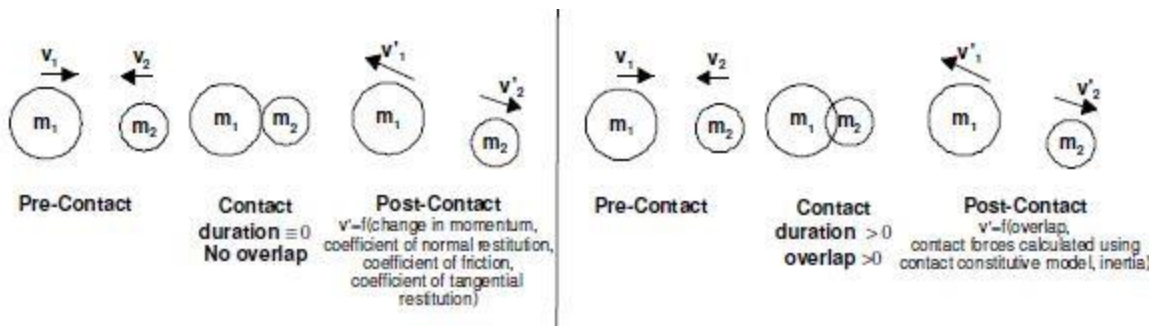


Fig. 2.3 Hard particle and soft particle approach in DEM

In the soft-particle approach, several contact model options have been implemented through the years. Cundall and Strack (1979) proposed a combined linear-spring viscous dashpot model whereas Di Renzo and Di Maio (2004) proposed linear spring model without a viscous dashpot. Elastic contact between two spheres has also been described by Hertz using a nonlinear relationship by considering the normal force and normal displacement (O'Sullivan,

2011). Further developments of this original model known as the Hertz-Mindlin and the Deresiewicz models have been considered to be more theoretically sound. These more complex models are slightly more time consuming for simulations. As such, they are not as popular as the linear models; however, they have been shown to well represent the contacts between two spheres (Cavarretta et al., 2012). Even more complex models have been developed which consist of a semi-latched spring displacement model proposed by Walton and Braun and a model of tangential force by Thornton and Yin (1991). Because of the fact that it is still rather simple and that it captures the complexities of particle contacts well, the Hertz-Mindlin contact model was used in this study and will be discussed in further detail in the following section.

2.2.1 Hertz Mindlin contact model

The Hertz-Mindlin contact model is used for successfully for capturing granular material behavior in the particle level by several researchers (Bernhardt et al., 2016; Cui & O'Sullivan, 2006). In Hertz-Mindlin model, the relationship between contact forces and relative displacements are non-linear elastic. This consists of normal and tangential components based on deformation of smooth spheres under frictionless contact. Contact force is resolved into a Hertzian and a damping or viscous component (Fig 2.4). Material properties such as shear modulus, Poisson's ratio, and inter-particle friction are used to determine the stiffness values for the Hertz-Mindlin contact model. The DEM simulations are performed using PFC 3D from Itasca. In PFC, the secant normal contact stiffness is given by

$$K_n = \left(\frac{2G\sqrt{2r}}{3(1-\nu)} \right) \sqrt{\delta_n} \quad (2.1)$$

Where G is the shear modulus of particles, δ_n is the normal contact displacement, ν is the Poisson's ratio of the particles, and r is the average radius. Tangential contact stiffness is given by

$$K_s = \left(\frac{2(3G^2(1-\nu)^{\frac{1}{3}})}{2-\nu} \right) f_n^{\frac{1}{3}} \quad (2.2)$$

For two particles in contact, denoted by A and B, the average values used in Equations 2.1 and 2.2 are defined as

$$r = \frac{2r^A r^B}{r^A + r^B} \quad (2.3)$$

$$G = \frac{1}{2}(G_A + G_B) \quad (2.4)$$

$$\nu = \frac{1}{2}(\nu_A + \nu_B) \quad (2.5)$$

where r is the average radius, G is the average shear modulus, and ν is the average Poisson's ratio for the two spheres in contact.

The normal contact force is then calculated as

$$F_n = K_n \delta_n \quad (2.6)$$

When the tangential contact force reaches its maximum allowable value, which is taken to be the coefficient of inter-particle friction angle multiplied by the contact normal force, particle sliding occurs. It is noted that the Hertzian contact model assumes the surface of contacting spheres to be perfectly smooth and frictionless. The contact area of the two particles in contact was also assumed to be small compared to the dimensions of the contacting particles. Therefore, the

overlaps are often limited to 0.1-0.5% of the radius of the spheres in contact to ensure the small contact area.

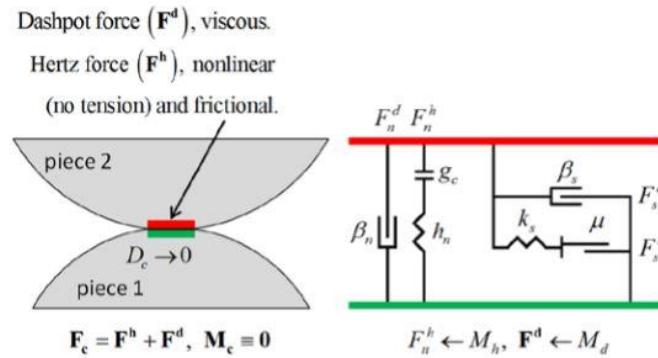


Fig. 2.4 Components of Hertz contact model (Itasca consulting Group, 2014)

2.2.2 Methods for specimen preparation in DEM

DEM simulations start with the generation of particles to assemble the specimen or the geometry of the system under consideration for analysis. In the laboratory, loose specimens for dry granular material are typically made by air pluviation. For dense specimens, tamping the material layer-by-layer is typically used to achieve a lower void ratio. Feng et al. (2003) and O'Sullivan (2002) discussed the need to develop specimen generation algorithms for specimen preparation which are capable of achieving realistic packings with the least amount of computational effort. The arrangement of particles, or the fabric influences the overall behavior of the specimen. Cui (2006) summarized the available approaches to generate and densify the specimens as constructive approaches and dynamic approaches. A constructive approach implies that the generation and densification of the specimen is by implementing geometrical calculations where particles are placed systematically without simulating the dynamic particle motions. Jodrey and Tory (1979; 1985), introduced sedimentation techniques which can produce

dense specimens relatively quickly. In this method, an initial group of particles is produced as a layer and further additions are made one-by-one by means of modifying the coordinates of the center of the particles added into the system (Fig 2.5). If there are overlaps between the spheres, they are eliminated by changing the coordinates of the particle centroids and this process is repeated for all the remaining particles until the required number of particles are assembled.

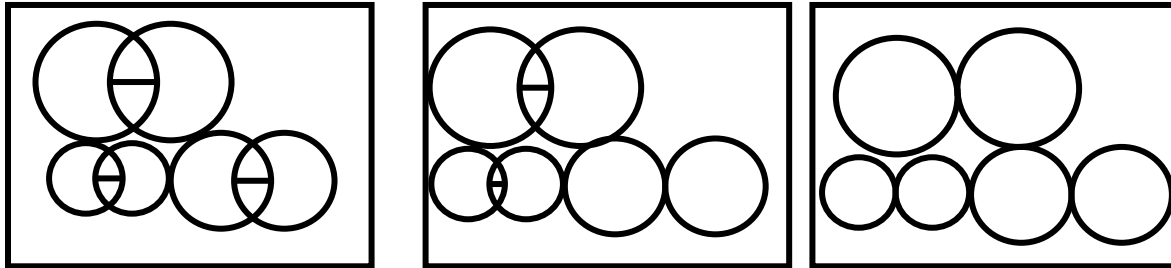


Fig. 2.5 Steps in the elimination of overlaps in the specimen preparation (Jodrey and Tory (1979; 1985)

Bagi (2005) and Feng et al. (2003) also proposed similar methods which are called the “dropping method” and the “open front technique and closed front technique”, respectively. The dropping method (Fig. 2.6) suggested by Bagi (1993) can be considered as a two-dimensional version of the sedimentation technique.

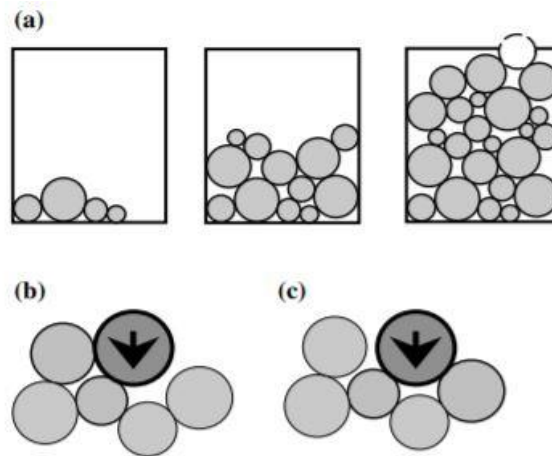


Fig. 2.6 (a) The general progression of the algorithm; (b) unstable and (c) stable position of a new particle (Bagi, 1993)

The advancing front approach by Feng et al. (2003) begins with a small assembly of discs. In the closed form algorithm, the size of the assembly grows as more discs are added into the system to touch the existing particles. One disadvantage is that this method creates large gaps around the assembly near the boundaries. On the other hand in the open form algorithm, the assembly is created layer by layer (Fig 2.7). Bagi (2005) noted that anisotropy is introduced in specimens created using the open front algorithms. The inward packing method, also introduced by Bagi (2005), produces stress free assemblies of grains touching each other without any overlaps (Fig. 2.9). This method is faster than the dynamic methods and Bagi stated that this method produced an isotropic assembly when compared to sedimentation techniques. This method also produced a specimen packed in the domain, without large gaps along the boundary. While generation of an isotropic packing might be important for some studies, soils are typically deposited and consolidated under K0 conditions in which vertical strains are allowed during compression, but no lateral strains are allowed. Therefore, some of the dynamic sedimentation techniques may be more appropriate for these systems.

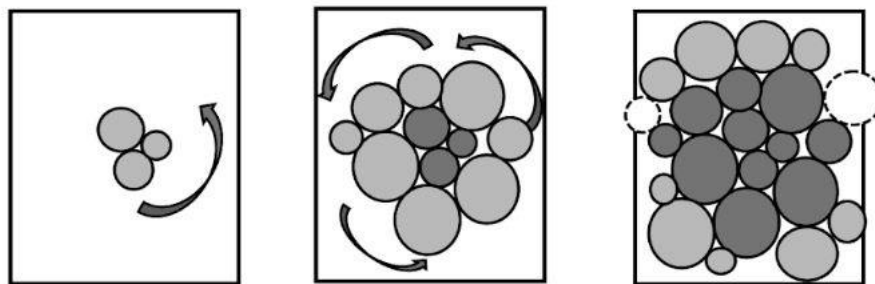


Fig. 2.7 Schematic of the closed form algorithm (Feng et al., 2003)

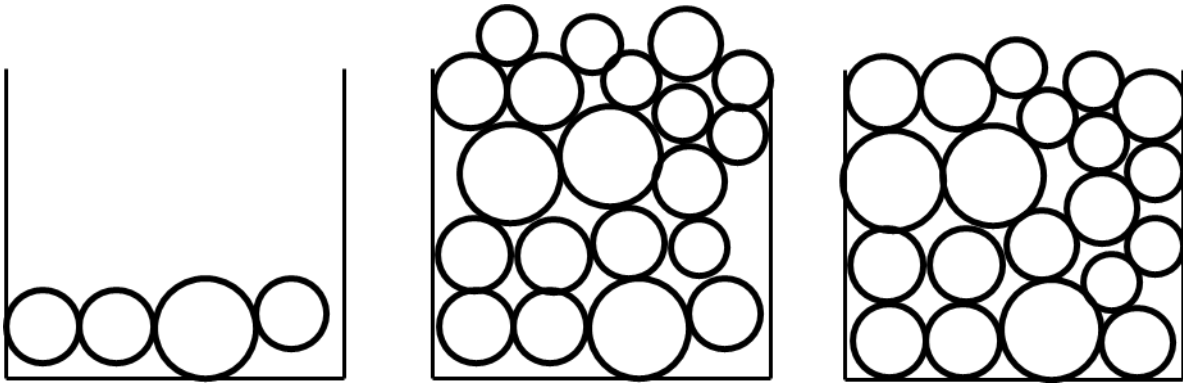
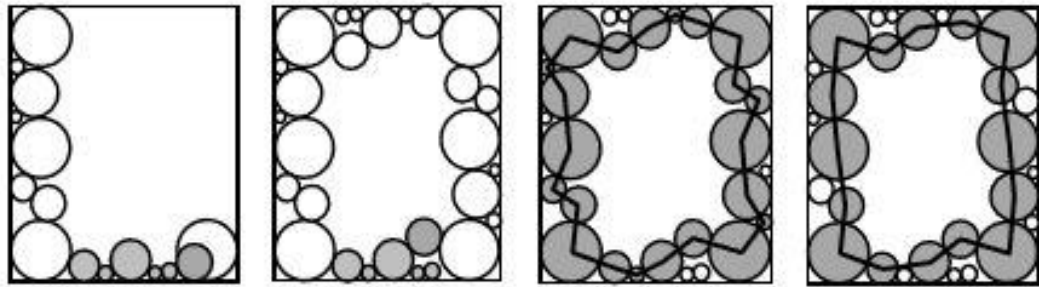
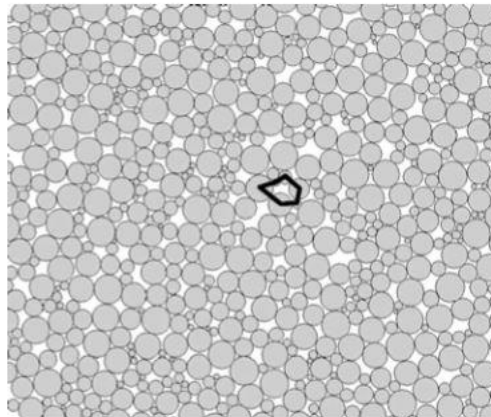


Fig. 2.8 Schematic of open form algorithm



(a)



(b)

Fig. 2.9 (a) Preparation of initial front for the inward packing method in a 3D assembly by placing the particles along the outer boundaries and (b) final front, (Bagi, 2005)

Itasca (2002) introduced a random generation approach, to define the random size and location of particles so that they are essentially a non-contacting cloud of particles within the

system domain. In order to fit the required number of particles in the chosen system, PFC tries different locations if the first selected location has an overlap with neighboring particles. Air pluviation can be simulated in DEM by creating a non-contacting cloud of the desired diameter particles and then allowing them to settle when gravity is activated. This method is very similar to the pluviation specimen preparation methods used in the laboratory for dry granular specimens, although slight variations are used to create looser or denser specimens. Fig. 2.10 shows the pluviation of a non-contacting cloud of particles into direct shear cylindrical boundaries. While these methods replicate the laboratory procedures well, dynamic methods require large calculation sequences and they are computationally expensive and time consuming.

Several other dynamic approaches can be used to generate specimens at a target porosity and stress condition. One such example is radius expansion where a required number of particles at reduced sizes are placed in the system domain. The particle diameters are then gradually increased so that they expand into each other until desired porosity or stress state is achieved. It is difficult to control both the size and numbers of the particles in this particular method and still achieve the target porosity and stress state. Another method commonly used is compaction using rigid boundaries because it is faster than pluviation and the number of particles and diameters can be controlled while still being able to achieve a target stress state or porosity. This method consists of placing the particles at their actual size in the system and then the boundary walls are slowly moved inwards to achieve a target porosity or stress state. Figures (2.11 and 2.12) show the dynamic methods of specimen preparation.

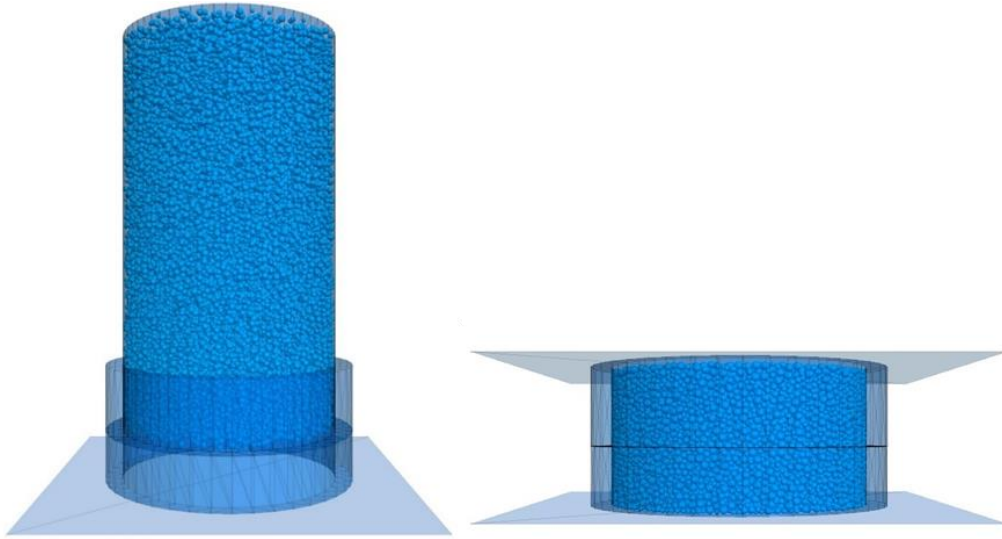


Fig. 2.10 (a) Pluviation of spheres to create a granular assembly for direct shear test.

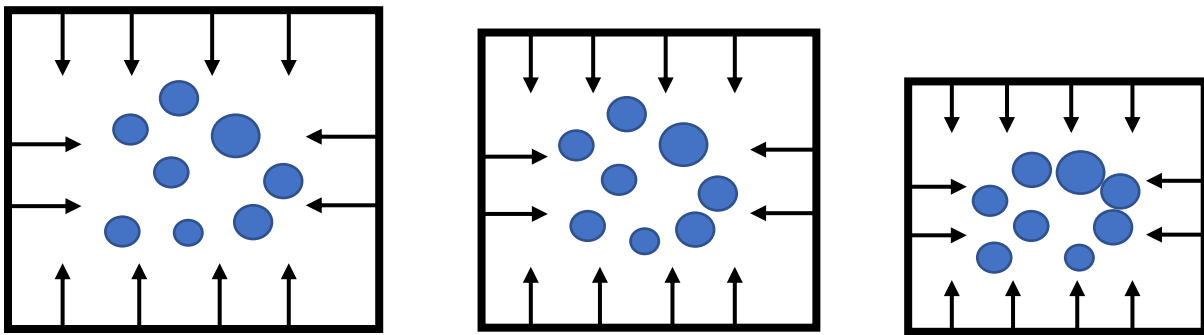


Fig. 2. 11 Dense specimen preparation by moving the walls inwards

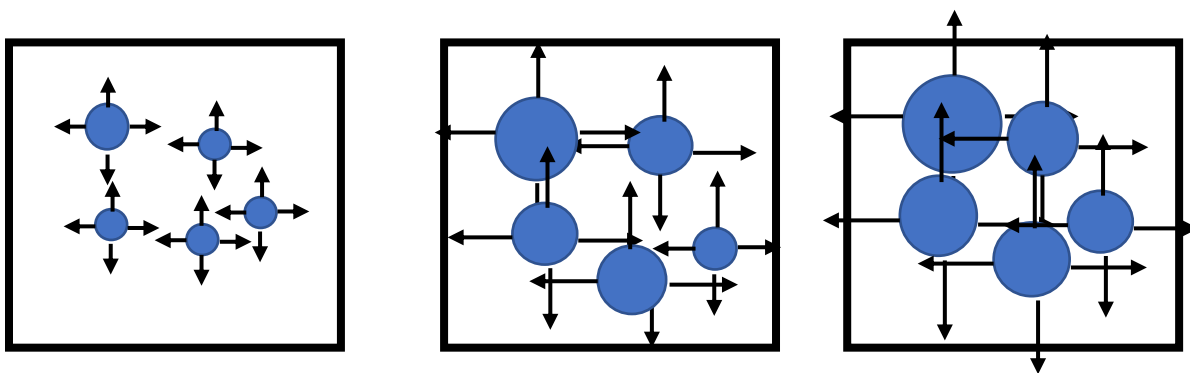


Fig. 2.12 Dense specimen preparation by radius expansion of particles

While there are many DEM studies, only a few validation studies have directly compared the physical laboratory data and DEM simulation data. A few researchers have conducted such experimental validation studies using precision steel ball bearings as a simple granular material

(Bernhardt et al. 2016; Cui and O’Sullivan, 2006) and have obtained good agreement between the laboratory and DEM responses. Bernhardt et al. (2016) demonstrated the importance of DEM specimen preparation in validation studies to ensure similar stiffnesses at low strains. In addition, Bernhardt et al. (2014) also presented a comparison of the initial state of the specimens created using several of the methods discussed above. They showed that pluviation (i.e., gravity settling) created a cross-anisotropic specimen which is similar to what is observed in laboratory prepared specimens. Therefore, a similar pluviation simulation technique was used in this study.

2.3 Direct shear

2.3.1 Previous experimental direct shear studies

The direct shear test is one of the simplest and oldest tests used to determine the shear strength properties for geotechnical design and analysis. It is an inexpensive and quick test to determine the drained shear strength of soil and has been used extensively to analyze granular soils. The direct shear apparatus consists of a two-part box separated at mid-height into equal halves, which enclose a circular specimen (Fig. 2.13). The top half of the box is held stationary while the bottom half moves horizontally at a constant rate. A vertical force is applied to the specimen and shear force is exerted on the horizontal plane. Standard test procedures and specimen requirements are documented in ASTM D3080.

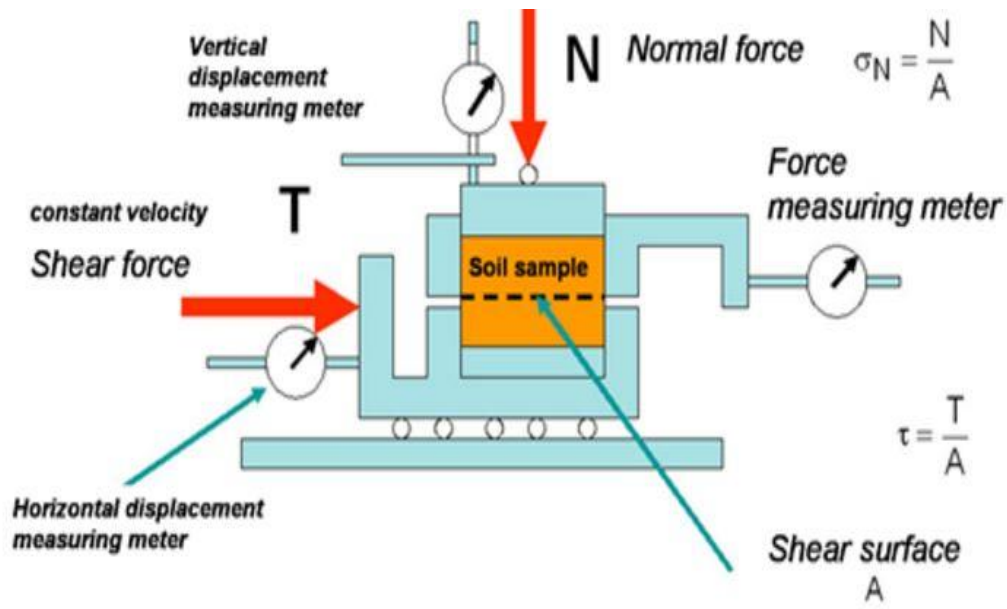


Fig. 2.13 Direct shear device (www.tankonyvtar.hu)

Some of the limitations associated with the direct shear apparatus include: non-uniformities of the stresses and strains within the specimen, and difficulty in defining the failure criterion (Potts, et al, (1987)). Numerical and experimental studies of direct shear tests were conducted by researchers to examine the non-uniformities inside the specimens, as well as the specimen size effects on the overall behavior. Potts et al. (1987) conducted finite element method (FEM) modeling of direct shear tests and found that strains within the final failure zone were uniform in spite of the non-uniform stresses and strains before the peak. Dounias and Potts (1993) observed the stress-strain non-uniformities in the direct shear specimen before reaching peak strength.

Despite several shortcomings, direct shear tests are still used extensively by researchers and practicing engineers for routine strength testing due to its simplicity and low cost. Researchers examined how the design of the apparatus influences the response (Jewell, 1989, Lingz and Dietz, 2004). An improved version of the direct shear box was suggested by Jewell

(1989), by fixing the top cap to the upper half of the shear box when vertical load is applied. This prevented the rotation of the top cap and increased the chance of uniform stresses inside the specimen. Shibuya et al. (1997) performed direct shear tests on different sands and analyzed the influence of wall friction and boundary properties. They found that wall friction, and rotation of the top cap results in lower peak and residual strengths. They discovered that due to the effects of wall friction, the vertical stresses acting on shear plane were considerably lower than the vertical stress measured from the specimen and the value of peak friction angle was over estimated with the stress calculated from the applied normal force. Lings and Dietz (2004) modified the conventional direct shear apparatus by the addition of ‘attached wings’ on the sides of the shear box to investigate the effects of gap size on specimens with Leighton buzzard sand. The results indicated that the new apparatus produced high quality data for angles of shearing resistance and dilation. The tests used a flat boundary at the bottom and a flexible flat boundary at the top to avoid developing non-uniform stress conditions at the top of the specimen. The rotation of the top frame of the shear box was not eliminated by the new design despite these arrangements.

The specimen size effects of direct shear tests were also studied to understand its effects on the peak angle of shearing resistance (Parsons, 1936; Palmeira and Milligan 1989). Cerato and Lutenecker (2006) evaluated three different sizes of direct shear boxes as well as five different sand specimens and reported that the friction angle could depend on sand type, specimen size, and relative density (Fig. 2.14).

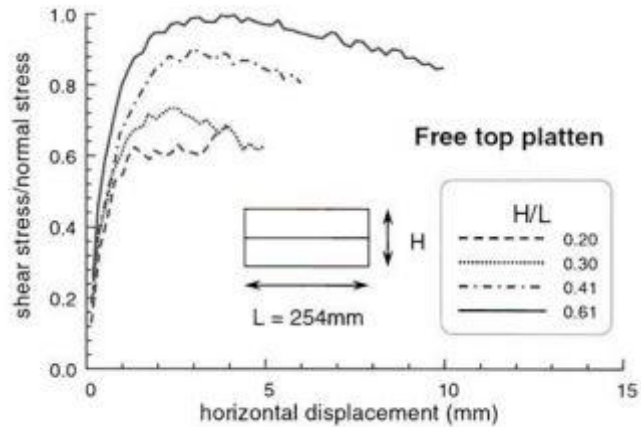


Fig. 2.14 Influence of aspect ratio on determination of friction angle (Cerato and Lutenegeger (2006))

Even though there have been several experimental and numerical studies conducted on granular material in the direct shear device, as noted in ASTM D3080, there is still limited information available regarding the effects of the boundary types on the observed response. The common boundary plate inserts used in the physical tests are either porous stones or grid plates, which ensure drainage, as well as the transmission of shear stress across the soil specimen. The roughness of the metal boundary was found to have significant influence on the coefficient of friction of sand specimens (Uesugi and Kishida (1986); Uesugi et al. (1988)). Regardless of these findings, exact criteria for the texture of the inserts have not been established in ASTM D3080.

Hryciw and Irsyam (1993) made visual observations of soil-boundary interactions in laboratory direct shear experiments with ribbed (i.e. grid) boundaries of different spacing and geometries (Fig 2.15). Tests conducted on Ottawa 20-30 sand and Glazier Way 20-30 sand established that there was a difference in the development of the shear zone depending on the type of boundary used.

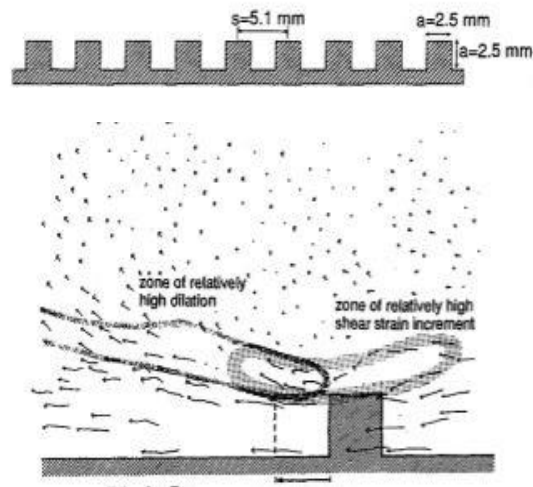


Fig. 2.15 Hryciw and Irsyam (1993)

While these tests gave valuable insight into the influence of the boundary type on the shear response, there are several other boundary types commonly used in laboratory and numerical modeling that were not considered, such as sawtooth, waffle stone and fixed-particle boundaries. DEM simulations often use a fixed-particle boundary, high roughness boundary or a sawtooth boundary to simplify the model and reduce computational cost; however, few documented studies have considered the influence these boundary types may have on the resulting response.

2.3.2 Previous direct shear DEM studies

In the 1990s and early 2000s, several studies of DEM simulations with granular materials were published. Because the proposed research focuses on the direct shear apparatus, only studies relevant to this device are presented here. Thornton and Zhang (2003) and Zhang and Thornton (2007) evaluated two-dimensional (2D) simulations of the direct shear test using DEM and found that there were variations in dilation in the shear zone when compared to the dilation

measured from the boundary. Cui and O'Sullivan (2006) analyzed the micro-scale parameters obtained from laboratory validated 3D DEM simulations of direct shear tests on precision ball bearing specimens. The results showed that significant stress and strain non-uniformities occur within the specimens, which concurred with the findings of previous continuum and 2D DEM analyses (Potts et al., 1987; Masson & Martinez, 2001; Zhang & Thornton, 2002).

The arrangement of particles, particle groups and pore spaces in the soil, termed soil fabric, has also been the focus of DEM direct shear studies. Soil strength and stiffnesses are anisotropic, i.e they vary depending on the direction in which the soil is deformed. Direct shear tests of coarse grained specimens with different gradation are tested experimentally and with DEM models to understand the influence of particle size by (Bagherzadeh-Khalkhali et al., 2009). Contact anisotropy information and shear behavior are evaluated from DEM simulations whereas influence of particle size in shear behavior was observed in both experimental testing and simulations. The authors found that friction angle and dilation of the specimen increases when larger particles are used. The anisotropy of soil specimen can be quantified by considering the orientation of the contact normal which can be directly calculated in the DEM simulations. A fabric tensor is used as an index to describe the packing structure of particles. In a two-dimensional DEM simulations study, Mahmood and Iwashita (2010) considered the sensitivity of the overall response and the evolution of the internal material fabric to the initial particle orientations with elliptical particles. They found that using elliptical particles the particle rotations and void ratio in the shear band are in better consensus with the particle rotations and void ratio in the shear band of natural granular soils.

Several 2D and 3D DEM studies also incorporated different shapes of granular materials. Typically, clumps formed by bonding several spheres are used as non-spherical particle

simulations. Ni et al. (2000) modeled direct shear tests on specimens with two bonded spheres in 3D DEM simulations to understand the effect of particle shape and inter-particle friction on granular response (Fig . 2.16). The simulation results were compared with direct shear tests conducted on Leighton buzzard sand specimens, and they found that the particle size relative to the direct shear box influences the overall strength, but the effect decreases when the number of particles are thirty thousand.

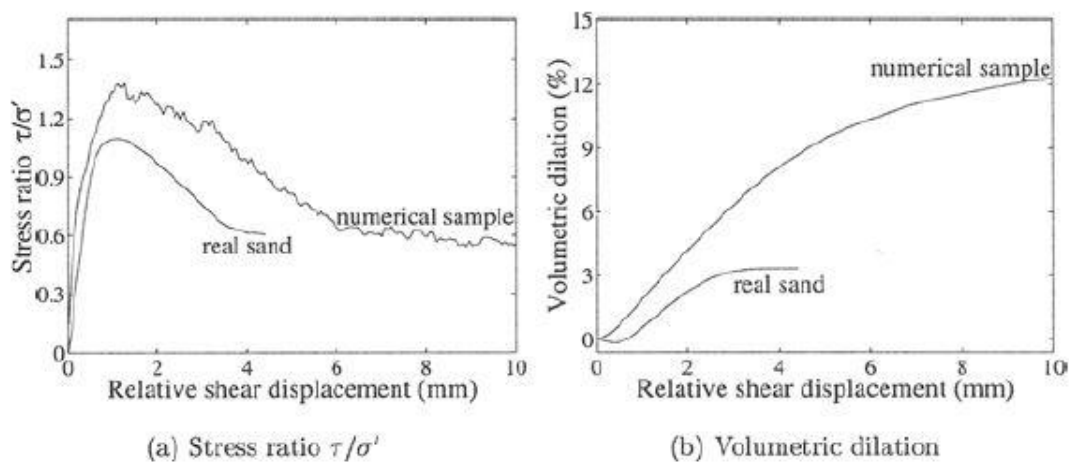
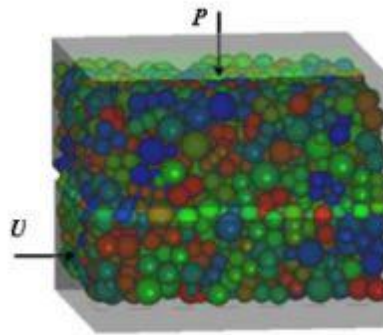
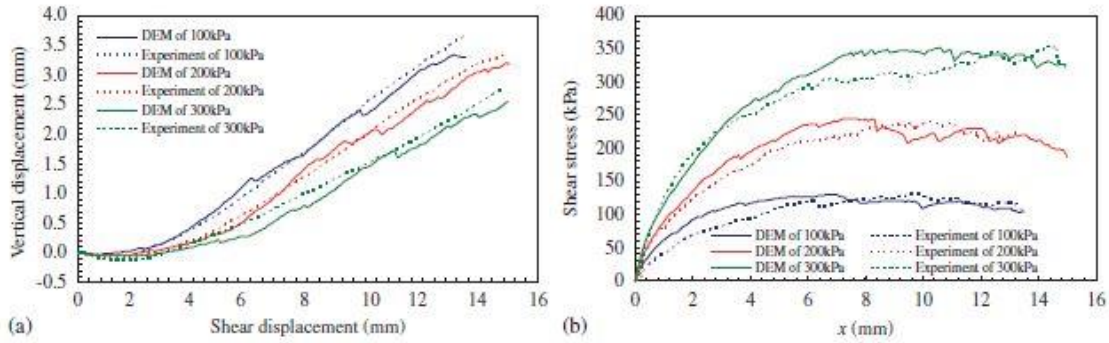


Fig. 2.16 DEM and experimental data compared by Ni et al. (2000)

Yan and Ji (2009) conducted 3D DEM simulations of direct shear tests of irregular limestone rubbles by making use of clumps. These simulations were directly compared with laboratory shear testing of limestone rubbles and the authors found that vertical displacements and shear stresses compared well with laboratory tests (Fig. 2.17).



(c)

Fig. 2.17 Direct shear test by Yan and Ji (2009)

Wang and Gutierrez (2010) conducted 2D DEM direct shear experiments on glass ballotini with saw tooth boundaries and high-friction boundaries to investigate the effect of the boundary in granular material behavior for specimens with different aspect ratios. They established that with large aspect ratios (i.e. large length to height ratio), the specimens had progressive failure due to boundary induced strain localization, whereas in small aspect ratio specimens, the bulk behavior was controlled by the global failure. Further, Wang and Jiang (2011) performed 2D DEM experiments for unifying interface shear tests (IST) and direct shear tests to study boundary induced soil behavior. The ISTs considered sawtooth boundaries and irregular asperity surfaces, and the direct shear tests considered high friction surfaces. The authors found that the stress ratios obtained from the IST using the sawtooth boundary were

closest to those obtained from direct shear tests with high rough surface boundaries, concluding that mobilized shear strength depends on the degree and extent of strain localization and shear banding in the specimen.

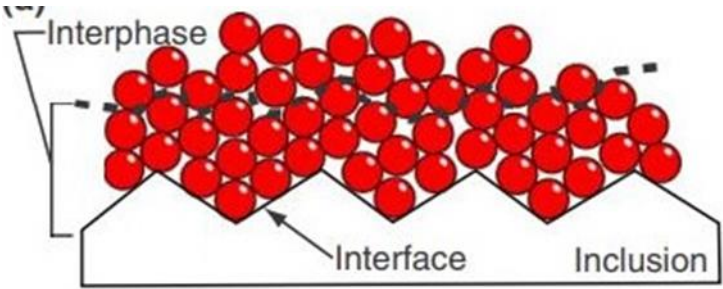


Fig. 2.18 2D simulation of sawtooth boundary with glass ballotini for direct shear testing (Wang, Dove, & Gutierrez, 2007)

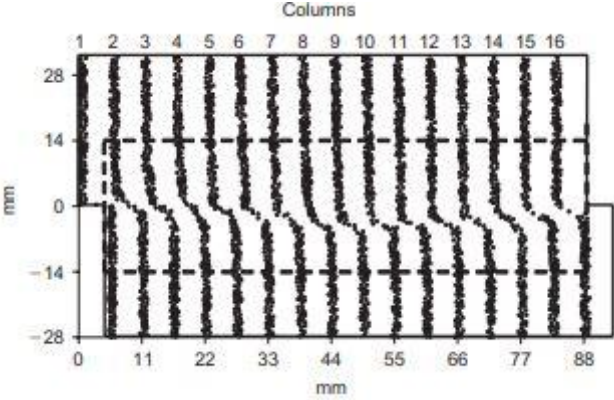


Fig. 2.19 Shear banding (Wang, Dove, & Gutierrez, 2007)

While these 2D DEM simulations were validated against results available in the literature, there is currently insufficient information available regarding how these types of boundaries would perform in laboratory experiments. Furthermore, until recently, it was difficult to recreate the 3D specimen boundaries with different geometries such as grid inserts or sawtooth projections in DEM simulations. Similar to the study by Wang, Dove, & Gutierrez (2007), recently, Jing et al. (2016) studied the shear banding in direct shear specimens in 3D DEM

simulations with varying surface roughness at the boundaries and found that as the roughness varies, the thickness of shear band varies with the roughness factor. Shear banding mechanism was investigated and changes in granular media are explained by Iwashita and Oda (2000). They pointed out the changes in void ratio affect dilatancy at shear bands.

2.4 Additive manufacturing of granular material

To understand granular material behavior, it is crucial to establish the relationship between the particle morphology and the bulk response. Naturally occurring granular soils differ in the mineral composition, as well as in the shape and surface characteristics of the particles. The soil behavior itself is complex and the different mineralogical compositions and surface characteristics makes it very difficult to accurately understand the distinctive effect of particle shape on granular response.

Additive manufacturing (AM), however, provides a means to create particles of varying shape while maintaining the surface and material properties, making it possible to single out shape for the first time. AM, often termed PBJ, is a collection of technologies that use a computer model to create a 3D product (Sachs et al., 1993; Gibson et al., 2015). AM has been used in a wide variety of fields (e.g., automotive and aerospace industries for printing prototypes of machine parts, bone tissue engineering for synthetic bone replacement materials, dental implants, and prosthetics). Generally, AM is comprised of two steps: modeling the construction and printing the model. The object is built layer-by-layer as defined by a 3D CAD model (Bredt et al., 1999). Depending on the quality of the surface finish, as well as the chemical and mechanical properties necessary to satisfy the requirement, post processing of the parts may also be necessary.

There are five major types of AM technologies, stereolithography (SLA), fused deposition modeling (FDM), laminated object modeling (LOM), and powder bed binder jetting (PBBJ). This research focuses only on two types: SLA and PBBJ printing. SLA uses a liquid plastic or a photopolymer resin. The resin is converted into a solid object by creation of successive, adjacent, cross-sectional layers, which are then cured using ultraviolet radiation (Hull, 1984).

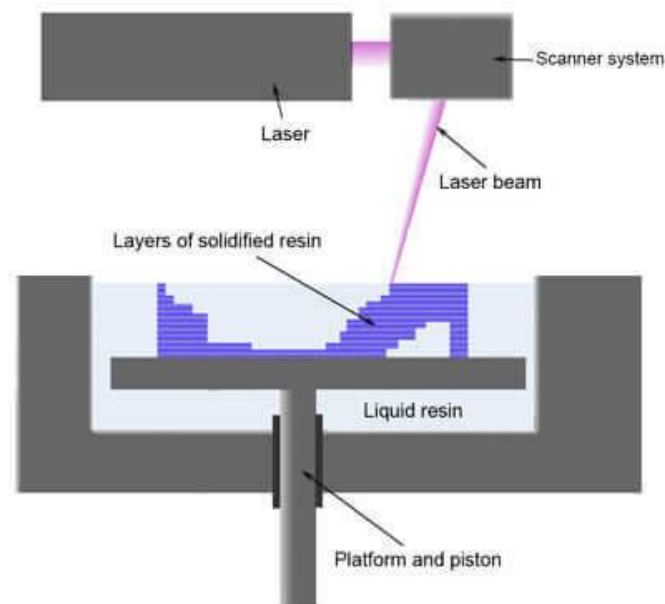
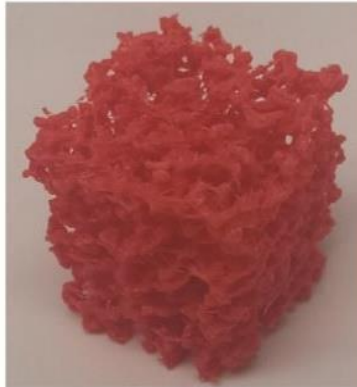


Fig. 2.20 Side view of PBBJ printing process (<https://all3dp.com/>)

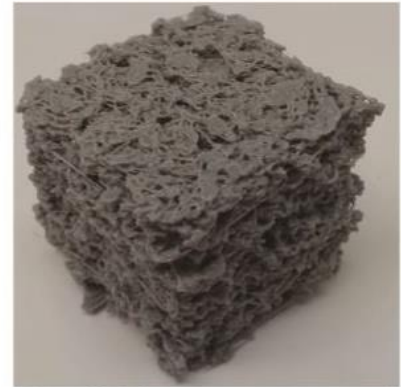
PBBJ is a powder-based method, where a layer of powder is spread on a build platform and a liquid binder is sprayed through an inkjet printer nozzle to bond the powder. The build platform lowers, another layer of powder is deposited and spread, and the process continues until the part is finished and the surrounding loose powder is removed to reveal the printed object.



Rock core, Osinga et al.
(2015)



T2 = -20 (micropores+macropores)
Dimensions: 28x28x28 mm
Magnification: 20x
3D Printer: Makerbot 2X
Material: ABS



T2 = -20 (micropores+macropores)
Dimensions: 30x30x30 mm
Magnification: 5x
3D Printer: Makerbot Mini
Material: PLA

Fig. 2.21 Examples of applications of AM in geotechnical engineering

Cost-effective SLA and PBJ technologies can be used for producing large quantities of desired particle shapes that are representative of real grains to run full-scale laboratory experiments. Recently AM has been introduced in geotechnical engineering studies such as slope models for seismic studies (Liang and Knapett, 2017). Rock modeling and testing using AM was employed by several researchers to assist in the deformation and failure analysis of rock-type materials, as well as in the simulation of similar material modeling experiments (Jiang, et al., 2016 ; Ju et al. 2014) as shown in Fig 2.21. Miskin and Jaeger (2013) illustrated the advantage of additive manufacturing (AM), or PBJ, techniques for the analysis of granular morphology. They conducted 3D DEM simulations and laboratory triaxial compression testing on AM granular particles of bonded spheres to experimentally investigate the effect of particle shape on the mechanical response. Significance of the AM granular materials for compression tests in the laboratory was demonstrated by Jaeger (2014). In this study, one to four spherical units were joined to produce AM grains. By using AM particles, the morphology can be separated from the material properties for examining the effect of these factors individually on the overall material

response. Hanaor et al. (2016)] used Fourier descriptors generated from 2D grain contours to model the complex morphology of granular materials. Particles were fabricated using AM featuring a layer-by-layer photo-polymerization (Fig. 2.22). While the AM particles represented the shape characteristics well, the triaxial tests were only conducted at a low confining stress of 20 kPa and the authors noted that there was a time-dependent compressibility of the soft photopolymer material. While both of these studies showed successful use of the material, very little information was given regarding the material properties and surface characteristics that would be needed in a DEM simulation. It is also unclear whether these materials would be suitable for DEM studies in which a nearly rigid particle behavior is preferred.

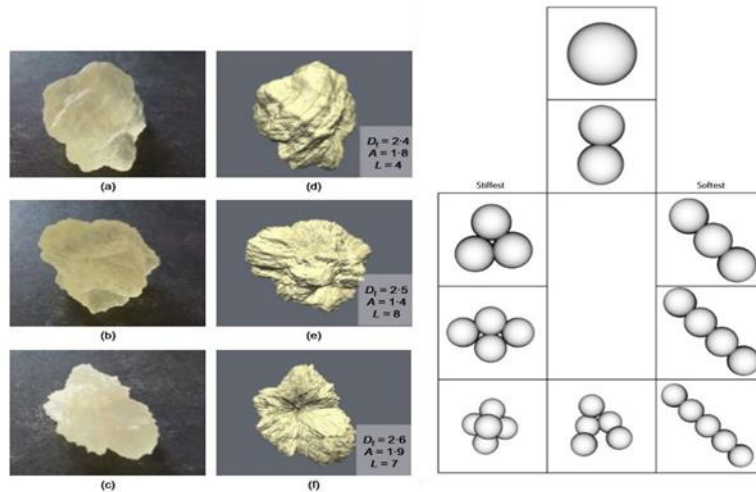


Fig. 2.22 (a) Comparison of printed and simulated grains (Hanaor et. al, (2016)) (b) Models of Bonded spheres, (Miskin and Jaeger (2013))

Watters et al. (2017) presented a review of the AM technologies available, which would likely be suitable for laboratory testing applications in terms of equipment and material costs, and material properties. Out of the many AM processes and materials examined, two in particular were determined to be the most appropriate: a gypsum powder composite produced in a PBBJ device and a photopolymer resin produced in a SLA device. These materials are

considered in the work presented herein and more discussion of the materials and the AM devices are given within the methodology.

2.5 Characterizing idealized granular material

Use of idealized granular materials such as steel ball bearings or glass beads in DEM validation studies have been illustrated by several researchers (Cui and O’Sullivan, 2006; Hartl and Ooi, 2006; Roubtsova et al., 2011; Bernhardt et al., 2016). Cui and O’Sullivan, (2006), O’Sullivan and Cui (2009), and Bernhardt et al. (2016) showed that the overall response (i.e. stress-strain or stress-displacement macro response) of granular assemblies involving steel ball bearings compared well with their DEM simulations. Barreto (2009), however, did not have good agreement between his laboratory tests with soda-lime spheres and the corresponding DEM simulations. This was most likely due to the small variations in the geometry of the soda-lime particles used in the experimental testing compared to the perfectly spherical particles used in the DEM simulations. Therefore, selection and characterization of optimal particle type and properties are important to ensure good agreement between DEM simulations and the corresponding experimental tests. Cavarretta et al. (2012) recommended that more robust characterization could aid in selecting an analogue material which has similar properties to natural sand grains. As a means to provide this more robust characterization, Cavarretta (2009) and Cavarretta et al. (2012) tested borosilicate glass beads using new technologies, and custom built apparatuses to quantify shape and roughness, particle contact stiffness and inter-particle friction of the glass beads.

Size, form, sphericity, roundness and roughness are the factors that describe the shape of the particle. Form is the property that represents the geometrical proportions of the particle. This can also be represented in terms of sphericity, or the shape of the particle in comparison with a

sphere. A brief discussion of selected shape descriptors for a particle is given below. More details on shape description parameters and correlations of circularity and regularity can be found in Cavaratta (2009).

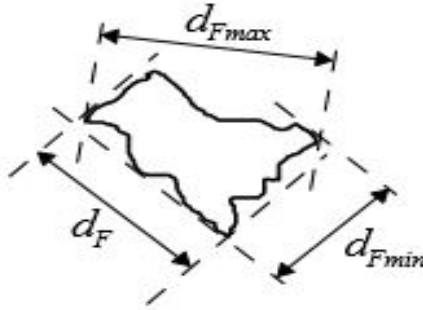


Fig. 2.23 Definition of Feret diameters (Cavarretta, 2009)

- Feret diameters: The distance between two parallel tangents on the particle. Maximum Feret diameters and minimum Feret diameters are presented in Fig. 2.23.
- Aspect ratio: The ratio of Feret minimum length to Feret maximum length.

$$\text{Aspect ratio, } AR = \frac{d_{Fmin}}{d_{Fmax}} \quad (\text{Cavarretta, 2009}) \quad (2.7)$$

- True sphericity: Wadell (1932) described sphericity as a three-dimensional property where circularity is a two-dimensional property. Sphericity is defined as the ratio of surface area of a sphere with the same volume as a particle to its actual surface area and calculated with Eq. (2.8).

$$\text{Sphericity, } \Psi = (d_1 d_2 d_3)^{\frac{2}{3}} \left[\frac{(d_1 d_2)^{1.6} + (d_1 d_3)^{1.6} + (d_2 d_3)^{1.6}}{3} \right]^{-\frac{1}{1.6}} (\text{Cavarretta, 2009}) \quad (2.8)$$

- **Circularity:** A measure of smoothness and roughness (Olson, 2011). The circularity is defined as the degree to which the projected section of area A and perimeter P is similar to a circle.

$$\text{Circularity, } C = \frac{4\pi A}{P} \quad (2.9)$$

During physical particle interactions, surface damage and plastic yielding occur at the contacts (Cavarretta, 2009); therefore, stress and deformation at the contact largely depend on the surface properties of the particle. Surface roughness can be quantified using a number of parameters, generally classified as extreme value parameters and average parameters. Extreme value parameters are based on the maximum or minimum values of the 2D surface profile and do not necessarily give an accurate estimation of overall topography. On the other hand, average parameters estimate the topography statistically such as the center line average (S_a or R_a) or the root mean square deviation (S_q or RMS) about the mean height of the surface profile. RMS is defined as the deviation of the surface from its average height. S_a/S_q can be used to ensure the topographical similarity of two surfaces. These roughness parameters are further explained in (Thomas, 1999).

Stress and deformations at the contact of a particle largely depends on the geometry and surface properties of the particle. Contacts between particles are divided into conforming and non-conforming contacts. Under a normal load, N , the mechanical response of the material traditionally follows a contact law such as the Hertz-Mindlin law which presumes a perfectly smooth sphere in contact within the elastic regime. Within the elastic loading regime, the Hertzian theory is represented as

$$N = \frac{4}{3} R^{0.5} E^* \delta^{\frac{3}{2}} \quad (2.10)$$

where R is the relative radius, E^* is the equivalent Young's modulus and δ is the particle deformation. $R = d/2$ for the spheres and E^* is

$$\frac{1}{E^*} = \frac{1-\nu_p}{E_p} + \frac{1-\nu}{E} \quad (2.11)$$

The compressive load at which the Hertzian behavior occurs depends on size, roundness and roughness, and elastic bulk properties. Furthermore, the Greenwood Tripp model (GT model) showed that, for a rough non-conforming contact, a threshold force noted as N_{GT} exists where the contact starts complying with Hertzian law (i.e. at $N = N_{GT}$). During the loading of a rough conforming contact, N_{GT} depends on an equivalent Young's modulus, E^*

$$N_{GT} \cong 100 RMS_f E^* (2R \cdot RMS_f)^{\frac{1}{2}} \quad (2.12)$$

where R is the relative radius and RMS_f is the flattened roughness which accounts for the natural curvature of the surface out of the roughness calculation. Cavarretta, et al. (2012) estimated the Hertzian behavior of borosilicate spheres by computing N/N_{GT} against the ratio of single contact strain δ and R , δ/R using uniaxial compression tests of single spheres. The plots obtained showed that for rough surfaces, the response conforms with the GT model, whereas the model is less accurate for smooth surfaces.

Another important particle characteristic is the inter-particle friction angle or coefficient. This property along with surface characteristics, fabric, and loading conditions influence the mechanical response of granular materials. Cavarretta, et al. examined steel ball bearings, glass ballotini and natural sand particles to determine inter-particle friction using a custom-built apparatus. These tests revealed that humidity significantly affected the inter-particle friction angle obtained for the glass ballotini, which was not observed in the steel ball bearings. Inter-

particle friction is a necessary input in DEM models. Thornton (2000), found that the macro-scale responses of spheres in a periodic cell are sensitive to inter-particle friction values for friction coefficients less than 0.35. Therefore, determination of inter-particle friction values for the materials used in DEM models are important to effectively capture the response of the macro-scale behavior of the specimens.

The ease at which a material deforms on its surface is often measured in terms of hardness. Measurement of material hardness was introduced in the early 20th century (Brinell, 1901) and led to common techniques such as Vickers (Fig 2.24), Berkovich, Knoop and Rockwell tests (Zhang, et al., 2011). Tabor (1970) summarized the hardness testing methods and indicated that the indentation hardness or yield pressure, p , of metal is a measure of its plastic properties which in turn can be related to the surface and bulk properties of the material. Hardness tests involve an indentation on the surface of a material which can be directly related to material strength. Cahoon, et al. (1971) showed that the yield strength of a material can be correlated to its hardness measurement. Furthermore, Pavlina, et al. (2008) highlighted the relationship of both the yield strength and the tensile strength of steel to its surface hardness. Rockwell hardness tests have been used to characterize the hardness of composite metals to correlate strength to hardness.

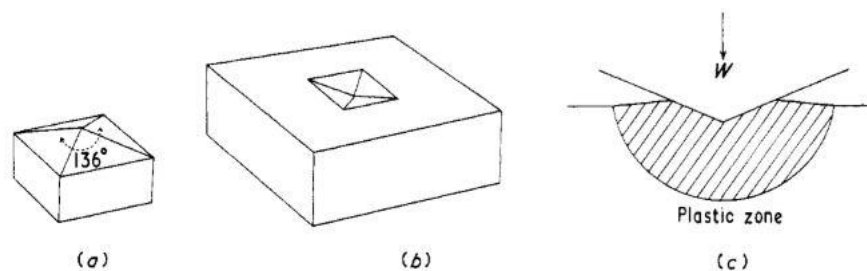


Fig. 2.24 (a) Viker's indenter (b) Indentation made on a specimen (c) Plastic zone

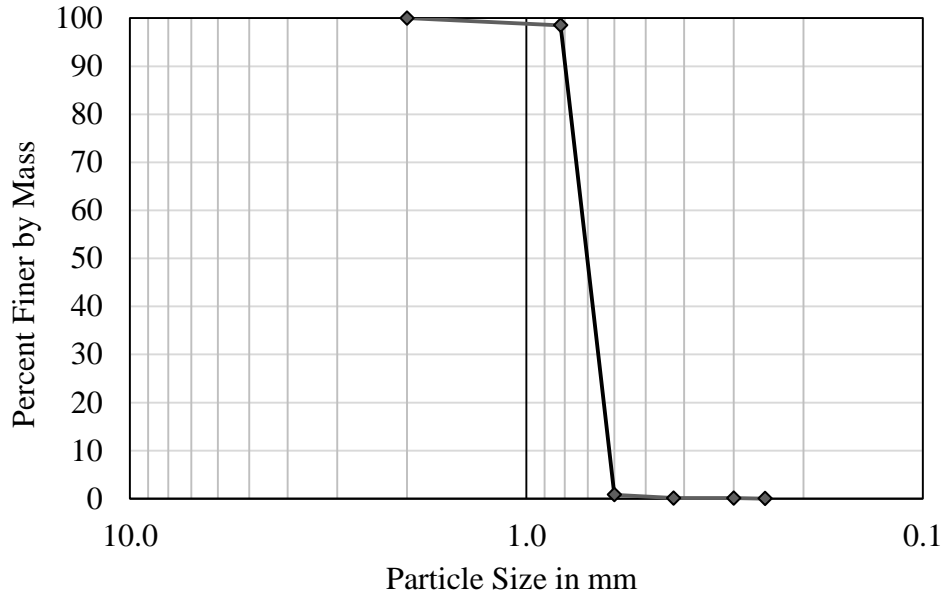
CHAPTER 3: EXPERIMENTAL EVALUATION OF THE INFLUENCE OF DIRECT SHEAR BOUNDARY TYPES ON GRANULAR MATERIAL RESPONSE

3.1 Introduction

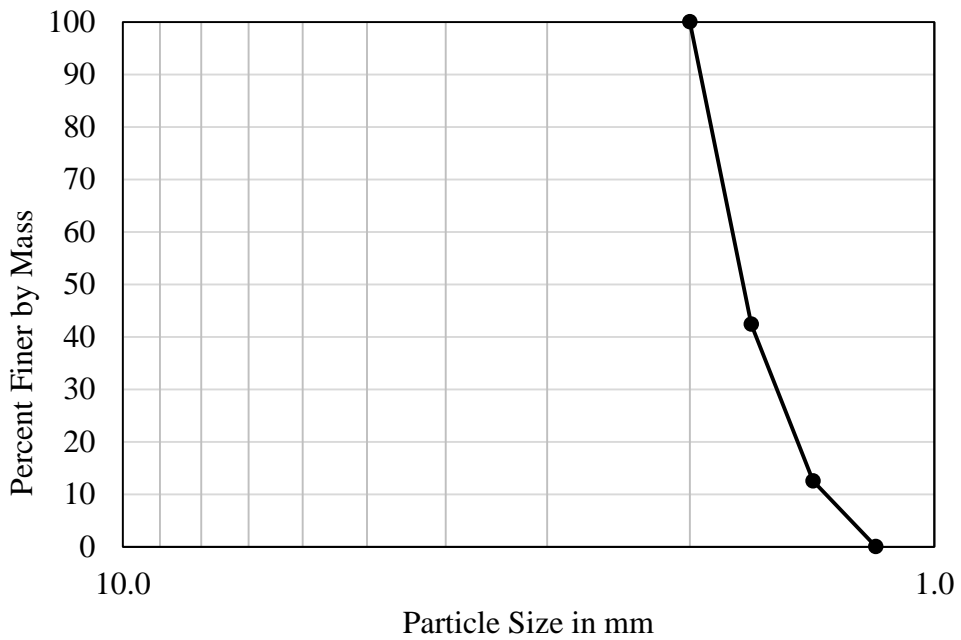
Direct shear tests were performed on dense and loose specimens of ball bearings and sand. To create different types of boundary plates, AM was used. Seven boundary plates were selected for these tests and they were paired with the loose and dense specimens of the two materials. A set of verification tests were performed on the metal grid plates typically used for direct shear tests and the AM versions. This chapter presents the specimen preparation and materials used for the tests. Further, the results from the verification tests are also presented and discussed.

The direct shear apparatus used in the current study consisted of the typical two-part box which encased a cylindrical specimen. The specimens tested were an average diameter of 63.5 mm, and an average height of 31.8 mm calculated from the bottom of the specimen to the top of the specimen excluding the box parts. The bottom half of the shear box was moved at a constant rate of 0.508 mm/min in accordance with ASTM D3080, while the top half was held stationary in the horizontal direction. Experiments were performed on dense and loose specimens of Ottawa 20-30 sand, as well as an idealized granular material. This study used American Iron and Steel Institute (AISI) 52100 Grade 25 precision chrome steel spheres manufactured by Thompson Precision Ball as the idealized granular material. Due to the tendency of uniform sized spheres to crystallize (i.e., form regular packing), three different diameters of spheres were used (Table 3.1). The specimens were comprised of approximately 8,862 spheres of each of the three sizes, totaling approximately 26,586 particles. Particle size distributions of Ottawa sand and ball bearings are illustrated in Fig. 3.1. The e_{\max} and e_{\min} of the specimens tested are summarized in

Table 3.2. Considering the fact that only a small range of void ratios were possible for the ball bearing specimens, only dense and loose specimens were tested.



(a)



(b)

Fig. 3.1 Particle size distribution of (a) Ottawa 20-30 sand, and (b) steel ball bearings

Table 3.1 Properties of the precision steel ball bearings used in the direct shear experiments

Property	Value
Nominal diameters (mm)	1.98
	1.59
	1.19
Density (kg/m ³)	7800
Shear modulus (GPa)	80

Table 3.2 Minimum and maximum void ratio of the specimens tested

Specimen	Void ratio
Ottawa sand	$e_{\max} = 0.83$
	$e_{\min} = 0.45$
Ball Bearings	$e_{\max} = 0.72$
	$e_{\min} = 0.52$

The geometry, dimensions and spacing of the six different types of boundaries are presented in Fig. 3.2. Not shown in the figure is the waffle stone which was used instead of the fixed-particle plate for the experiments involving specimens of dense and loose sand. In addition to the specimens paired with these boundaries, dense specimens of sand and ball bearings were tested with flat plates without any projections. With the exception of the waffle stone, all the boundary plates were printed using the gypsum-based PBBJ device described previously. This allowed for rapid generation of different geometries without the need for machining the boundary plates. The ratio (R) of the spacing of the projections on the grid insert to the

maximum diameter of the ball bearings were 1.5 and 4.8. Two different grid boundaries with R of 1.5 and 4.8, as well as two taller grid boundaries with R of 1.5 and 4.8 were used in this study as illustrated in Fig. 3.2(a), Fig. 3.2(b), Fig. 3.2(c) and Fig. 3.2(d). The spacing and height of these grid inserts were selected following the parameters used in a study by Wang, et al., (2007). The sawtooth boundary (Fig. 3.2(e)) was modeled such that the base of one triangular tooth was 3 mm and the height to the vertex was 1.5 mm. For the fixed particle boundary (Fig. 3.2(f)), precision ball bearings were glued using a high-strength epoxy to a flat AM plate. This type of boundary has been used previously in similar simple shear experimental tests (Bernhardt et al., 2016). Photographs of these plates are shown in Fig. 3.2.

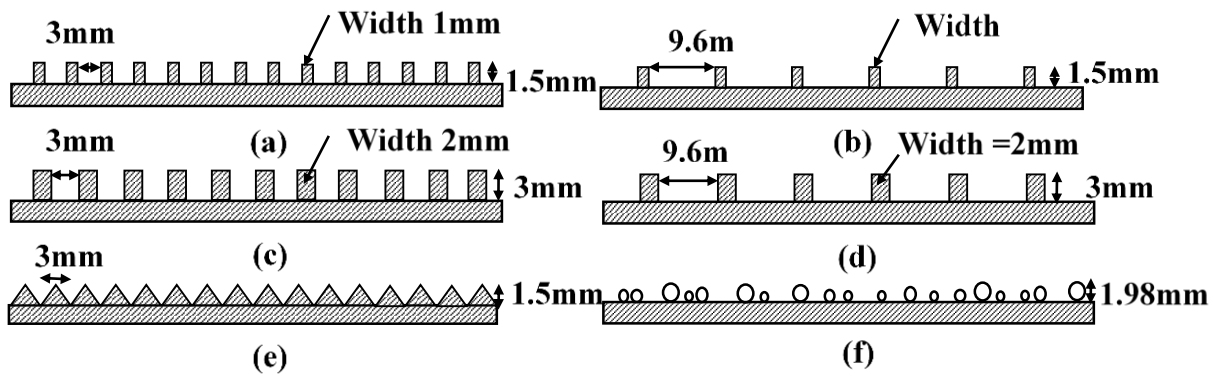


Fig. 3.2 Schematics of the AM boundaries (a) grid plate (R1.5) (b) wide spaced grid (R4.8) (c) grid plate with taller projections (T1.5) (d) wide spaced grid plate with taller projections (T4.8) (e) sawtooth (S) (f) fixed particles (F)

Prior to performing tests on the AM printed boundary inserts, ‘verification tests’ were conducted on dense Ottawa sand specimens using typical metal grid inserts and AM inserts with the same geometry (Fig. 3.2(a)). The material stiffness and surface properties of the AM plates differed from the typical metal plates used in the device and it was important to ensure that these differences did not affect the response. The verification tests compared the response of dense sand specimens under three initial vertical stresses of 50 kPa, 100 kPa, and 150 kPa with void

ratios varying from 0.45 to 0.53. Three tests were conducted at each vertical stress and the results were averaged to improve the clarity of the stress-displacement response and vertical displacement response. Mohr-Coulomb failure criterion was considered for computing the peak angle of shearing resistance. The tests were categorized according to the test type, boundary material, initial normal stress, and specimen density. The designations used include: ‘V’ for verification, ‘M’ for metal or ‘P’ for AM printed boundaries, the value of the initial vertical stress, and ‘D’ for dense. The comparison of the metal and the AM grid inserts under each initial stress is discussed in the corresponding results section.

Following the verification tests, dense and loose sand and ball bearing specimens were tested using the different boundary geometries. Dense sand specimens were prepared by alternating air pluviation and vibration in three equal layers. Loose sand specimens were prepared using a funnel to place the sand in the mold as loosely as possible (ASTM-D4253, 2014). Similar to the dense sand specimens, the dense ball bearing specimens were prepared by alternating pluviation and vibration in three equal layers; however, the loose ball bearing specimens were prepared by placing the ball bearings in a hollow cylindrical tube and quickly raising the tube to fill the mold (ASTM-D4253, 2014). Identical to verification tests, the specimens with AM boundaries were also tested under initial vertical stresses of 50 kPa, 100 kPa, and 150 kPa. The tests were designated by their respective boundary types (F–fixed, R1.5, R4.8, S, T1.5, T4.8, W-waffle stone and N – no projections), initial vertical stress, and specimen density (L-loose and D-Dense).

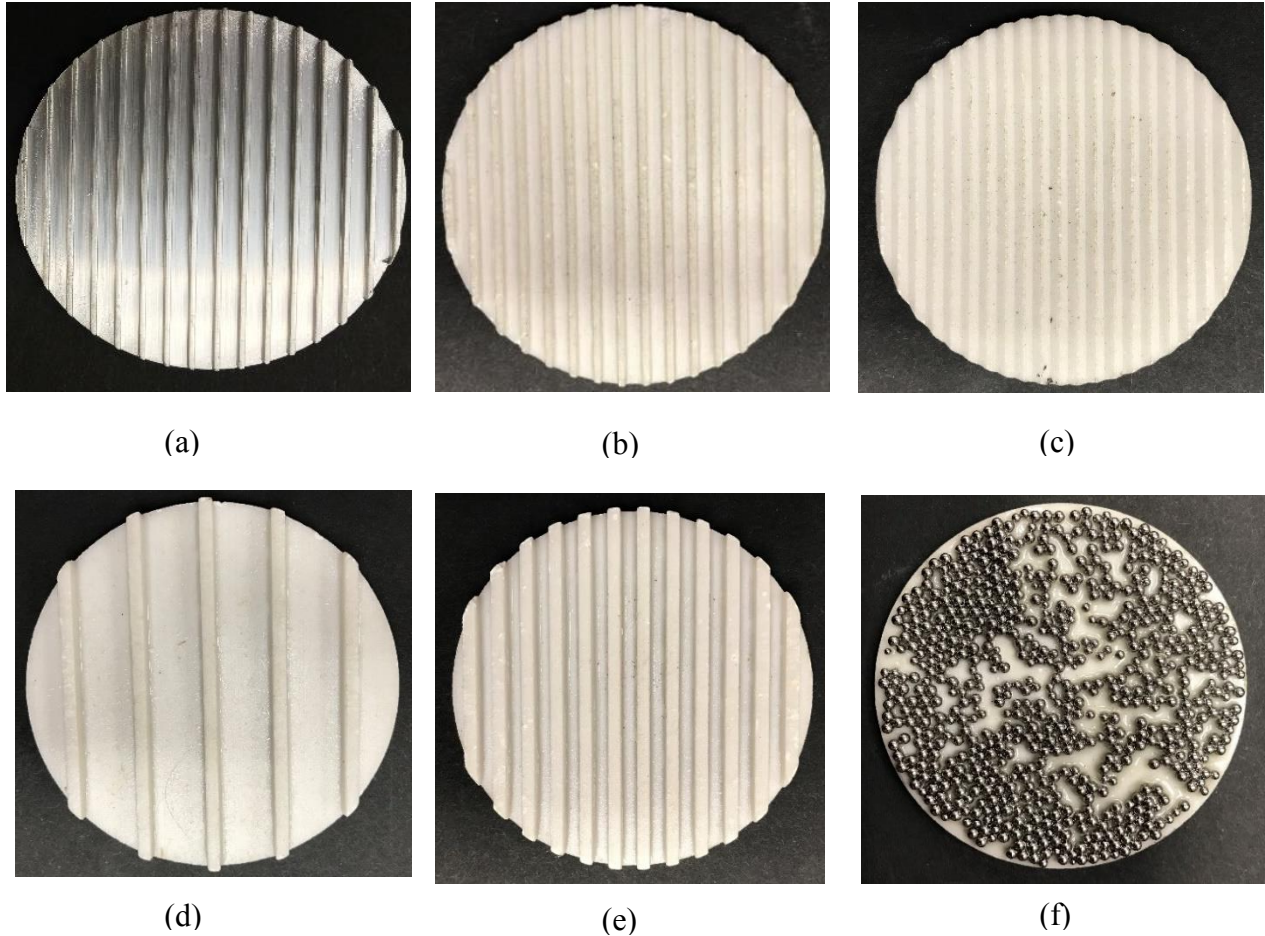


Fig. 3.3 Photographs of printed boundaries (a) regular grid plate (R1.5) (b) AM grid plate (c) sawtooth (d) wide grid plate with taller projections (T4.8) (e) grid plate with taller projections (T1.5) (f) fixed particles (F)

3.2 Verification tests on sand specimens with metal and AM grid inserts

The results of the experimental tests conducted on dense Ottawa sand with the metal grid inserts and similar AM grid inserts (R1.5), under three initial vertical stresses are illustrated in Figs 3.4 – 3.6 This particular boundary was chosen because it is the most common insert used. The range of void ratios and peak shear stresses for each set of tests are given in Table 3.3. The stress-displacement response, as well as the vertical displacements of three experiments conducted at 50 kPa initial vertical stress with the metal grid inserts and similar AM grid inserts are shown in Fig. 3.2. These tests are shown to demonstrate the experimental scatter observed

and justify the need for averaging the values for clarity in the comparisons. Considering the fact that the cross-sectional area on which both normal and shear load acts, is usually expressed in terms of the original area, using correction factors (ASTM D3080). It was determined that the area correction did not change the peak angle of shearing resistance; therefore, no area correction was applied in the following results. Fig. 3.5 shows the shear stress variation with respect to the horizontal displacement measured.

The peak shear stresses observed in the stress-displacement response indicate no particular trend between the metal and the PBBJ plates. Similarly, with the vertical displacements, there is no specific pattern in the results obtained for both types of grid plates. While more variability is seen in the vertical displacements, there is no consistency between grid types or void ratios that would indicate a difference in the response due to the boundary material. Hence, it is concluded that the variability of the results in Fig. 3.4 are due to slight experimental scatter. Because of the number of tests used for each comparison, it was determined that the information could be more easily examined by averaging the data from the three replicate experiments. Therefore, for the remainder of this research study, the three stress-displacement responses and three vertical displacements are averaged for clarity in the comparison. The three replicate tests were also examined separately prior to averaging to ensure that no important differences or discrepancies were lost or overlooked because of the averaging. This examination included calculating the highest and lowest possible angles of shearing resistance for the test data, the difference in the high and low values, and the average angle of shearing resistance.

Table 3.3 Details of the verification experiments on sand specimens

Test Design	Void Ratio	Peak Shear stress (kPa)
V-M-50-D	0.45-0.52	41.3-42.0
V-M-100-D	0.48-0.53	78.04-79.0
V-M-150-D	0.48-0.53	123.18-127.80
V-P-50-D	0.48-0.53	40.7-42.0
V-P-100-D	0.48-0.53	69.4-75.2
V-P-150-D	0.48-0.52	111.0-119.6

Fig. 3.5 illustrates the stress-displacements and vertical displacements for the averaged curves at initial vertical stresses of 50 kPa, 100 kPa, and 150 kPa. At the initial vertical stress of 50 kPa, the full stress-displacement responses for the metal grid inserts and the PBBJ grid inserts are very similar. At 100 kPa and 150 kPa, the peak shear stresses and the post-peak stress-displacement responses show a very small amount of variation for the metal and the PBBJ grid plates. As shown in Fig. 3.4, however, it is no more variability than what would be expected in a series of tests repeated at the same conditions. The vertical displacement of the sand during shearing for specimens with the two different grid plates also agrees quite well with no considerable variation observed. At 50 kPa, the dilation is slightly higher for the specimens with PBBJ grid inserts than for the specimens with regular metal grid inserts, but at higher stresses the dilation was very similar and at 150 kPa the specimens with metal grid inserts actually exhibited slightly greater dilation. Hence, the vertical displacements of these tests reinforces the observation that the boundary material and surface characteristics have little to no influence on specimen response.

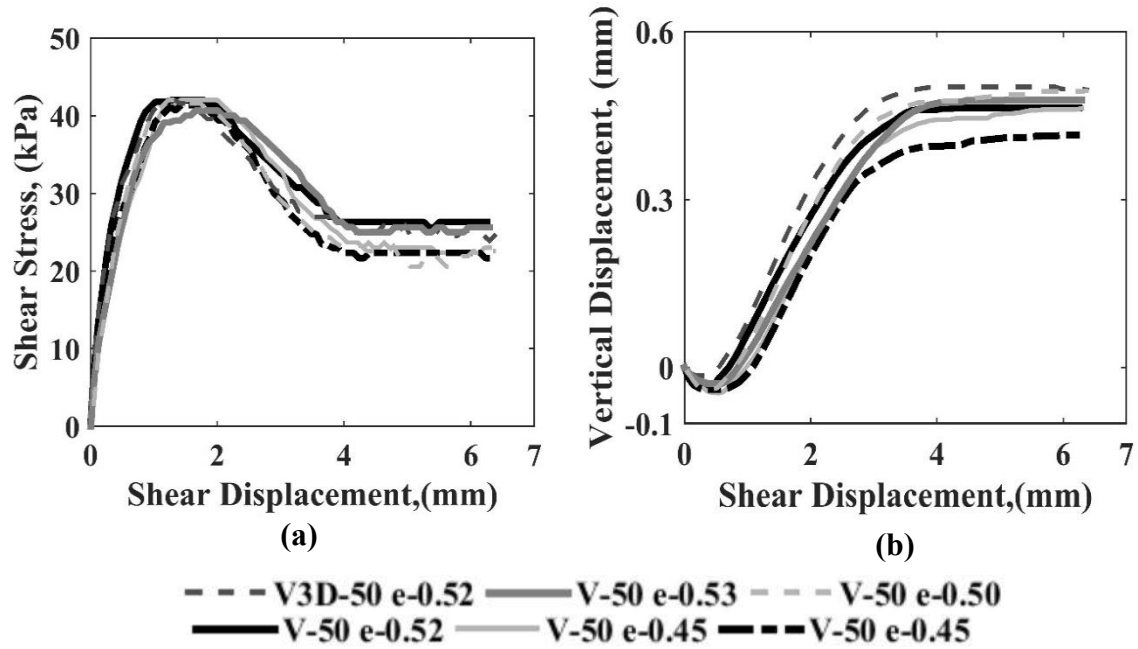


Fig. 3.4 Results of dense sand specimen configuration V-M-50-D and V-P-50-D

The average peak angle of shearing resistances, ϕ' , determined for the specimens with the metal and the 3D grid inserts with R1.5 are displayed in Fig. 3.6. The average ϕ' obtained for specimens with the metal grid inserts and the PBBJ inserts are 36.7° and 36.4° , respectively. Fig 3.5 presents the shear stress variation of the specimen without any area correction applied to the normal stresses and shear stresses. The peak shear stresses and friction angles obtained for the specimens with metal grid plate and PBBJ inserts were very close. Overall, there is no significant difference in the stress-displacement and vertical displacement responses of sand when the same geometrical grid inserts with two different materials are used. It should be noted that the PBBJ material used in this study is stiffer than many other similarly formed materials and it is likely that the boundary material must be sufficiently stiff to not influence the response. For the remainder of the study on the dense and loose specimens of sand and ball bearings, only PBBJ boundaries as described in Fig. 3.2 are used.

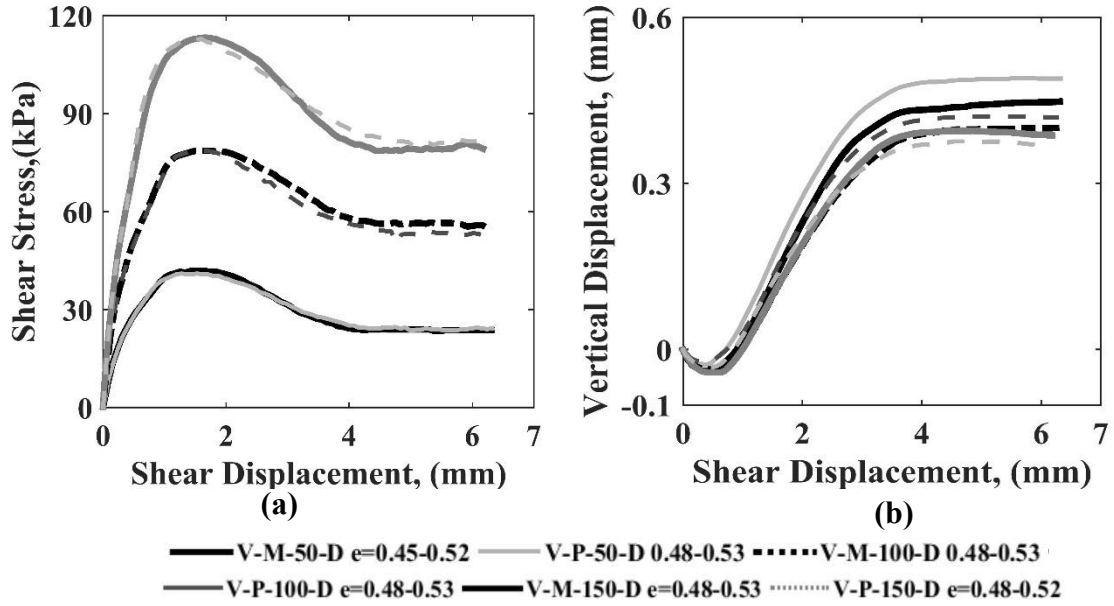


Fig. 3.5 Results of verification tests at vertical stresses of 50 kPa, 100 kPa and 150kPa

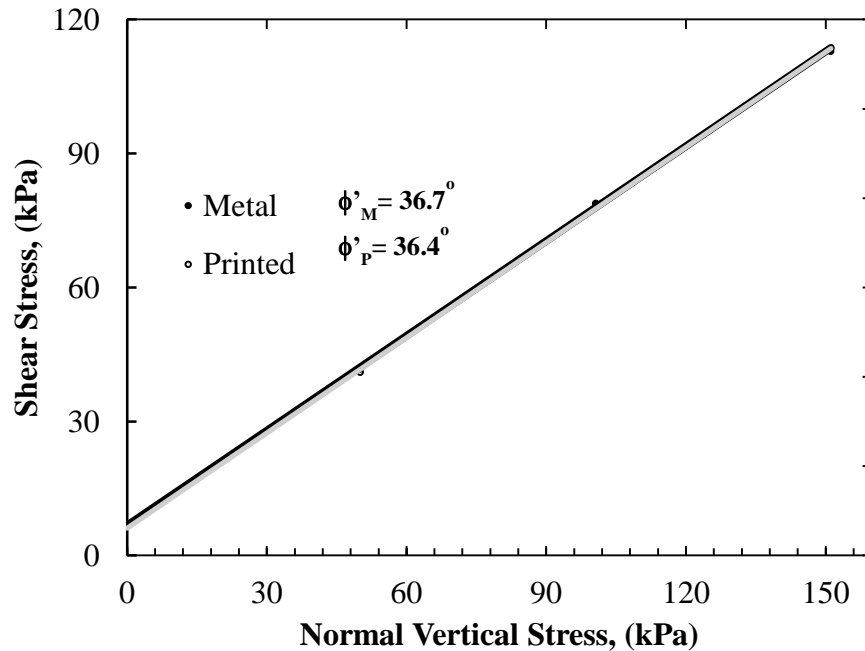


Fig. 3.6 Comparison of peak shear stress at select normal stresses for specimens with metal grid plates and PBBJ boundaries

3.3 Response of dense sand specimens

To understand the influence of boundary type on the shear behavior of dense Ottawa sand, a waffle stone boundary (W) along with R1.5, R4.8, T1.5, T4.8 and S boundaries were

used for experimental testing. Specimen void ratios and peak shear stresses for each set of tests are given in Table 3.4. While the volumes of the grid and sawtooth geometries were taken into account in the calculations, the differences in void ratios could be caused by slight measurement errors in the estimation of the volume occupied by the projected geometries. Therefore, for all the analyses, it was assumed that the specimens were actually at similar initial void ratios and that the differences observed were due to slight errors in the calculation of the total volume of the specimen when considering the boundary insert geometries. The average stress-displacement curves for the specimens with different boundaries indicate that the R1.5 grid boundary leads to different stress-displacement behavior when compared to the other boundary types (Fig. 3.7(a)). Specimens with the R1.5 grid boundaries exhibited the highest peak stress at all vertical stresses tested, with a 22% higher peak stress observed at 50 kPa when compared to the other specimens. The specimens with the R1.5 grid boundaries, also exhibited higher post peak-shear stress at 50 and 150 kPa initial vertical stresses. At 50 kPa and 100 kPa, all the other specimens show no considerable difference in their stress-displacement responses. However, at 150 kPa, the variability of the peak shear stresses for R1.5 boundary specimens are large, with a range of peak shear stresses varying from 94.6 kPa to 119.6 kPa for all the specimens with different boundaries. Specimens with the T4.8 grid boundaries exhibit the lowest peak shear stress at 150 kPa; however, this was not consistent at the other two vertical stresses.

The initial contraction of all the specimens are very similar, regardless of boundary type or vertical stress, as illustrated in Figs. 3.7(b), 3.7(c) and 3.7(d). The specimens with the waffle stone boundaries exhibited the highest average dilation of 0.5 mm at 50 kPa vertical stress, although the specimens with the R1.5 grid boundaries had a very similar response. The specimens with the R1.5 grid boundary have the highest dilation (0.45 mm) for tests conducted

at 100 kPa. While the specimens with the R1.5 and waffle stone boundaries consistently exhibited the highest dilation for the vertical stress range tested, there is little consistency in the responses observed for the remaining boundaries.

The average ϕ' , for all of the specimens are presented in Fig. 3.8. The values of high and low ϕ' as well as the differences between highest and lowest ϕ' from 3 replicate tests at the same initial stress are presented in Table 4. For specimens with the T4.8 grid boundary, the average ϕ' is 31.4 °, which is the lowest of all the specimens. The variations between high and low values of the replicate tests were also lower for T4.8 specimens. Because of the high peak shear stresses, the highest value of ϕ' (36.4 °) is obtained for specimens with the R1.5 grid boundaries. It is clear from Figs 3.6 and 3.7 that the boundary influences the response obtained for the dense sand specimens and that the R1.5 boundary leads to specimens which appear to have higher peak strength. Higher strength is usually associated with higher dilation, however, at 150 kPa, the highest dilated specimens are specimens with waffle stones, when specimens with R1.5 boundaries have next higher dilation. The difference between the highest and lowest ϕ' values obtained for specimens with R1.5 boundaries is 3.7 °, which is the highest of all other specimens.

Table 3.4 Details of the experiments on dense sand specimens

Test designation	Void ratio	Peak Shear stress (kPa)	ϕ'_{low} , (°)	ϕ'_{high} , (°)	$\phi'_{high} - \phi'_{low}$, (°)	Average ϕ' , (°)	Intermediate, ϕ' , (°)
R1.5-50-D	0.48-0.53	40.7-42.0					
R1.5-100-D	0.48-0.53	69.4-75.2	34.3	38.0	3.7	36.4	36.8
R1.5-150-D	0.48-0.52	111.0-119.6					
R4.8-50-D	0.46-0.48	31.8-33.8					
R4.8-100-D	0.45-0.46	65.2-69.9	33.9	37.1	3.2	35.3	34.7
R4.8-150-D	0.45-0.46	101.7-108.3					
T1.5-50-D	0.46-0.47	35.2-37.4					
T1.5-100-D	0.46-0.48	64.3-71.0	31.9	35.4	3.5	33.6	33.1
T1.5-150-D	0.45-0.47	100.4-107.0					
T4.8-50-D	0.51-0.52	34.0-36.0					
T4.8-100-D	0.5-0.51	67.0-69.9	30.6	32.2	1.6	31.4	32.2
T4.8-150-D	0.51	95.7-97.7					
S-50-D	0.46-0.48	33.6-36.7					
S-100-D	0.46-0.47	66.3-72.3	31.4	34.8	3.4	33.4	32.8
S-150-D	0.47-0.48	98.4-107.0					
W-50-D	0.46-0.47	33.6-35.6					
W-100-D	0.47	68.3-70.3	34.1	36	1.9	35	35.1
W-150-D	0.45-0.47	104.1-107.0					
N-50-D	0.49-0.50	29.2-31.4					
N-100-D	0.5	61.9-66.3	32.9	35	2.1	33.7	33.8
N-150-D	0.5	94.6-102.1					

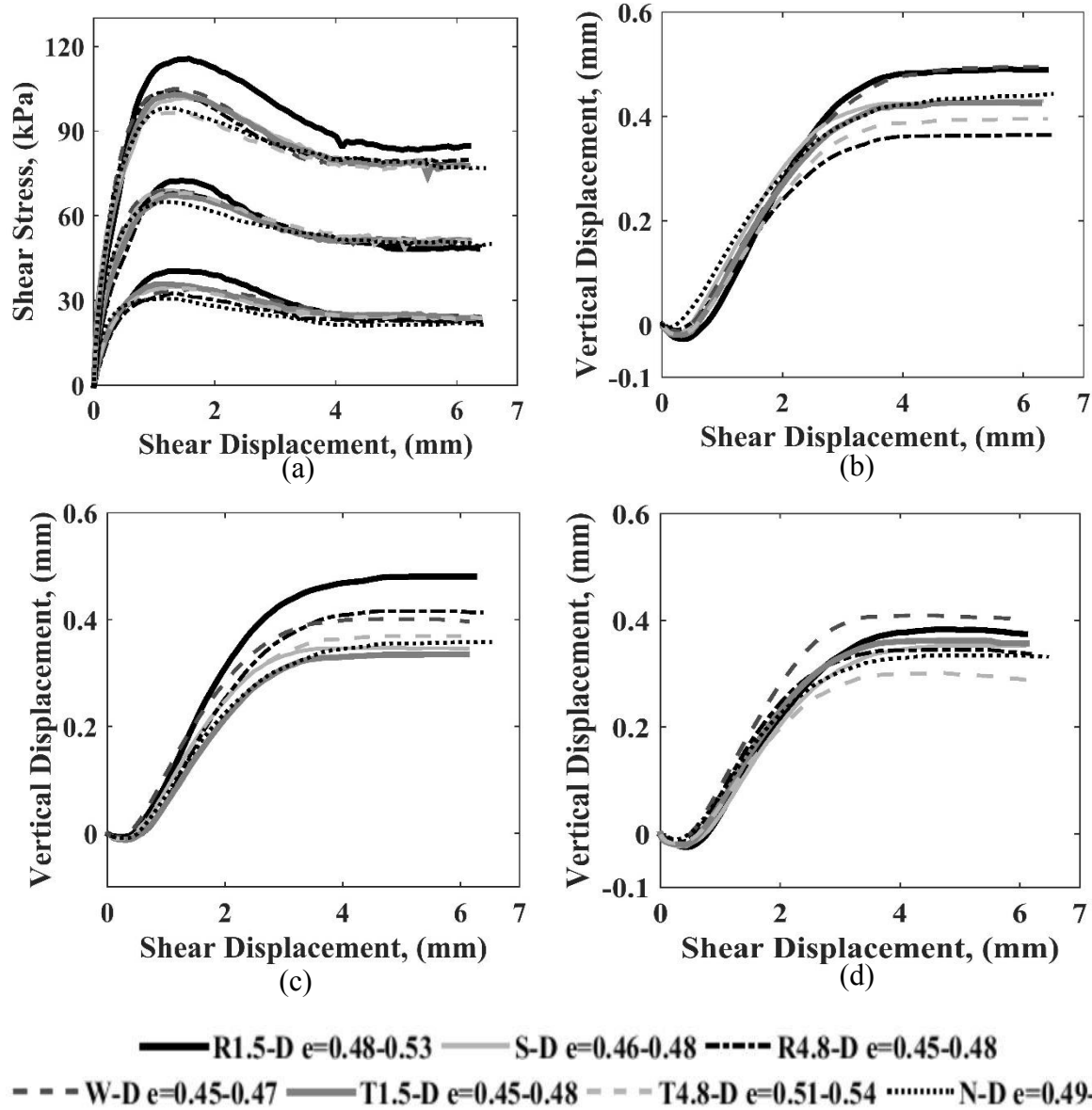


Fig. 3.7 Results of dense sand specimen configurations N, R, S, T and W, (a) stress-displacement response, and vertical displacements at (b) 50 kPa, (c) 100 kPa, and (d) 150 kPa

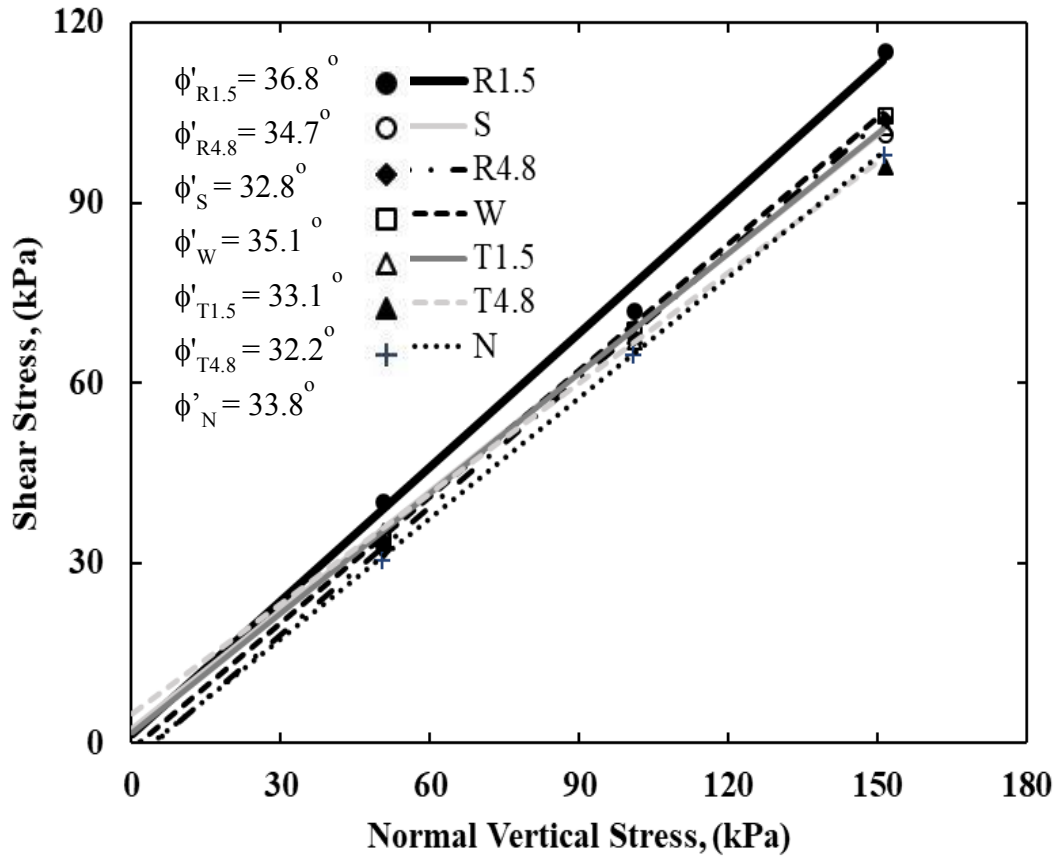


Fig. 3.8 Average peak angle of shearing resistance of dense sand specimens with different boundaries

3.4 Response of loose sand specimens

Experiments were performed on the loose sand specimens with R1.5, R4.8, T1.5, T4.8, S and W boundaries. The ranges of void ratios tested for the loose sand specimens, along with the corresponding peak shear stresses are given in Table 3.5. The average peak shear stresses for specimens with the R1.5 boundaries are 4% higher than other specimens. From Table 3.5, it can be noted that the range of peak shear stresses of the sawtooth specimen at 50 kPa varies from 25.0 kPa-28.5 kPa, even though the void ratios were consistent. Overall, the results of the loose sand specimens exhibited similar trends to the dense sand specimens, with the specimen with

R1.5 grid boundary in having the highest peak shear stresses (Fig. 3.9(a)). As expected, the peak shear stresses of the loose specimens are lower than the dense specimens.

Table 3.5 Details of the experiments on loose sand specimens

Test designation	Void ratio	Peak shear stress (kPa)	ϕ'_{low} , (°)	ϕ'_{high} , (°)	$\phi'_{high} - \phi'_{low}$, (°)	Average ϕ' , (°)	Intermediate, ϕ' , (°)
R1.5-50-L	0.79-0.82	23.9-26.5					
R1.5-100-L	0.76-0.79	54.4-57.5	30.5	33.7	3.2	32.1	32.0
R1.5-150-L	0.77-0.80	83.3-94.0					
R4.8-50-L	0.77-0.80	24.3-26.5					
R4.8-100-L	0.77-0.80	56.2-57.7	28.9	31.5	2.6	30.1	29.9
R4.8-150-L	0.77-0.80	82.2-86.2					
T1.5-50-L	0.75-0.78	23.9-25.6					
T1.5-100-L	0.76-0.8	55.5-56.2	30.0	30.9	0.9	30.5	30.6
T1.5-150-L	0.77-0.78	84.0-84.2					
T4.8-50-L	0.77-0.80	22.1-24.8					
T4.8-100-L	0.78-0.80	54.8-55.9	27.2	31.0	3.8	29.5	29.9
T4.8-150-L	0.79-0.80	76.7-82.9					
S-50-L	0.81	25.0-28.5					
S-100-L	0.79-0.81	55.3-55.7	28.1	30.1	2.0	29.0	28.7
S-150-L	0.80-0.81	82.9-83.6					
W-50-L	0.81-0.83	23.0-25.2					
W-100-L	0.77-0.8	51.3-57.0	29.4	31.4	2.0	30.2	30.5
W-150-L	0.77-0.8	82.2-84.7					

The vertical displacement of the specimens presented in Figs 3.9(b), 3.9(c) and 3.9(d) indicate that overall, the specimens exhibited higher variability at vertical stresses of 50 kPa and 150 kPa. Also, the variability observed in the vertical displacements did not correspond with the void ratios tested. At 50 kPa, the specimens with T1.5 boundaries have the highest contraction (0.3 mm) while the lowest contraction is exhibited by specimens with the R4.8 boundaries (0.1 mm). The specimens with sawtooth boundary have the highest contraction at 150 kPa vertical

stresses (0.3 mm). The magnitude of the contraction exhibited by the specimens did not follow any trends. In other words, the loosest specimens or those with the largest void ratio did not necessarily demonstrate the highest amount of contraction.

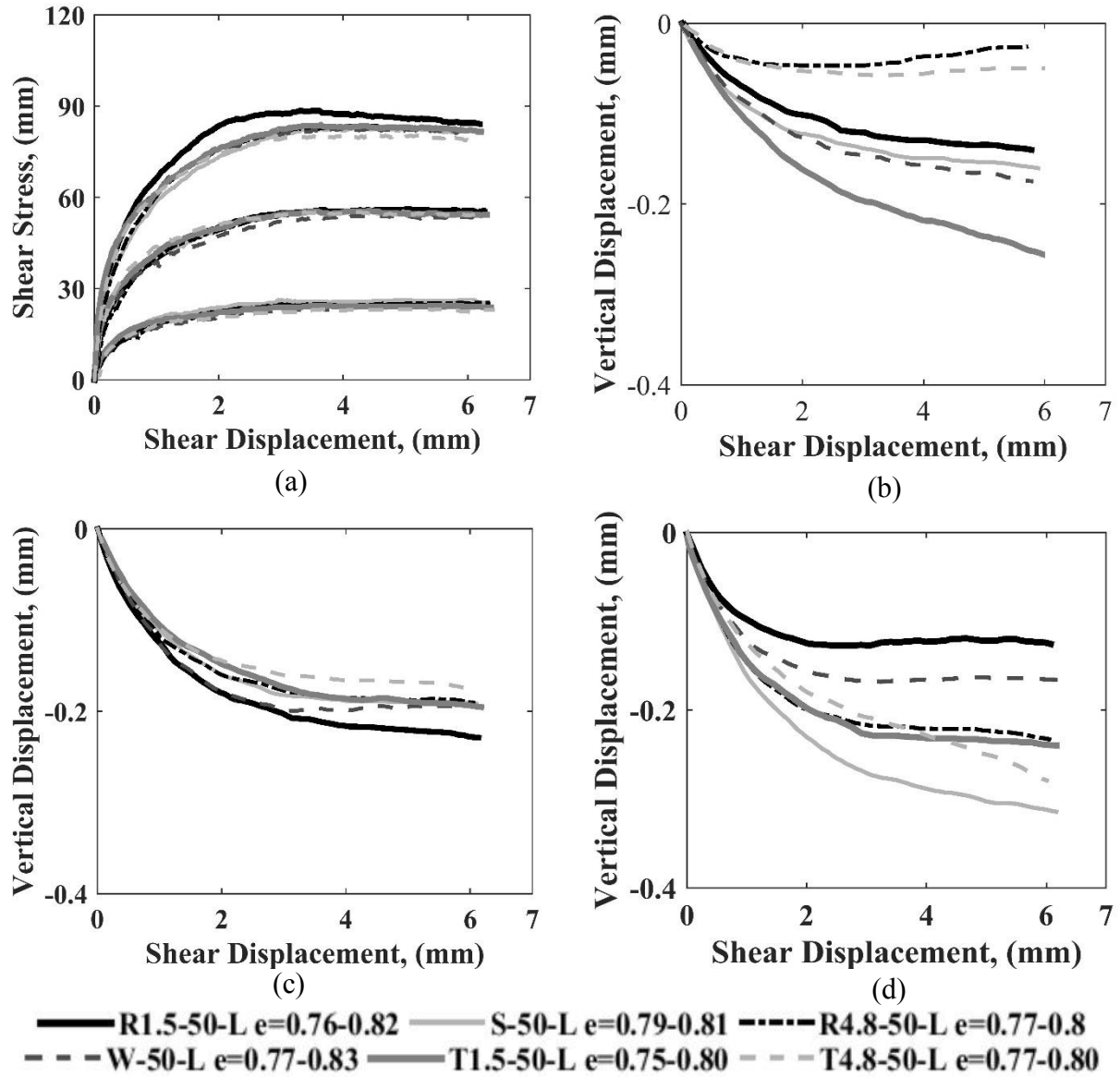


Fig. 3.9 Results of loose sand specimen configuration R, S, T and W, (a) stress-displacement response, and vertical displacements at (b) 50 kPa, (c) 100 kPa, and (d) 150 kPa

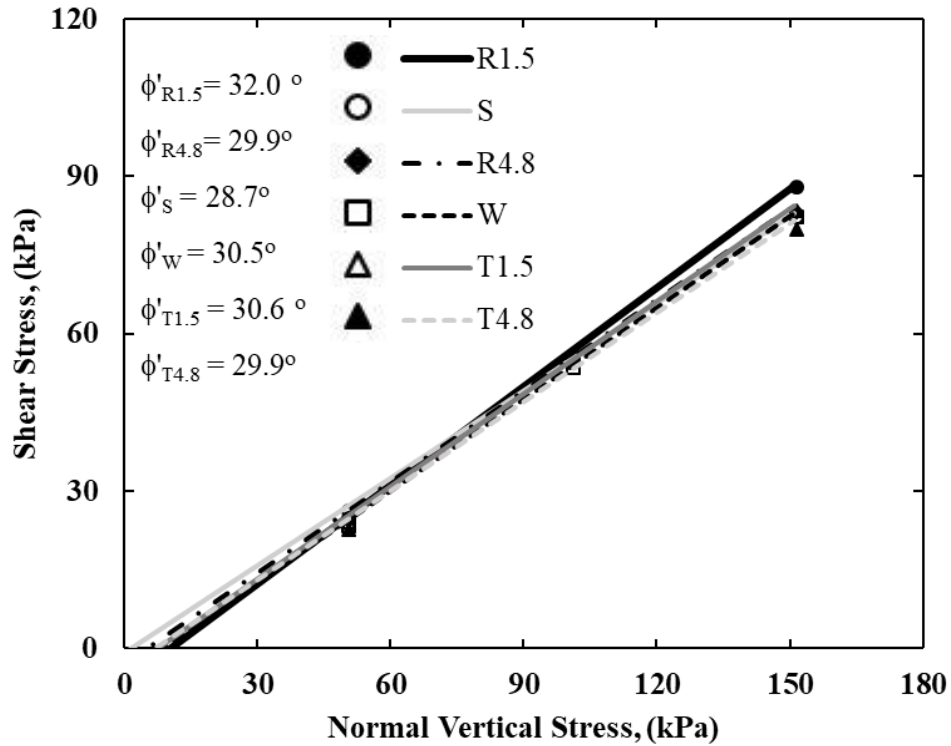


Fig. 3.10 Average peak angle of shearing resistance of loose sand specimens with different boundaries

The average ϕ' obtained from the peak stresses are presented in Fig. 3.10 and the highest and lowest ϕ' values from the replicate tests are summarized in Table 3.5. The average ϕ' is lower for specimens with the T1.5 and T4.8 grid boundaries, similar to the average ϕ' obtained for the dense sand specimens. Also, similar to the dense sand specimen results, the loose specimens with the R1.5 grid boundary have the highest ϕ' of 32.0° and but T4.8 specimens have the highest difference (3.8°) between the lowest and highest ϕ' obtained from the three replicate tests. The R1.5 specimens have a difference of 3.2° between the three replicate tests. For all specimens with different boundaries, the lowest variation among the replicate tests was found for specimens with T1.5 boundary as given in Table 3.5. Overall, the ϕ' values obtained varied from 29.0 o to 32.1°, indicating that the boundary geometry does influence the response, although the

range for the loose specimens was slightly less than the range observed for the dense sand specimens.

3.5 Response of dense ball bearing specimens

Because of its use in numerical simulations on idealized granular material, a fixed-particle boundary, as demonstrated in Fig. 3.2(f) was also tested along with S, R1.5, R4.8, T1.5 and T4.8 boundaries for the experiments on the dense ball bearing specimens. For the fixed-particle boundary, ball bearings were glued to a flat PBBJ plate and used in the experiment. The range of void ratios and peak shear stresses of the dense ball bearing specimens with the different type of boundaries are given in Table 3.6. As discussed, the volume of the grid and sawtooth geometries were considered while calculating the volume of the specimen, however, the fixed-particle boundary had excess epoxy in some regions which was not considered in the calculations. All the specimens with fixed-particle boundaries were created with a very little variation in void ratio, in their densest state possible and therefore, for the analyses it was assumed that all the specimens were at similar initial void ratios. As presented in Fig. 3.11(a), the stress-strain response is similar for all the specimens with one exception being that the average peak shear stress of the specimens with fixed-particle boundaries is 5% greater at 100 kPa initial vertical stress than the other specimens. As expected, the dense ball bearing specimens have lower peak stresses when compared to the dense sand specimens at all initial vertical stresses. For example, at 150 kPa initial vertical stress, the sand and ball bearing specimens with the R1.5 boundaries exhibit higher peak stress. The sand specimens with the R1.5 boundaries have a peak stress of 119.6 kPa whereas the ball bearing specimens with the R1.5 boundaries have a peak shear stress of 76.5 kPa. This was expected since the ball bearings are smooth spheres and do not exhibit the interlocking that is observed in a more angular, sand particle.

Although the results are very similar, specimens with the sawtooth boundary and the specimens with T4.8 grid boundary have the lowest peak shear stresses at the vertical stresses tested.

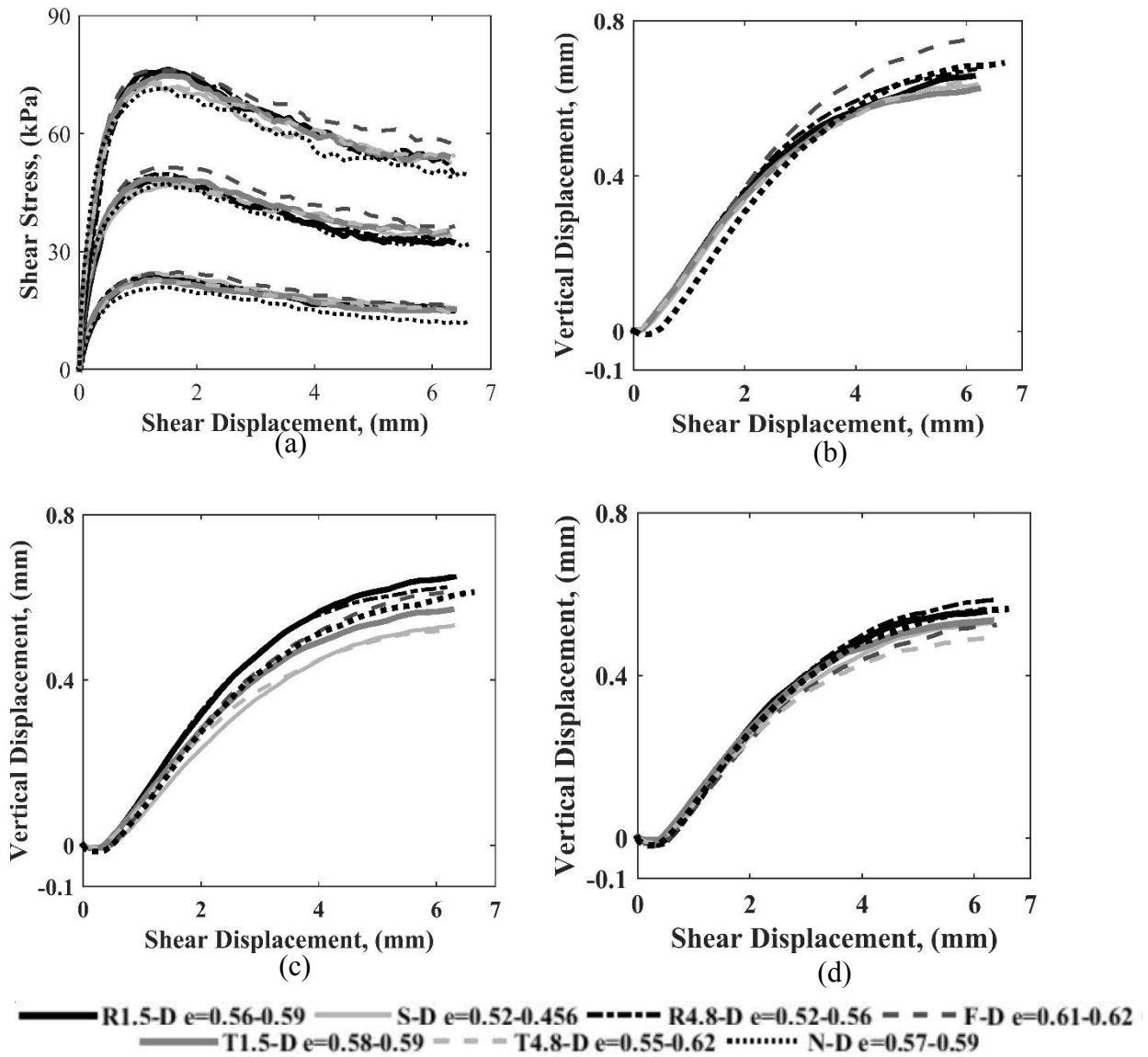


Fig. 3.11 Results of dense ball bearing specimens, configurations N, R, S, T and F (a) stress-displacement response, and vertical displacements at (b) 50 kPa, (c) 100 kPa, (d) 150 kPa

Table 3.6 Details of the experiments on dense ball bearings

Test designation	Void ratio	Peak Shear stress (kPa)	ϕ'_{low} , (°)	ϕ'_{high} , (°)	$\phi'_{high} - \phi'_{low}$, (°)	Average ϕ' , (°)	Intermediate, ϕ' , (°)
R1.5-50-D	0.57-0.59	21.4-24.5					
R1.5-100-D	0.56-0.57	47.3-49.5	26.9	28.6	1.7	27.9	27.4
R1.5-150-D	0.57-0.56	75.8-76.5					
R4.8-50-D	0.54-0.55	22.1-24.5					
R4.8-100-D	0.53-0.54	48.6-52.2	25.7	29.2	3.5	27.4	27.5
R4.8-150-D	0.52-0.56	73.2-78.5					
T1.5-50-D	0.58-0.59	21.4-23.4					
T1.5-100-D	0.58-0.59	48.2-50.4	26.2	28.9	2.7	27.3	27.4
T1.5-150-D	0.58-0.59	73.2-77.2					
T4.8-50-D	0.55-0.61	22.6-22.8					
T4.8-100-D	0.61	47.3-48.9	26.4	26.9	0.5	26.6	26.7
T4.8-150-D	0.55-0.62	73.0-73.6					
S-50-D	0.57-0.59	23.9-24.8					
S-100-D	0.58-0.60	46.2-47.1	25.2	26.5	1.3	25.6	25.6
S-150-D	0.58-0.57	72.3-74.3					
F-50-D	0.61	24.1-25.6					
F-100-D	0.61-0.62	51.3-51.7	25.8	27.9	2.1	26.9	27.2
F-150-D	0.61-0.62	74.5-77.6					
N-50-D	0.57-0.58	20.6-24.1					
N-100-D	0.57-0.58	46.9-48.2	25.8	27.7	1.9	26.7	26.5
N-150-D	0.58-0.59	70.5-73.6					

Similar to the dense sand experiments, the initial contraction is the same for all the dense ball bearing specimens. As expected, the plots of vertical displacement at the three vertical stresses in Fig. 3.11(b), 3.11(c) and 3.11(d) shows that the amount of dilation is reduced as the vertical stress increases. Comparisons of the vertical displacements for the individual boundary type specimens showed that at 50 kPa and 100 kPa vertical stresses, specimens with the sawtooth boundary showed the least amount of dilation. For instance, at 50 kPa vertical stress, the highest

dilation is exhibited by the specimens with fixed-particle boundary (0.75 mm) and the specimens with the sawtooth boundary have the least amount of dilation (0.6 mm). At 150 kPa, the lowest and highest vertical displacements are 0.48 mm (specimens with T4.8 boundaries) and 0.57 mm (specimens with R4.8 boundaries), respectively. The overall variation between the different specimens is much smaller for the ball bearing specimens than it is for the sand specimens. This is also likely because the particles are spherical and smooth. The average ϕ' for the dense ball bearing specimens is much lower than the ϕ' for the dense sand specimens, as presented in Fig. 3.12.

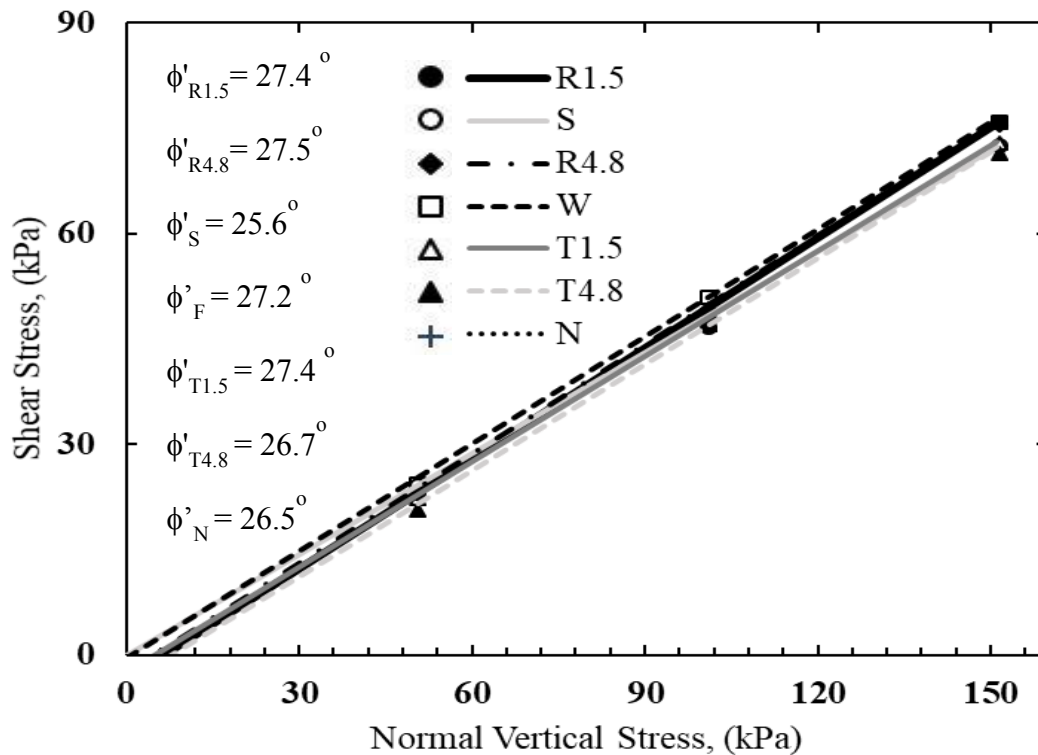


Fig. 3.12 Average peak angle of shearing resistance of dense ball bearing specimens with different boundaries

The ϕ' values from the replicate tests were examined individually before averaging, to obtain the highest and lowest values of ϕ' which are presented with the average ϕ' obtained in

Table 3.6. When $\phi'_{\text{high}} - \phi'_{\text{low}}$ for all the specimens are compared, the specimens with R1.5 boundaries have highest difference ($\phi'_{\text{high}} - \phi'_{\text{low}} = 1.8^\circ$) among the replicate tests which is similar to what was observed for the dense and loose sand specimens with the R1.5 boundaries. The highest ϕ' ($\phi'=27.5$ and 27.4) is observed for specimens with the R1.5 and R4.8 boundaries, whereas the specimens with the sawtooth boundary have the lowest average friction angle ($\phi'=25.6^\circ$) of all the specimens tested. It is likely that the ball bearings can move up and over the triangular ridges of the sawtooth boundary more easily when compared to rectangular ridges of R1.5 or similar boundaries. This could explain the reason why the strength appears to be lower for the specimens with the sawtooth boundary.

3.6 Response of loose ball bearings

Experiments were also conducted on loose ball bearing specimens with boundaries R1.5, R4.8, T1.5, T4.8, S, and F. The void ratios of the specimens and their respective peak shear stresses together with ϕ' are summarized in Table 3.7. The averaged stress-displacement and vertical displacements obtained are illustrated in Fig. 3.13. Largest variability in peak shear stresses was obtained for specimens with R4.8 boundary plates (12.8 - 16.8 kPa). Sawtooth boundary specimens have lowest variability in peak stresses (14.1 kPa - 14.8 kPa). Lowest variability was for specimens paired with sawtooth boundaries. At all the three vertical stresses, the specimens with the T4.8 grid boundary exhibit the highest peak stresses which are approximately 10% higher than all other specimens, whereas the specimens with the sawtooth boundaries show the lowest peak stresses (Fig. 3.13 (a)).

Table 3.7 Details of the experiments on loose ball bearing specimens

Test designation	Void ratio	Peak Shear stress (kPa)	ϕ'_{low} , (°)	ϕ'_{high} , (°)	$\phi'_{high} - \phi'_{low}$, (°)	Average ϕ' , (°)	Intermediate, ϕ' , (°)
R1.5-50-L	0.69	16.1-16.8					
R1.5-100-L	0.65-0.68	32.7-36.3	20	22.4	2.4	21.2	22.0
R1.5-150-L	0.68-0.71	53.5-57.7					
R4.8-50-L	0.66-0.68	12.8-16.8					
R4.8-100-L	0.65-0.68	33.4-37.4	22.4	24.1	1.7	23.1	22.9
R4.8-150-L	0.66-0.69	54.4-57.9					
T1.5-50-L	0.70-0.71	16.8-19.7					
T1.5-100-L	0.70-0.72	34.7-37.4	20.2	22.6	2.4	21.2	21.6
T1.5-150-L	0.70-0.72	56.8-58.8					
T4.8-50-L	0.70-0.71	18.8-20.1					
T4.8-100-L	0.70-0.72	38.9-40.9	20.2	22.5	2.3	21.2	21.8
T4.8-150-L	0.71-0.72	57.3-60.6					
S-50-L	0.65-0.69	14.1-14.8					
S-100-L	0.67-0.7	33.4-35.4	21.9	22.1	0.2	21.8	22.1
S-150-L	0.68-0.69	55.4-55.9					
F-50-L	0.71-0.72	16.4-17.7					
F-100-L	0.71-0.72	34.9-36.3	20.4	21.4	1	20.9	20.8
F-150-L	0.70-0.72	53.9-57.3					

The vertical displacement of all the specimens at the three different vertical stresses showed that specimens with the T1.5 boundaries have significantly high contraction (0.6 mm) at 50kPa, while the other specimens have an average contraction ranging from 0.1-0.3 mm. A similar trend is observed at 100 kPa and 150 kPa, even though the void ratios of the specimens with T1.5 boundaries are similar to the other specimens tested. These results were further examined individually before averaging the responses and it was found that all three of the experiments yield the same trends shown in Fig.s 3.13(b), 3.13(c) and 3.13(d). In each of the cases, the top boundary cap was carefully placed so that the specimen remained in its loosest

possible state. For 50 kPa and 100 kPa, the lowest contraction is for specimens with the sawtooth boundary. At 150 kPa, the lowest contraction is observed for specimens with the T4.8 grid boundary.

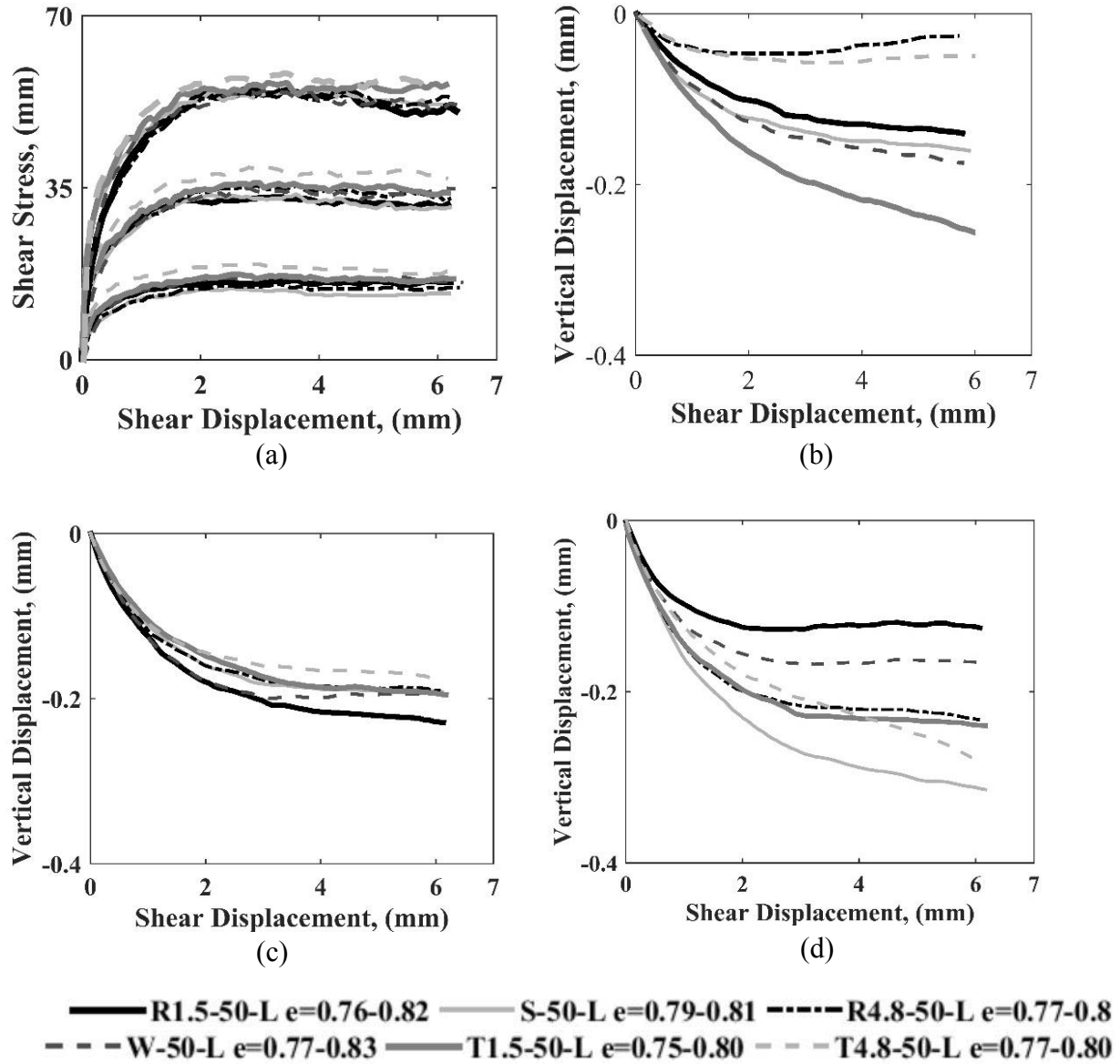


Fig. 3.13 Results of loose ball bearing specimen configuration R, S, T and F (a) stress-displacement response, and vertical displacements at (b) 50 kPa, (c) 100 kPa, and (d) 150 kPa

Specimens with the R1.5, T1.5 and T4.8 grid boundaries have variability of friction angles greater than 2° (Table 3.7). As demonstrated in Fig. 3.14 and Table 3.7, the loose ball

bearing specimens have the lowest average ϕ' of all the specimens tested. Similar to sand specimens and dense ball bearing specimens, specimens with R1.5 and T1.5 boundaries have the largest variation of ϕ' ($\phi'_{\text{high}} - \phi'_{\text{low}} = 2.4^\circ$) among the replicate tests. Overall, all the specimens with different boundaries, the average ϕ' varied from 20° to 22.6° . Of the loose ball bearing specimens, the highest ϕ' is obtained for the specimens with the R4.8 boundary ($\phi' = 23.1^\circ$) and the all other boundaries had friction angle values varying from 20.9 - 21.8° . Therefore, in loose and dense specimens of ball bearings, the strength of the specimens did not have much variation.

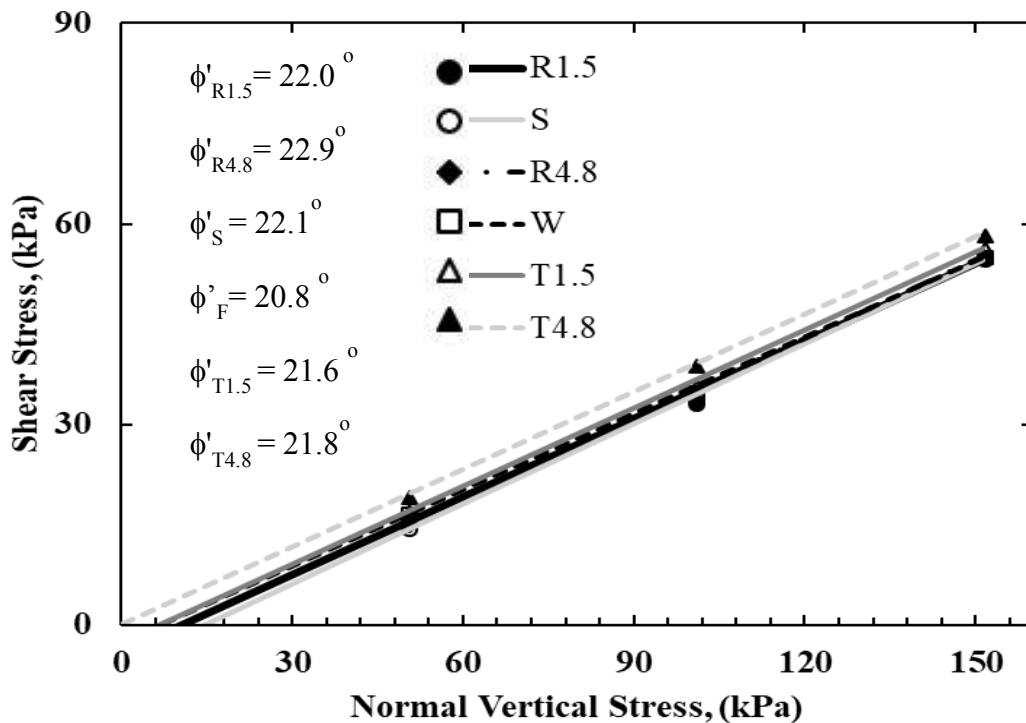


Fig. 3. 14 Average peak angle of shearing resistance of loose ball bearing specimens with different boundaries

3.7 Conclusions

Direct shear tests on dense and loose Ottawa sand specimens and precision ball bearing specimens were performed using seven different types of boundaries. The results were then

examined to determine the influence of the boundary type on the stress-displacement and vertical displacement responses of the granular materials. Overall, it can be concluded that the boundary type does affect the overall shear response of sand and the idealized granular material, although a consistent trend was difficult to determine. The response patterns tended to change for specimens with each type of boundary and for the vertical stresses tested.

Tests indicated that dense sand specimens with R1.5 grid boundaries exhibited 14% higher peak shear stress on average when compared to the other boundary types, while loose sand specimens with this same boundary exhibited 4% higher peak shear stress on average. The specimens with the T4.8 grid boundary exhibited the lowest strength in the sand tests. Dense specimens of ball bearings with the R1.5 grid boundary exhibited slightly higher strength; however, this same trend was not observed for the loose ball bearing specimens. For the dense ball bearing specimens, the specimens with the sawtooth boundary exhibited the lowest overall peak strength.

Overall, it is clear that the boundary does influence the results; however, it is difficult from these macro-scale results to single out the mechanisms leading to the observed behavior. One conclusion that can be drawn is that the idealized ball bearings are not necessarily representative of the sand, thus the research hypothesis that *the use of suitable idealized granular material can lead to a better understanding of granular behavior in laboratory studies and in DEM validation studies* is not true when only considering laboratory results. More realistic particle shapes are needed to better represent the granular materials of interest in geotechnical studies; however, the idealized material may still lead to an improved generalized understanding of granular material when coupled with validated DEM simulations. To examine this, the results

from the direct shear tests on the idealized granular material were used for experimental validation of DEM simulations of spherical particles as presented in the next chapter.

CHAPTER 4: DEM DIRECT SHEAR STUDY TO EXAMINE EFFECTS OF BOUNDARY FRICTION

4.1 Introduction

From the experimental testing of the dense and loose steel ball bearings and sand direct shear specimens, it was concluded that, even though there were differences in the results for specimens with different types of boundaries, the overall data were not sufficient to draw concrete conclusions. Therefore, DEM models were used to further examine the influence of the boundary interaction with the metal ball bearing specimens. Two simulations were developed for the boundary plate with no projections and the top and bottom boundary caps were given a low friction coefficient of 0.0, and a high boundary friction value of 10.0. Only the dense specimens were modeled because of the fact that the influence in boundary type was more prevalent in these specimens. Although these simulations do not examine the influence of the boundary projections, they provide a simple means to study the sliding and rolling interactions of the particles with the boundaries and they can be used as a validation comparison with the laboratory data gathered. This chapter discusses the details such as specimen preparation, contact models, and input parameters for the dense DEM specimens. A comparison of the DEM simulations with experimental data is presented to serve as the validation of the models. Micro mechanical behavior including particle interactions, contact forces and stresses were analyzed for the DEM models and plots are discussed herein.

4.2 Specimen preparation

Dense DEM specimens were prepared using 29,298 spheres to replicate the steel ball bearing specimens used in the experimental testing. All DEM specimens were prepared in

PFC3D to try and match the void ratios of the specimens prepared in the laboratory. Then these virtual specimens were imported into LIGGGHTS to conduct the shearing part of the simulation to reduce computation time. The results were analyzed using MATLAB and specimen visualization was conducted with PARAVIEW. LIGGGHTS was chosen as the software platform for the shearing part of the simulations because of the increased speed of the simulation due to parallel processing capabilities and the ability to run more simulations simultaneously.

To prepare the specimens, first, a random assembly of spheres was generated as a non-contacting cloud with three diameters of spheres (Table 4.1) in a tall cylinder with a diameter of 63.5 mm and a height of five times the diameter, as shown in Fig 4.1. In order to replicate air pluviation and create a specimen similar to what is used in laboratory tests, the bottom wall of the tall cylinder is deleted, and the particles are allowed to fall freely under gravity and settle until equilibrium is established. The particles settle into the bottom of the cylindrical direct shear box (replicated by two stacked thick-walled cylinders) of diameter 63.5mm and a height of 31.75mm. Once in equilibrium, the top cap is lowered into position until a desired normal stress is achieved. A normal stress of 50 kPa was targeted for the DEM simulations. Table 4.1 shows the input parameters for the DEM simulations using the Hertz-Mindlin contact model. The reduced values of Young's modulus were used in the simulations to reduce the computational cost (O'Sullivan, Bray, & Li, 2004; Cui & O'Sullivan, 2006). The generated specimens had a void ratio of 0.64. Since these were higher than the laboratory specimens tested, the particles were subjected to rotations in specific directions to achieve a lower void ratio.

Table 4.1 Specimen size and particle diameters for DEM Fric10.0 and DEM Fric0.0.

Specimen configuration	Number of particles	Nominal diameter (mm)
Fric_0.0	29298	1.19
		1.59
		1.98
Fric_10.0	29298	1.19
		1.59
		1.98

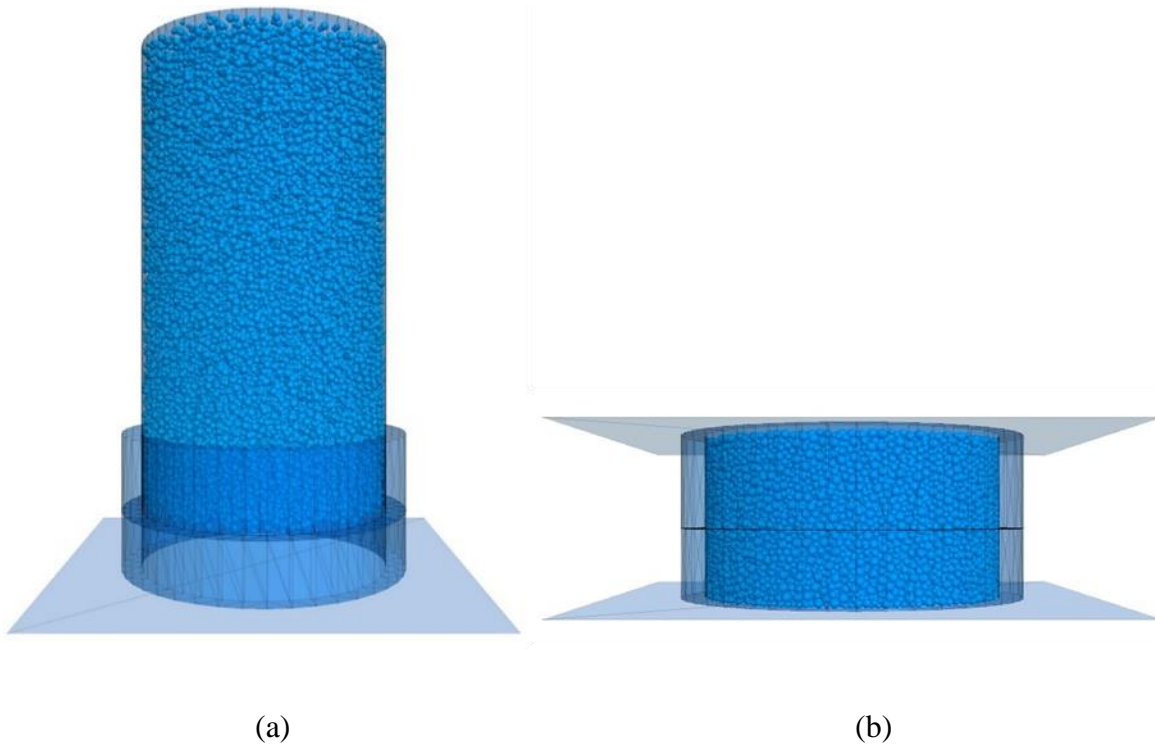


Fig. 4.1(a) Cloud of non-contacting particles, and (b) particles settled into direct shear box in PFC 3D

To achieve the densification in the specimen, first a lower inter-particle friction coefficient was applied, and the system is allowed to equilibrate. Then the original friction value of 5.5 ° is reapplied, followed by spinning the particles in three layers to reestablish the shear forces. Without reestablishing the shear force, the initial stiffness of the specimens is fictitiously

high. To spin the particles, they are divided into three groups along the height of the specimen where the lower 1/3 of the particles were assigned to group 'one', particles from 1/3 to 2/3 of the height assigned group 'two' and the top 1/3 assigned group 'three'. These ball groups were set to an angular velocity of 1.0×10^{-2} rad/s. Group 'one' is allowed to spin in the x direction whereas group 'two' and 'three' were set to spin in the y and z directions, respectively. These were allowed to spin for 1,000,000 cycles to equilibrate the system and the void ratio was rechecked when the top cap reached a stress of 50 kPa. The void ratio obtained in the DEM specimens was 0.061 which is close to the void ratio of the dense laboratory specimens (0.57-0.59), although the exact void ratio was not achieved. At this point, the particle positions were exported into LIGGGHTS for the shearing phase.

Two specimens were created with the same initial particle positions, one with the top and bottom boundary cap friction coefficients set to 0.0 and another with the boundary friction coefficients set to 10.0. They are denoted as DEM Fric0.0 and DEM Fric10.0 respectively. As discussed, the two extreme friction values were used in order to understand if the friction at the boundary caps affected the macro-scale or micro-scale behavior of the dense specimens. The setup of the specimen prior to shearing is illustrated in Fig 4.2. The top and bottom boundary caps are different from that of Figure 4.1(b) because in LIGGGHTS servo control can only be used if the meshes are .STL files. Hence, they were designed in AutoCAD and imported to the locations at the top and bottom cylinders and aligned axially in the z (i.e., vertical) direction. The top cap was placed so that the plate was not in contact with the top most particle. The servo control was used to keep the top cap in position, as well as to achieve contact with the particles before shearing. The bottom cap and cylinder were moved horizontally at a constant shearing rate of 1.0×10^{-5} m/s. The top cap moved vertically to allow the dilation of the specimen during

shearing. The radii of the measurement spheres set up for the localized measurements were 12mm each. The input parameters used in the simulation are presented in Table 4. 2.

Table 4.2 Material properties used in the DEM Simulation

Property	Value
Poisson's ratio	0.3
Shear modulus	$21.0 \times 10^9 \text{ N/m}^2$
Coefficient of restitution	0.6
Density	7780 kg/m^3
Interface friction angle	5.5°
Interface friction angle direct shear box	10.0
Interface friction for boundary plates	0.0 (tangent value 0.0) and ≈ 84.5 (tangent value 10.0)

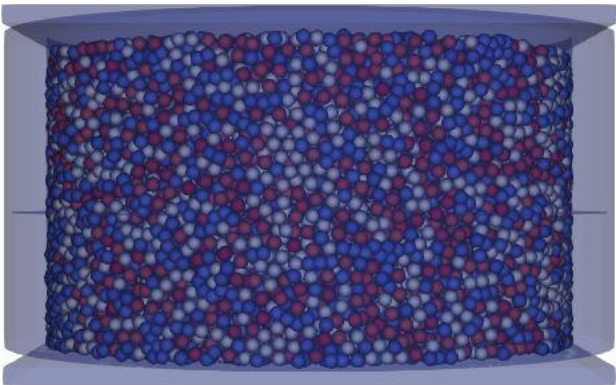


Fig. 4.2 Specimen set up in LIGGGHTS before starting shearing

The results are presented and analyzed in the following sections. The overall specimen behavior in terms of the stress-displacement response and the displacement in the vertical

direction was compared for the DEM and experimental data. The results are presented and analyzed in the following sections. The simulation results (denoted as DEM Fric10.0 and DEM Fric0.0) are compared with the laboratory specimens tested with no projections on the boundaries (denoted as Exp N).

4.3 Results and discussions

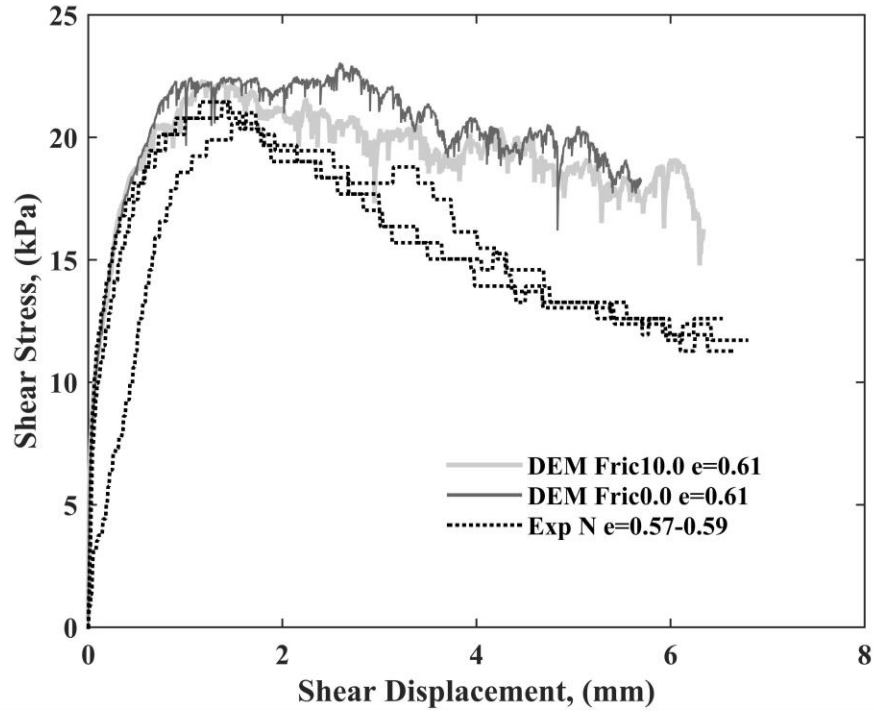
4.3.1 Comparison of overall behavior of specimens with experimental data

The shear stress was recorded for the bottom cylinder wall for the DEM specimen and was plotted with the similar measurement made for the experimental data (Fig. 4.3). At the beginning of shearing, the DEM simulations capture the experimental behavior very closely. These simulations capture the low strain stiffness observed in the experimental testing which has proven difficult to do in dense particle assemblies in DEM because of the specimen preparation techniques (Bernhardt et al., 2016). As the specimens reached the peak shearing stresses, the DEM specimens had a slightly higher peak stress when compared to the experimental specimens. The response of the high friction and low friction simulations were very similar in terms of the initial stiffness; however, at the peak shear stress, DEM Fric10.0 is slightly lower than DEM Fric0.0. While there is a delay in strain softening for DEM Fric0.0, the specimen eventually strain-softens and reaches similar a stress-strain response as DEM Fric10.0. Neither of the DEM simulations exhibit the amount of strain softening observed in the experimental results.

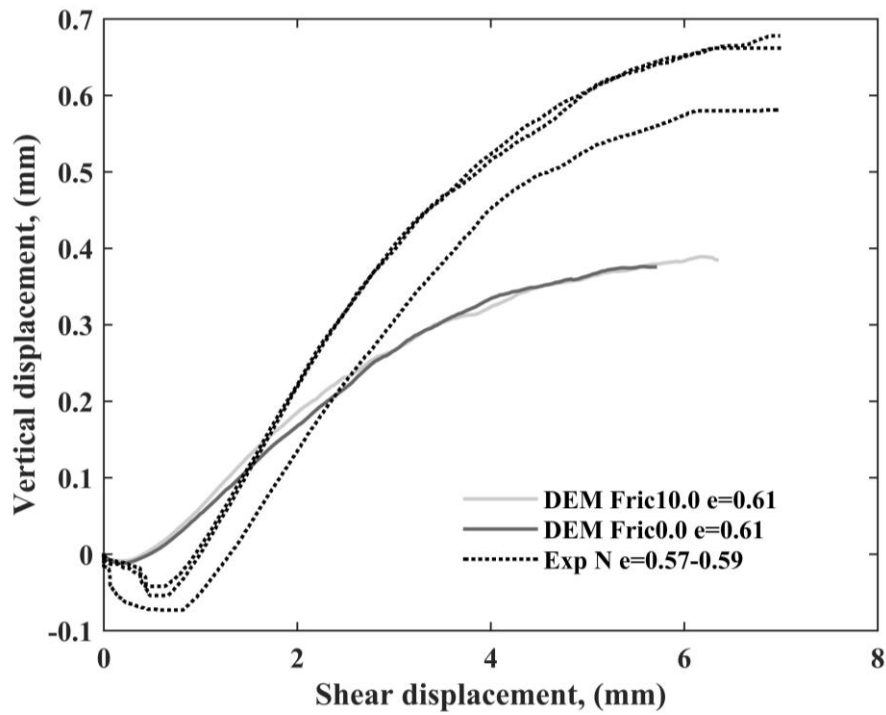
The dilation responses of the DEM specimens were also compared with the experimental specimens as shown in Fig. 4.3(b). It is evident that the vertical displacement response of the DEM specimens and the laboratory specimens are quite different. The experimental specimens exhibit much more initial contraction and much higher dilation rates than the DEM specimens.

An explanation for the difference is not evident at this time, but two options may be possible. Firstly, it may be attributed to the experimental shear box design which exhibits much more contraction at the initial stages of the test and essentially has more compliance than the DEM simulation. Secondly, it may be related to the fact that the top cap is allowed to slightly rotate in the experimental apparatus, but it is not allowed to rotate in the DEM simulations. Preventing the top cap rotation in the experimental apparatus was difficult given the design and there is no consistent way to allow this rotation in the DEM simulations. This will be explored further in the future with a large-scale device at the University of Arkansas capable of allowing or fixing top cap rotation.

The rate of dilation being higher in the experimental tests could also be the difference in the void ratios of the experimental and DEM data. The experimental specimens had a slightly lower void ratio which would result in a higher dilation rate. The lower void ratio should also result in a higher peak stress; however, this was not observed. It is noted here that many other DEM studies have also noted difficulties in matching the stress and dilative responses exactly for various reasons (Dabeet, 2014; Bernhardt et al., 2016). What is an important finding from these macro-scale responses is that it appears that friction on the top and bottom boundaries has virtually no influence on the peak response observed. It also appears that there is a slight delay in strain-softening for the zero friction boundary until particles likely slide and pack together eventually resulting in a similar strain-softening response to the high friction boundary.



(a)



(b)

Fig. 4.3 (a) Shear stress - displacement and (b) vertical displacement of DEM Fric10.0 and DEM Fric0.0

4.3.2 Micro-scale analysis of DEM specimens

Five measurement spheres were specified in the post processing stage in order to investigate the void ratio at different locations in the specimen. Measurement spheres are simply measurement volumes over which quantities such as porosity, stress, and density can be averaged. A plan view of the locations of these spheres (denoted as mpsphere) are as shown in Fig. 4.4.

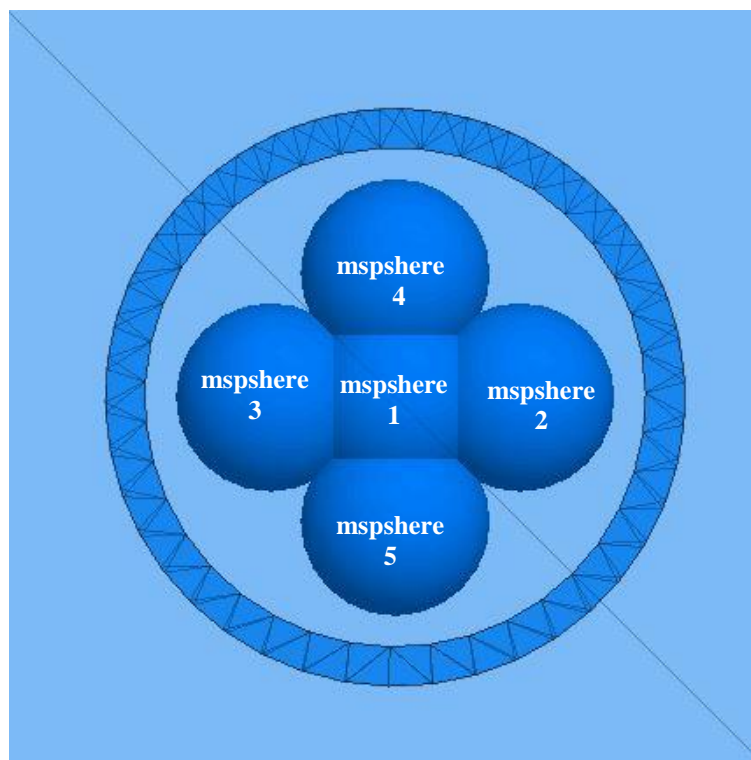


Fig. 4.4 Locations of five measurement spheres

The volumes of particles, including particles completely falling within the spherical boundaries and the internal portion of the spheres for those intersecting the sphere volume boundaries within each measurement sphere were considered for calculating the void ratio. The overall void ratios (calculated according to the specimen boundaries) of DEM Fric10.0 and DEM Fric0.0 are compared with the void ratio of the laboratory specimen along with void ratios from

the measurement spheres at the different locations within the specimens in Fig. 4.5 and Fig. 4.6. The initial overall void ratio of the DEM specimen is 0.6, whereas the void ratios from the five measurement spheres are around 0.56. As shearing progresses, the void ratio increases for the laboratory and DEM specimens as expected. In both DEM specimens, the center of the specimen (msphere1) and msphere4 are very similar and have the lowest void ratio. The rate of change in void ratio is different for DEM Fric0.0 (Fig 4.6); however, this change is very small. For both specimens, the boundary void ratios, or the void ratio calculated from the external specimen boundaries, are higher than the void ratios measured from the measurement spheres. These difference in the void ratios are due to the proximity of the spheres to the flat boundary versus spheres packed near spheres. Within the specimen, spheres interact with spheres and they are packed very tightly. At the boundary however, the spheres and the flat boundaries do not have a tight packing, resulting in the higher void ratio.

The initial contraction and dilation rates of the measurement spheres are more similar to the experimental data than what is observed for the overall boundary void ratio measurement. Therefore, the physical and virtual specimens are very similar in terms of the localized void ratio response, and it is likely that the difference in the overall response may actually be due to the ability of the top cap to rotate. In the future, it would be recommended to install multiple vertical displacement transducers on the experimental top cap to evaluate the significance of the cap rotation and determine whether or not this theory is correct.

The localized dilation response is also very different throughout the specimens. Msphere 3 (on the trailing edge of the specimen) shows the largest dilation in both specimens and msphere 2 (on the leading edge) shows some of the lowest dilation. This further proves previous studies that show non-uniform strains throughout the specimen in direct shear testing.

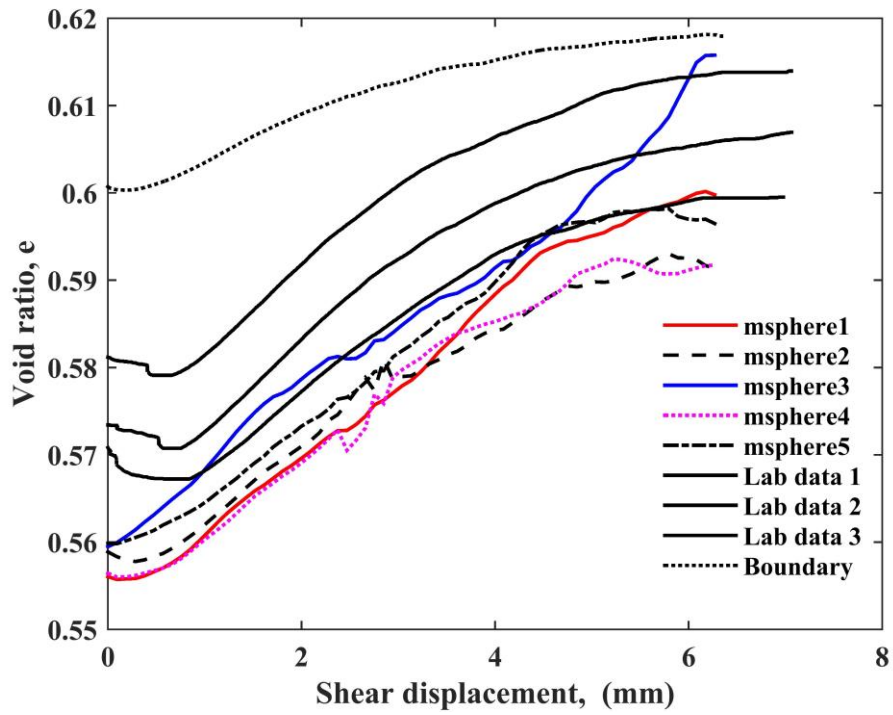


Fig. 4.5 Void ratio of DEM Fric10.0

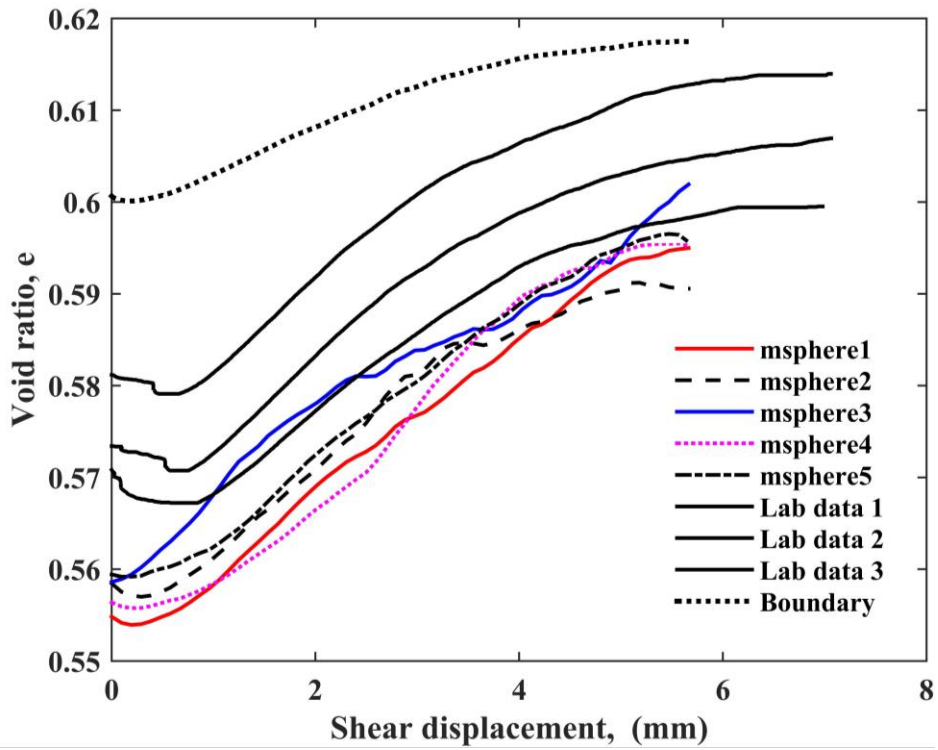


Fig. 4.6 Void ratio of DEM Fric0.0

Incremental displacements as a function of the particle's height in the specimen are given in Fig. 4.7 and 4.8. Masson & Martinez (2001) and Cui & O'Sullivan (2006) previously analyzed a similar response for direct shear DEM specimens. These responses are plotted when the x displacement is approximately 6 mm, after the peak shear stress was reached in both DEM specimens. The response observed is essentially the same regardless of the boundary friction used. In the x-direction (Fig. 4.7(a) and 4.8(a)), the particles in the middle of the specimen, exhibit more movement than particles located near the top and bottom boundaries. The central zone of particles also show a somewhat linear displacement relationship, although there is quite a bit of scatter. One important feature of granular material response is the fact that motion may occur in the y-direction although shearing is progressing in the x-direction (Fig. 4.7(b) and 4.8(b)). Most of this out of plane movement occurs for particles near the central portion of the sample. Also, it can be seen that the particles move up and down vertically (Fig. 4.7(c) and 4.8(c)). Particles located in the upper portion of the specimen move upwards, whereas particles in the lower portion of the specimen move downwards. The vertical displacements of the particles in the shear zone are higher than any other location. This is expected considering that most of the movement of the specimen takes place within the shear zone, compared to the boundaries.

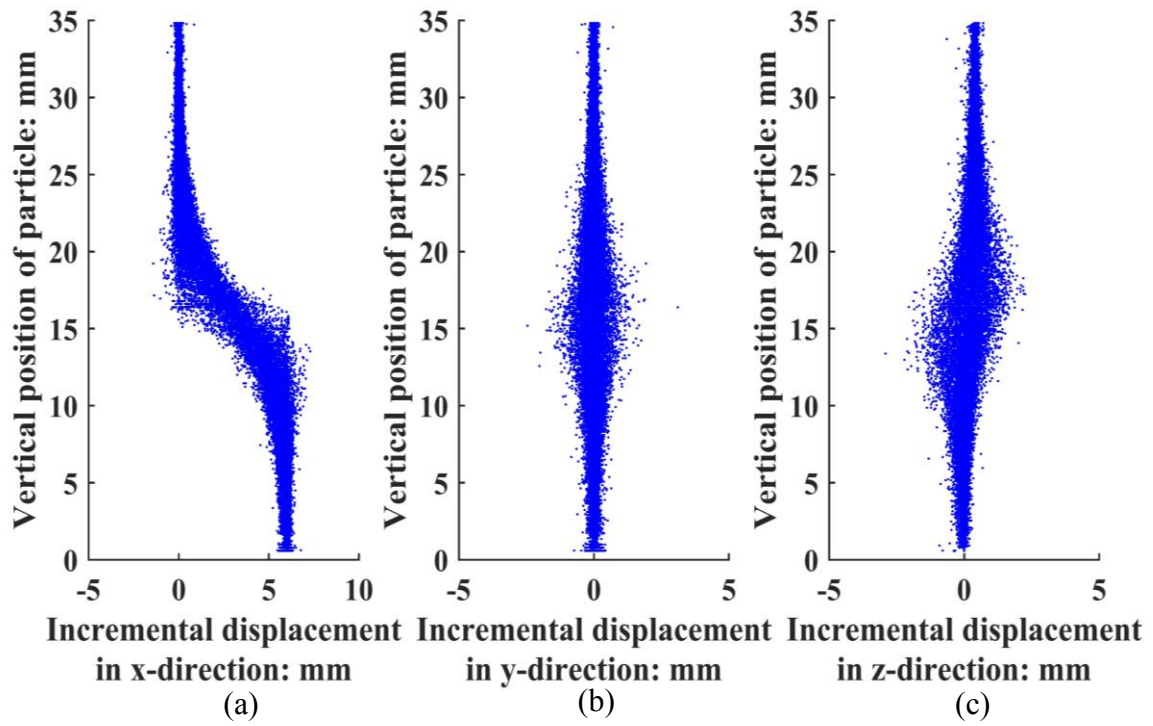


Fig. 4.7 Incremental displacements of particles in DEM Fric10.0

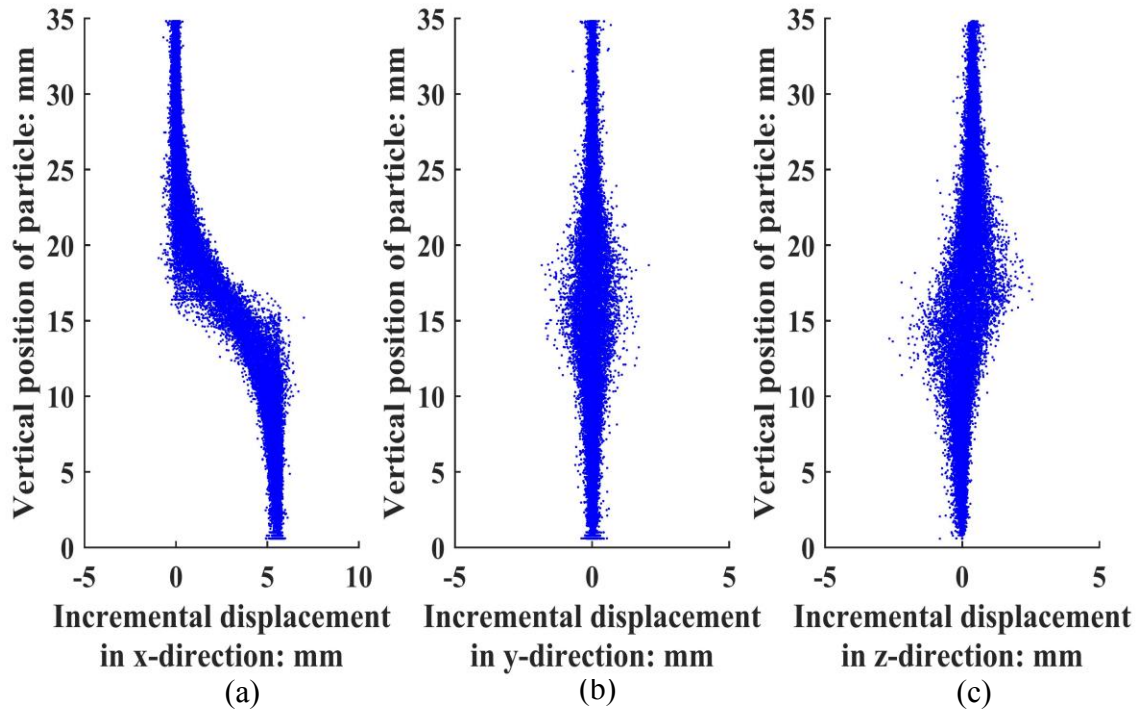


Fig. 4.8 Incremental displacement of particles in DEM Fric0.0

4.3.3 Contact force network

Contact networks which show the force transmission in the specimens are shown in Fig. 4.9 and Fig. 4.10 for the two DEM specimens considered. In this figure, the centers of the contacting particles are connected with lines creating a force network lattice. This represents the particle structural arrangement. For clarity only, forces which are larger than the average contact force are shown. The line thickness is proportional to the magnitude of the contact force. At the beginning of shearing, the lower middle part of both of the specimens have fewer strong force chains, but the DEM Fric10.0 specimen has a large portion of force chains which fall below the average value and thus are not shown. This likely represents some arching occurring in the high friction boundary specimen since particles are not allowed to slide and redistribute the chains easily. It can be seen that at a shear displacement of 6 mm, the upper left corner and bottom right corner of the specimen have very few large force chains and the force chains throughout the central portion of the specimen are aligned diagonally in the direction of shearing. For the high friction and low friction specimens, there were some slight differences in the force network observed. Many more strong force chains (shown by the dark thick lines) were observed in DEM Fric10.0 compared to DEM Fric0.0. Therefore, although the peak stresses were similar for the specimens, the load is transferred through fewer force chains (i.e., particles) when the boundary friction is high. When the boundary friction is low, the force chains collapse easier and the load is carried by many smaller force chains.

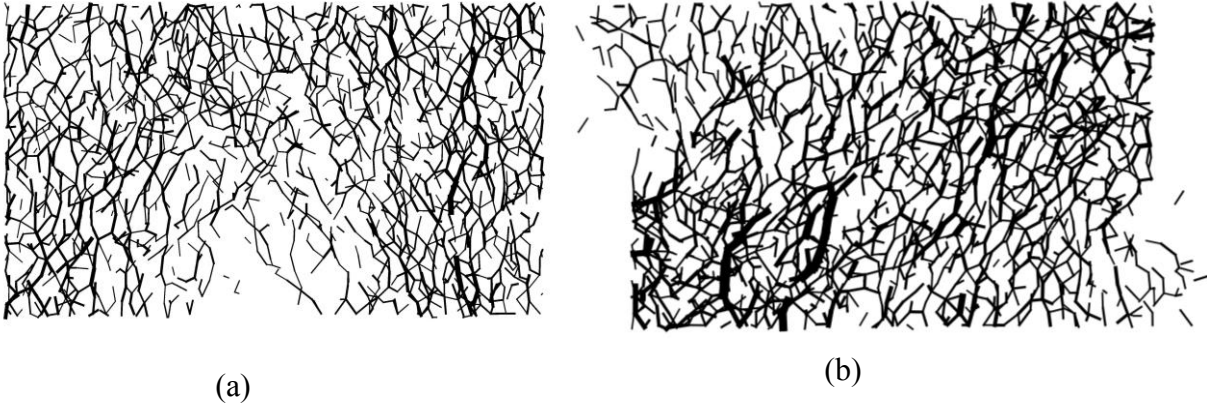


Fig. 4.9 Contact force network of dense DEM Fric10.0 at shearing displacement 0.0 and at shearing distance 6.0mm

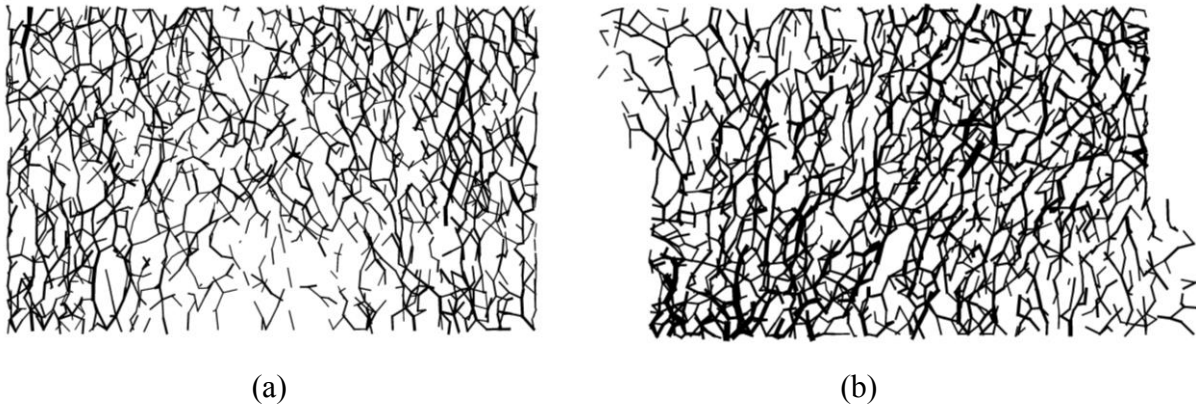


Fig. 4.10 Contact force network of DEM Fric0.0 at shearing displacement 0.0 and at shearing distance 6.0mm

4.4 Conclusions

The DEM results compared well with the experimental data in terms of the overall stress-displacement behavior of the specimens. The initial part of the shearing behavior of the DEM specimens were very close to that of two replicate laboratory specimens and the peak stresses matched quite well. However, the contraction and dilation of the dense specimens were not the same for the DEM and laboratory specimens. Also, the peak stress response of the high friction and low friction boundary specimens did not differ very much. While the strain-softening was delayed for the low boundary friction DEM specimen, it eventually became very similar to that

of the high boundary friction specimen. There was much more strain-softening in the experimental results which agreed with the differences in the dilation response. It is proposed that this could likely be due to the fact that the top cap is allowed to slightly rotate in the experimental apparatus, but no rotation is allowed in the DEM specimens. More testing is needed in the future to confirm this theory.

In terms of the micro-scale response, the localized measurements of void ratios, incremental displacement, incremental displacement vectors and contact force networks for both specimens did not show significant difference in the specimens. Non-uniform localized strains were observed in the measurement sphere void ratio response, and the dilation rates in these localized zones matched quite well with the experimental data. Although it does not appear that a high friction boundary causes any major differences in particle displacements or the peak stress response, it does appear to affect how the load is carried throughout the specimen. DEM Fric10.0 had many more large force chains running diagonally when compared to DEM Fric0.0. As discussed however, this seems to result in similar stress-strain responses and strengths. Ultimately, it is recommended that additional simulations be carried out and further analyses be conducted in the future to investigate the observations further and to examine whether the projection geometries result in any differences in the macro-scale or micro-scale responses. There are several laboratory studies which have stated that the differences due to the projections is minimal, and so it may very well be that the boundary geometry and friction have little effect on the overall response in direct shear tests. This can be understood as the failure is forced through the central plane of the specimen and the rigid boundaries can likely transmit enough shear to cause this failure in densely packed specimens.

CHAPTER 5: CHARACTERIZATION OF ADDITIVE MANUFACTURED PARTICLES FOR DEM VALIDATION STUDIES

5.1 Introduction

Steel ball bearings and glass beads are commonly used as an idealized granular material in laboratory studies, so that the results can be used to calibrate or validate DEM simulations (Cui & O'Sullivan, 2006; Hartl & Ooi, 2008; Roubtsova, Chekired, Morin, & Karray, 2011; Bernhardt, Biscontin, & O'Sullivan, 2016). The selection and characterization of these particles and their inherent properties are important to ensure good agreement between DEM simulations and corresponding experimental tests. One of the limitations for both of these materials is that they are only available in spherical or near spherical form, which does not replicate the actual shape of natural sands. The development in additive manufacturing has enabled to produce any shape of material sent from a desired drawing file to print them. However, the variety of material available along with the methods of printing makes it difficult to choose one material and method. Watters (2017) did a comprehensive study on different types of printers and materials. Based on that study only two materials were selected, and a characterization study is presented here. Cavarretta, et al. (2012) conducted a characterization study for glass beads and steel ball bearings so that a better selection can be made when the Hertz-Mindlin contact model is applied in DEM simulations. Fig. 5.1 shows the difference between the surface features of a steel ball bearing and a gypsum particle. The contact model used in a DEM simulation influences the particle-to-particle interaction and is governed by the material properties. Therefore, it is important to characterize the material before they are used in simulations. This chapter describes the specimen preparation of gypsum and photopolymer particles, their shape and surface characteristics and suitability for using them in DEM models. Further, the Hertzian behavior of the gypsum particle under a small load is evaluated.

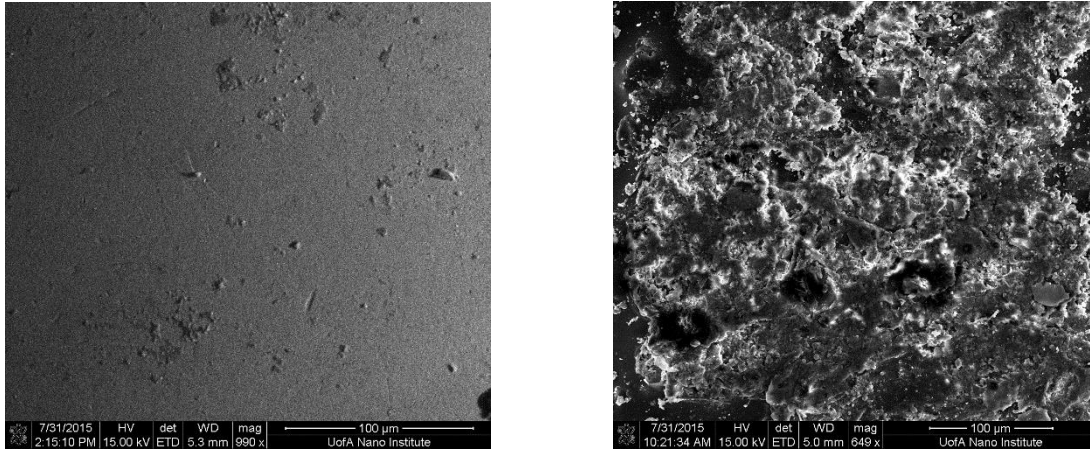


Fig. 5.1 (a) Surface of a steel ball bearing and (b) Surface of a gypsum sphere under scanning electron microscope (SEM) at same magnification power

5.2 Specimen preparation

Two different materials (and corresponding AM technologies) were considered for this study: gypsum powder composite and a photopolymer resin. The models of spheres and cylinders were created using computer-aided-design (CAD) software and .STL files were exported to the AM devices. Spheres were fabricated with diameters of 4 mm, 6 mm, 10 mm, and 12 mm (Fig. 5. 2). Cylinders with dimensions of 10 mm in diameter and 20 mm in length were also fabricated. Although the AM materials can be fabricated in a wide range of sizes and shapes, spheres were used in this study so that they could be directly compared to the commonly used steel ball bearings and glass ballotini.

The first device was a binder-jetting type printer manufactured by 3D Systems Incorporated that uses gypsum powder. The binder-jetting process consists of spreading the gypsum powder across a build plate and then a solution is sprayed in defined locations to bind the powder. This sequence is repeated layer-by-layer to create the 3D object. The gypsum powder is 80-90 % calcium sulfate hemihydrate ($\text{CaSO}_4 \cdot 0.5\text{H}_2\text{O}$) and the binder used to solidify the powder between layers is comprised of 2-pyrrolidone (3Dsystems, 2018). A layer thickness

of 0.1 mm was used for creating the parts at a temperature of 20-22 °C and a relative humidity of 36-40 % to provide optimum print quality (Watters, et al., 2017). After fabrication, a high strength epoxy infiltrant (Strengthmax) was used to infiltrate the gypsum particles to increase the stiffness and overall strength of the particles as recommended by the manufacturer. Additional details of the curing process and factors affecting the strength and homogeneity of the particles are given in Watters and Bernhardt ((Watters and Bernhardt, 2017; Watters and Bernhardt 2018). The second device used was a Form 2® stereolithography (SLA) system manufactured by Formlabs which uses a photopolymer material. The SLA fabrication method uses an ultraviolet light to cure the photopolymer resin layer-by-layer. The parts are then cured in an oven equipped with an LED light with a wavelength between 400-405 nm. Details of the curing procedure can be found in Watters, and Bernhardt (2018).

For both materials, ten spheres of each size were measured manually with a digital caliper and diameters were used to compute sphericity, aspect ratio and circularity. In calculating these parameters, the maximum and minimum measured diameters were selected as d_1 and d_3 , respectively. An intermediate diameter was also determined which was designated as d_2 as described in (Cavarretta, 2009). Aspect ratio, sphericity and circularity were then computed using equations 2.7, 2.8, and 2.9 for the 4mm, 6mm, and 10mm specimens.

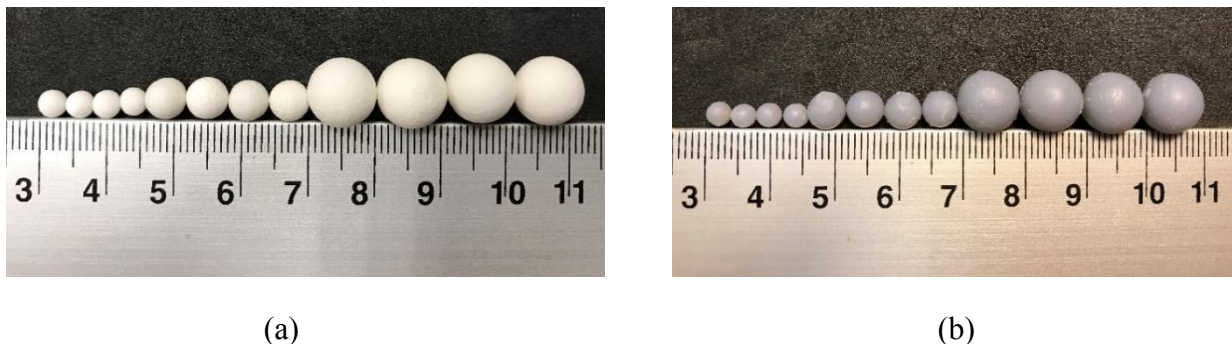


Fig. 5.2 AM printed spheres of 4mm, 6mm and 10mm diameters (a) gypsum and (b) photopolymer

5.3 Determination of Poisson's ratio, surface roughness and hardness

Uniaxial compression tests were conducted on the cylindrical specimens in an Instron machine. In the uniaxial compression machine, the cylindrical specimens were tested with an axial compression rate of 0.04 mm/min. A digital image correlation (DIC) camera setup was used to measure the longitudinal strain and lateral strain to calculate Poisson's ratio. The principle of DIC is based on a set of digital photographs of a specimen taken at different times during testing to measure strain and displacement. Vic 3D software (correlatedsolutions.com, 2010) was used to measure the longitudinal strain and lateral strain on a speckled pattern located in the center of the cylindrical specimen (Fig. 5.3). The pattern was placed in the center of the specimen in order to eliminate boundary effects.

Uniaxial compression testing was also conducted on the gypsum spheres at a rate of 1 $\mu\text{m/s}$ with a compressive force less than 100 N, which was the maximum load limit for the load cell used (Fig. 5.4). Furthermore, loads less than 100 N were used on the spherical specimens in order to remain within the elastic regime of the material. This device was custom made for the compression of natural and artificial particles. The DIC system was not used for this configuration.

A Fogale Nanotech optical interferometer (Fogale Nanotech Microsurf 3D) and a confocal microscope (Zeiss LSM 700) were used to determine the surface roughness of the spherical particles. Interferometer works on the principle where one beam initiating from a light source is divided into two which are reflected by a reference mirror and the rough surface under consideration. Following that, these beams are captured by a charge coupled device (CCD) camera and are analyzed with a resolution of 10 nanometers. Both R_a and RMS were determined

to assess the overall surface roughness of the particles, whereas the RMS_f was determined for evaluating the Hertzian behavior of the spherical particles under small loads.

A confocal microscope was used as an additional method for measuring the surface roughness to provide a comparison to the values of surface roughness obtained using the interferometer. Unlike the interferometer which uses the principle of light reflection, the confocal microscope uses a laser to scan a surface using a slicing method in which each slice is used to create a composite surface roughness.

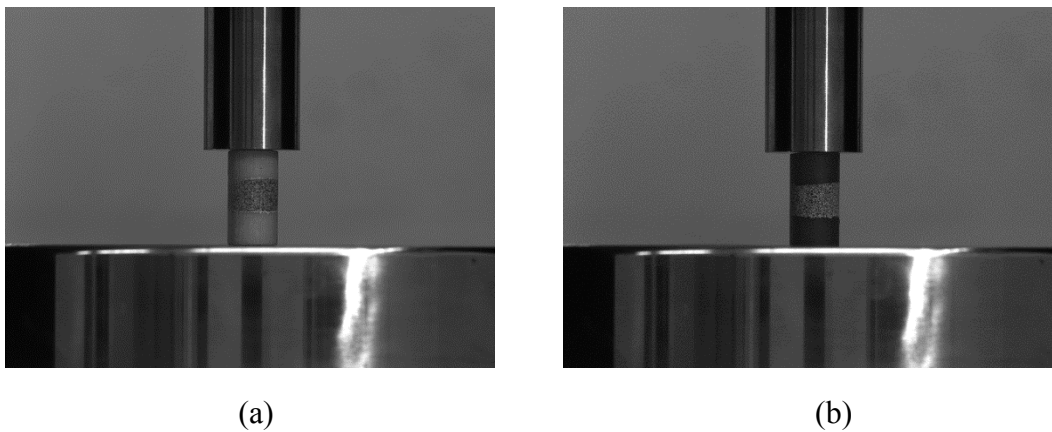


Fig. 5.3 Compression testing on a 10mm diameter cylinder: (a) gypsum (b) photopolymer

Inter-particle friction angles were also determined for the gypsum and photopolymer spheres of diameters 4mm, 6mm, and 10mm using the apparatus introduced (Cavarretta, et al., 2011). The specimens were sheared with a vertical load of 0.93 N at a speed of 2.4 mm/hour in the friction apparatus. No rotation of the particle is allowed and movement along the z-axis is permitted, thus the top particle must slide up and over the bottom particle which remains stationary (Fig. 5.5). Using attached load cells, the horizontal force is measured, which is processed to ultimately calculate the inter-particle friction of the particles (Cavarretta, et al., 2011).



Fig. 5.4 Uniaxial compression testing machine

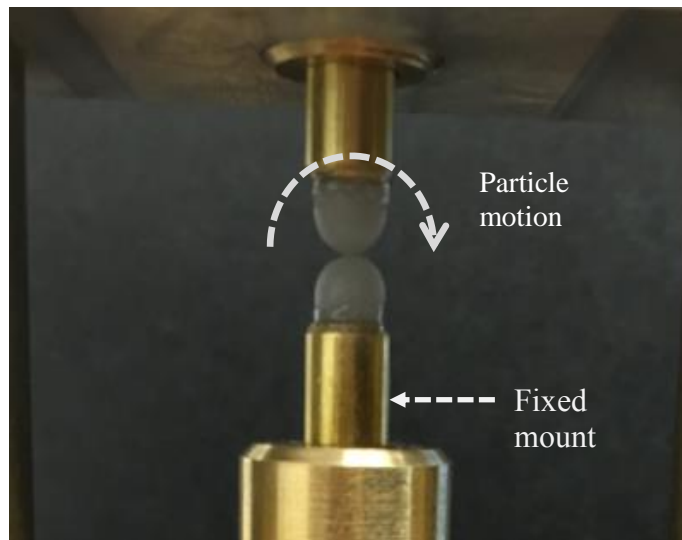


Fig. 5.5 Inter-particle friction testing on 4mm diameter photopolymer spheres

For the Rockwell hardness tests, 12 mm cuboidal gypsum specimens and 12 mm diameter gypsum spheres were tested. The Rockwell hardness (Fig. 5.6) test has an indenter with a diameter of 6.35 mm for which a load of 588.4 N (60 kgf) is applied to the specimen. Initially, a load of 98 N (10 kgf) is applied as a seating load, after which the load application is completed, a hardness value is directly obtained from the machine. Hardness is the mean contact stress p when the initial plastic deformation in the area of contact occurs (Cavarretta, et al., 2012). The value of p is determined as suggested by Tabor (1970) as the ratio between the max

indentation load and the projected area of contact, which is a geometric function of the Rockwell depth of indentation expressed in micrometers: $100-y_p$, where $100\ \mu\text{m}$ is the reference depth in the Rockwell test and y_p is the distance between the deepest point of the indented surface and the reference plane, given as HR15Y output in the apparatus. Hardness testing values were compared with the hardness values obtained from the curve fitting exercise carried out using the results of uniaxial compression testing and assuming a Hertzian behavior.

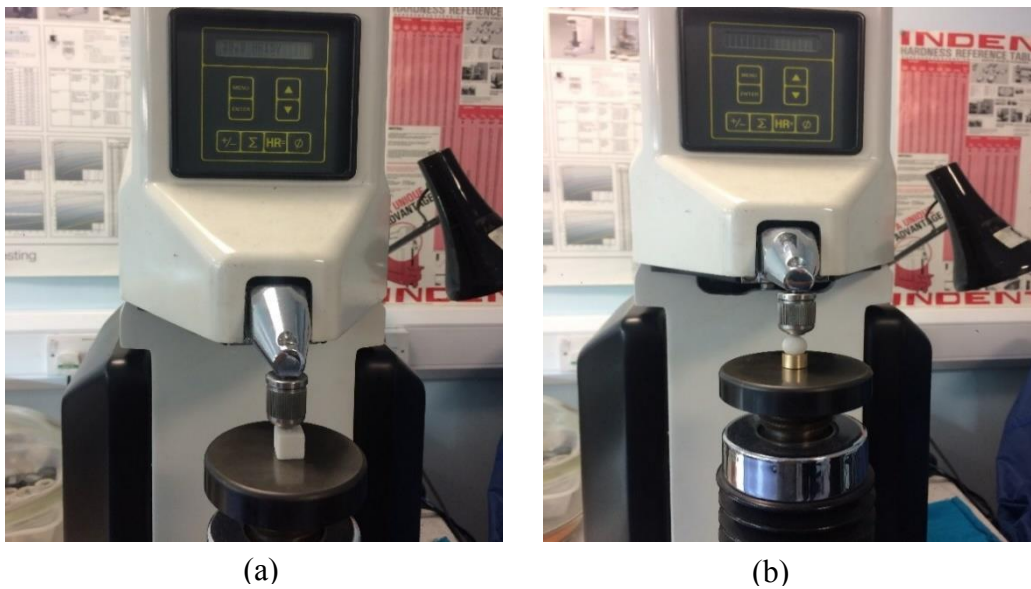


Fig. 5.6 Rockwell testing on: (a) gypsum cube; (b) gypsum sphere

5.4 Results and discussion

5.4.1 Shape parameters

The shape parameters for the gypsum and photopolymer spheres calculated from the measured diameters are given in Table 5.1. As the measured diameters indicates, the fabricated gypsum particles were slightly larger than the specified diameter whereas the photopolymer spheres were slightly smaller than the input dimension due to the printing tolerances of the two AM devices. The minimum diameter, d_{min} and maximum diameter, d_{max} are selected from the

four measured diameters for calculating the shape parameters. The average value of d_{min} for the 4 mm gypsum spheres was 1.8 % larger than the specified diameter whereas the average d_{max} was larger by 8.5 %. On the other hand, the average d_{min} value of the 4mm photopolymer spheres showed a deviation of 8 % from the specified diameter and d_{max} showed only a 1 % deviation. The 6 mm and 8 mm particles showed a lower deviation from the specified value. Interestingly, the d_{max} values of photopolymer spheres never exceeded the specified diameter of the model.

Sphericity and circularity of the spheres for both materials have an ideal value of 1 whereas the aspect ratio of the gypsum spheres was slightly higher than photopolymer spheres. However, these values were not drastically different, which demonstrates that the photopolymer spheres are as good as gypsum spheres in terms of their spherical shape factors. One of the reasons for the larger deviation in aspect ratio values of the photopolymer spheres could be due to the requirement of the build support during fabrication which is not required for the gypsum material. Overall, the shape parameters assessed in this study indicate that the gypsum and photopolymer manufactured particles can be considered for experimental validation tests where spherical particles are used in the DEM simulations.

Table 5.1 Shape parameters for AM spheres

Material type	Nominal diameter	Measured diameter		No. of particles tested	Sphericity	Aspect ratio	
		d_{min} (mm)	d_{max} (mm)			ratio	Circularity
Gypsum	4	4.07	4.34	10	1.000	0.979	1.000
Gypsum	6	6.03	6.37	10	1.000	0.984	1.000
Gypsum	10	10.03	10.36	10	1.000	0.986	1.000
Photopolymer	4	3.68	3.96	10	1.000	0.961	1.000
Photopolymer	6	5.65	5.99	10	1.000	0.967	1.000
Photopolymer	10	9.64	9.97	10	1.000	0.980	1.000

5.4.2 Surface characteristics

Surface roughness measurements of 4 mm, 6 mm, and 10 mm gypsum and photopolymer spheres were conducted using a confocal microscope and an interferometer before they were used in shearing in the friction apparatus. The surface roughness measurements provided in Table 5.2 and Table 5.3 were obtained over an area of 50 μm x 50 μm . Four specimens of each size were tested for the two materials. Overall, the roughness values obtained for the gypsum spheres using both measurement techniques were comparatively higher than the values of roughness obtained for the photopolymer specimens. It shall be noted that the interferometer consistently measured higher surface roughness values as compared to the confocal microscope for the gypsum material. For the photopolymer material, however, the values obtained by interferometry were lower than the values obtained using the confocal microscope (Table 5.3). This difference could be due to the level of light reflectivity associated with the interferometer based on material type and its relative albedo.

Table 5.2 Inter-particle friction and surface roughness values of gypsum spheres.

Nominal Diameter	Inter-particle friction	Confocal		Interferometer					
		R_a	R_{af} (flattened)	RMS	RMS_f	R_a	R_{af} (flattened)	RMS	RMS_f
(mm)	(deg)	(μm)	(μm)	(μm)	(μm)	(μm)	(μm)	(μm)	(μm)
4	27.5	1.710	0.995	2.113	1.328	2.122	0.516	2.546	0.866
6	24.7	2.130	1.117	2.553	1.479	2.296	0.437	2.995	0.784
10	26.6	0.943	1.493	1.771	1.257	2.945	0.519	3.302	0.863

Table 5.3 Inter-particle friction and surface roughness values for photopolymer spheres before shearing.

Nominal Diameter	Inter-particle friction	Confocal			Interferometer				
		R_a	R_{af} (flattened)	RMS	RMS_f	R_a	R_{af} (flattened)	RMS	RMS_f
(mm)	(deg)	(μm)	(μm)	(μm)	(μm)	(μm)	(μm)	(μm)	(μm)
4	11.2	1.480	0.870	1.816	1.115	1.281	0.194	1.556	0.327
6	16.7	1.883	0.778	2.231	0.992	1.012	0.115	1.078	0.182
10	14.3	0.731	1.284	1.575	0.900	1.194	0.244	1.548	0.388

In general, the gypsum spheres tend to demonstrate higher roughness than the photopolymer spheres; however, these values are on the order of micrometers and indicate no considerable variation. Therefore, it can be said that both AM materials are likely suitable in terms of surface roughness. The flattened surface roughness (RMS_f) obtained for the gypsum spheres was used in the curve fitting exercise of Hertzian curves for back-calculating the Young's Modulus value and the hardness of the material which will be discussed below.

Results for inter-particle friction tests for the gypsum and photopolymer spheres are illustrated in Fig. 5.7 and Fig. 5.8, respectively. The average values of inter-particle friction were 26.3 ° and 14.1 ° for the gypsum and photopolymer specimen, respectively. The value of relative humidity fluctuated from 51.7 % to 53.8 % during the inter-particle friction tests of gypsum particles. The friction value for gypsum begins with a higher value of 34 ° and ends around 22 °. It is possible that this fluctuation is caused by the change in relative humidity during the experiment or possibly the effects of some plastic deformation at the particle contact surface during shearing. Shape and surface parameters also could be an influencing factor in the inter-particle friction testing, and these factors could be responsible for the variation of inter-particle friction values between these three different sizes of specimens.

Figs 5.9-5.12 show the scanning surface of particles tested and the roughness profiles before and after testing in the inter-particle shearing apparatus. Although roughness values vary within a small interval, there is no clear relationship between them and the values of inter-particle friction presented here. The speed of shearing, humidity and diameter of the particles also might have influenced the surface roughness parameters obtained.

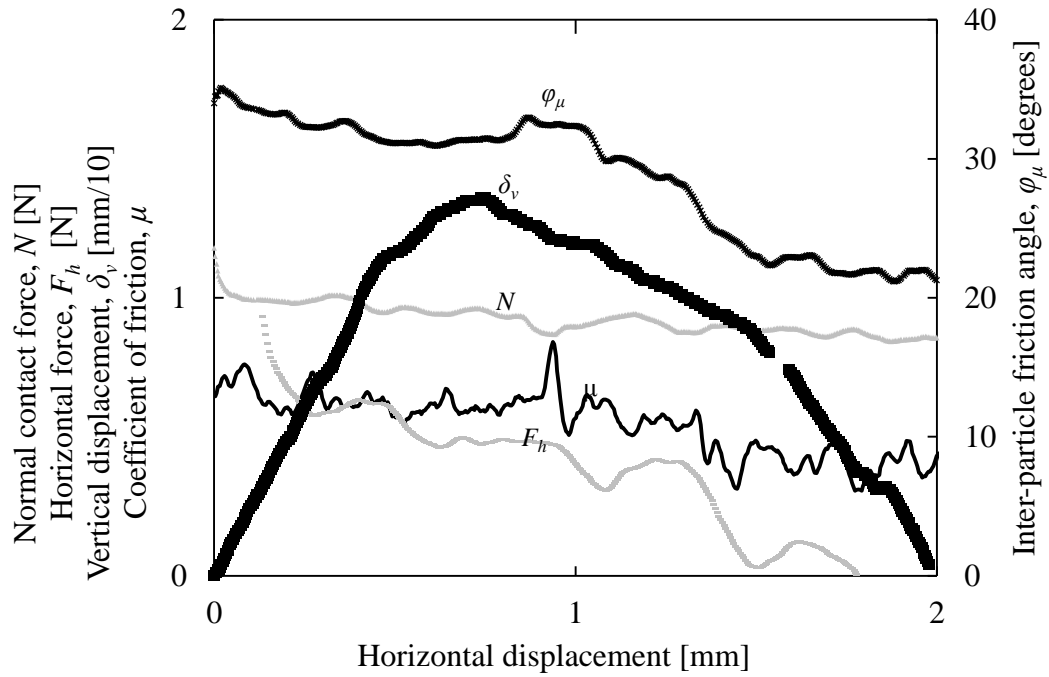


Fig. 5.7 Inter-particle friction test of 4mm gypsum sphere

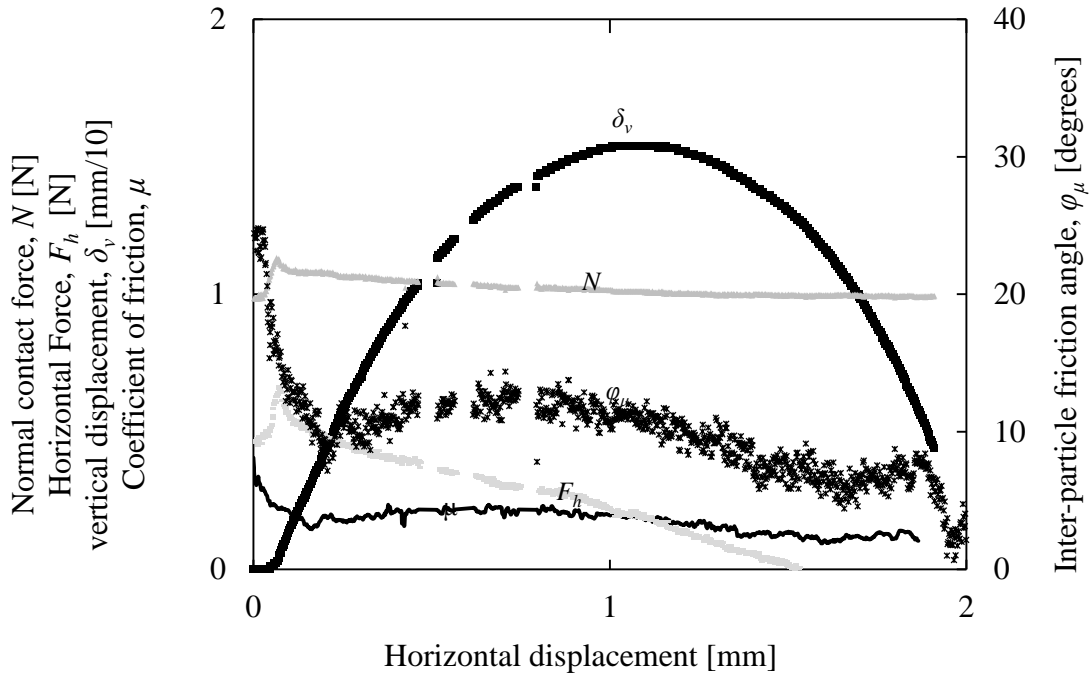


Fig. 5.8 Inter-particle friction test of 4 mm photopolymer sphere

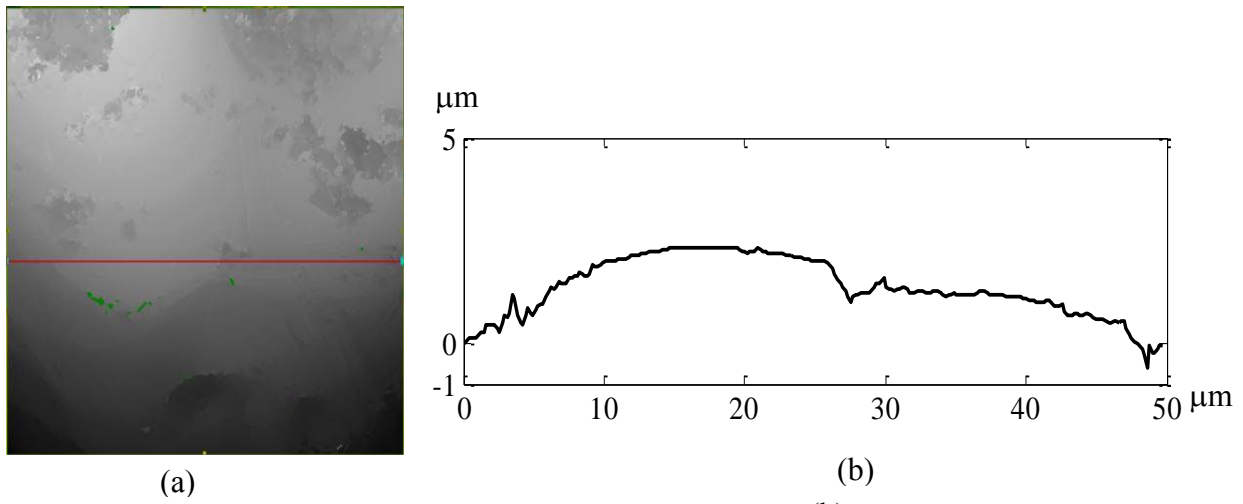
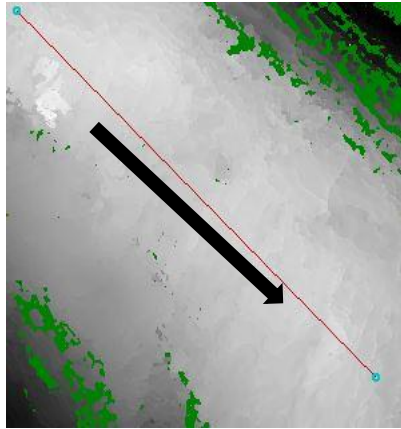
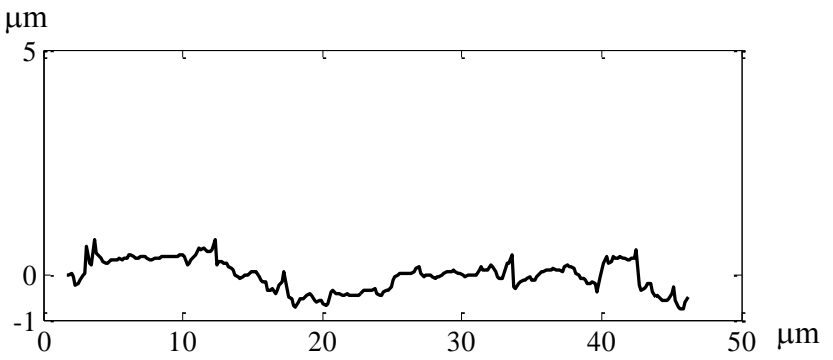


Fig. 5.9 Interferometric view of 10 mm gypsum sphere (a) surface (b) profile before shearing

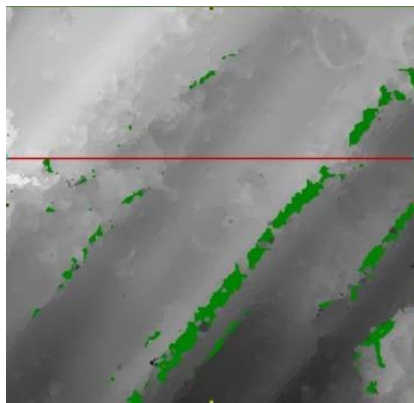


(a)

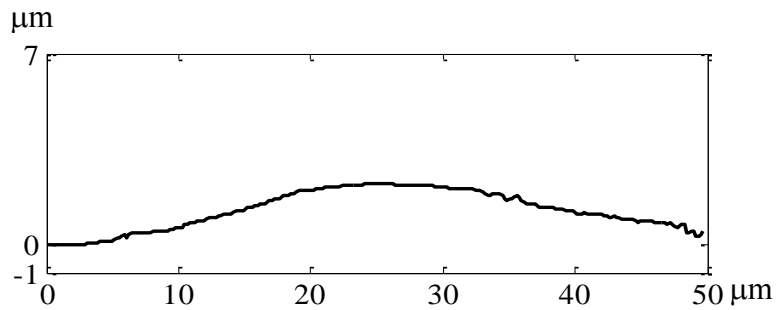


(b)

Fig. 5.10 Interferometric view of 10 mm gypsum sphere (a) surface (arrow represents direction of shearing) (b) roughness profile after shearing



(a)



(b)

Fig. 5.11 Interferometric view of 10 mm photopolymer sphere (a) surface (b) roughness profile before shearing

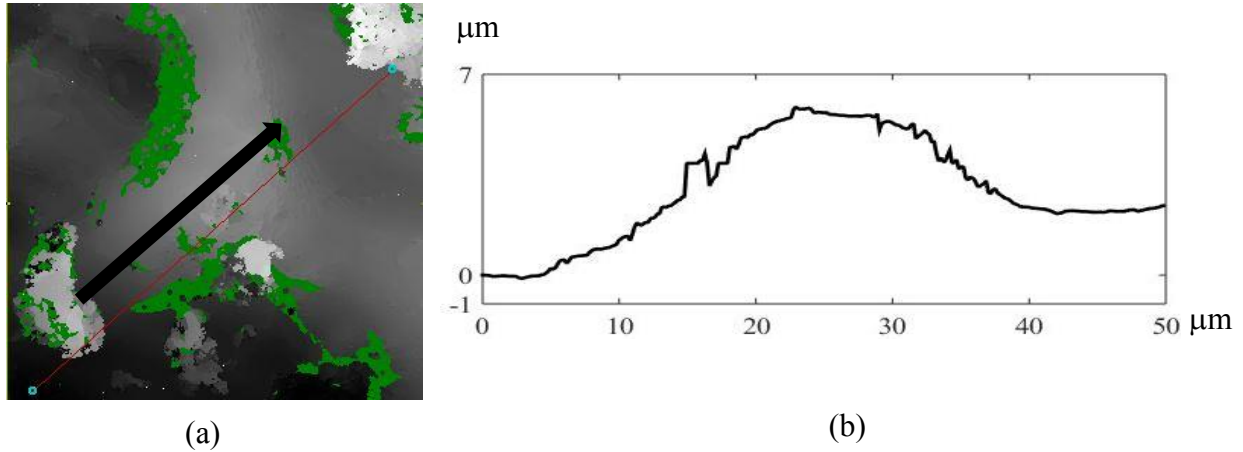


Fig. 5.12 Interferometric view of 10 mm photopolymer sphere (a) surface (b) profile after shearing

5.4.3 Material properties

The density for the gypsum and photopolymer are 1.6 g/cm^3 and 1.2 g/cm^3 , respectively as previously determined by Watters, et al., 2017. The plots of longitudinal and lateral strains during uniaxial compression are displayed in Fig. 5.13 and Fig. 5.14 from which the Poisson's ratio was found to be 0.27 and 0.39 for the gypsum and photopolymer specimens, respectively. Plachy, et al., (2011) determined the Poisson's ratio of various specimens of gypsum materials with different water/gypsum ratios and reported values between 0.25 – 0.35. Therefore, the values obtained in this experiment are consistent with previously published values within a range of 0.25-0.33.

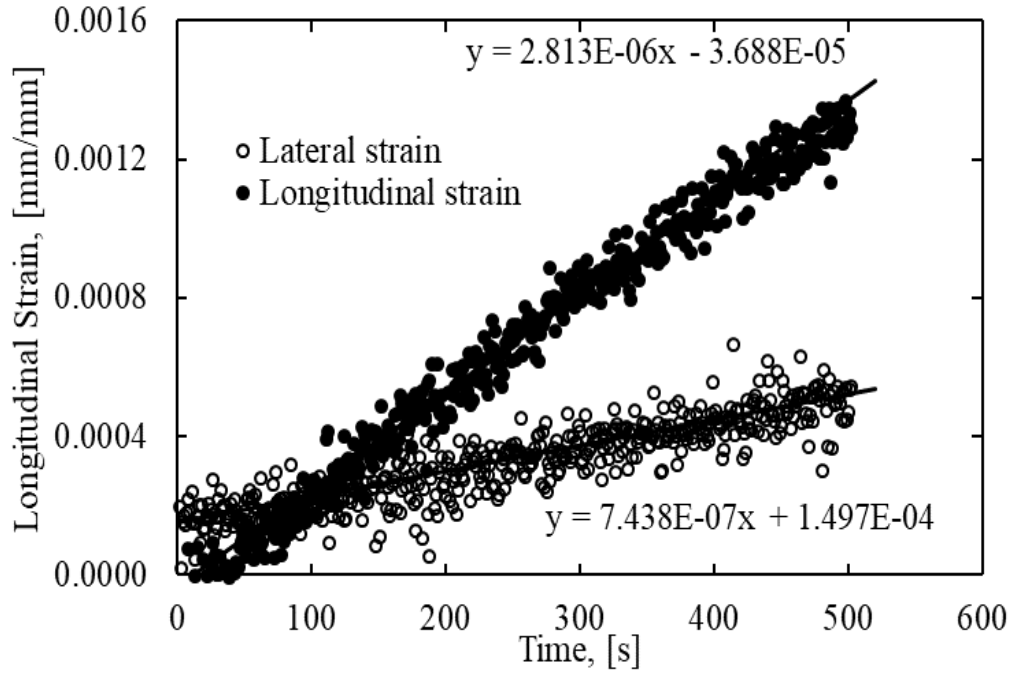


Fig. 5.13 DIC calculated strain from 10 mm diameter gypsum cylinder in uniaxial compression

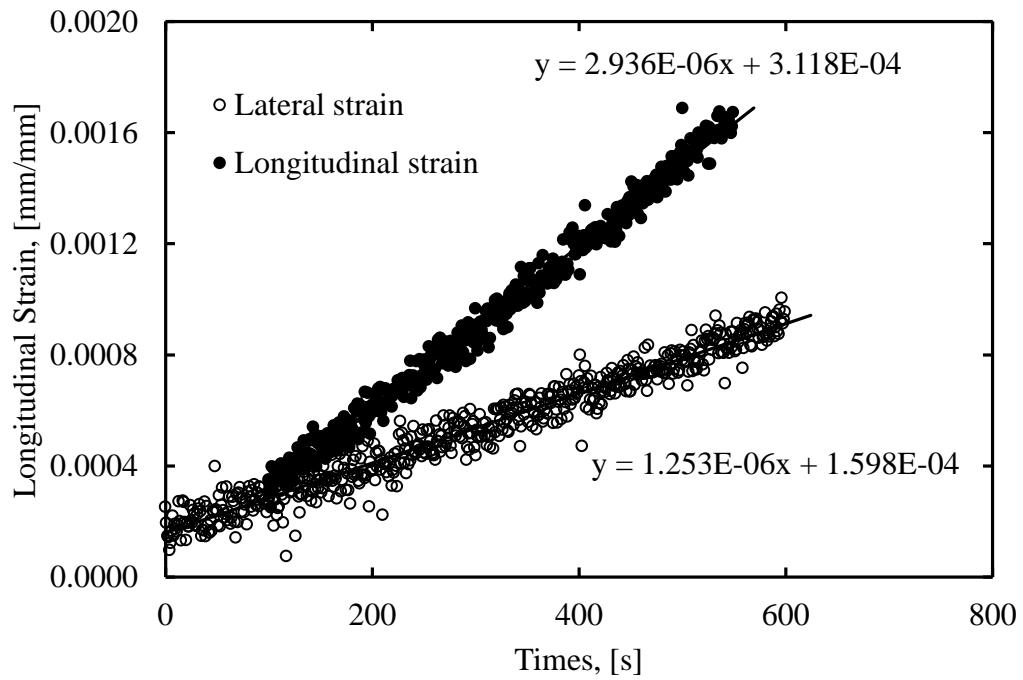


Fig. 5.14 DIC calculated strain from 10 mm diameter photopolymer cylinder in uniaxial compression

Load-displacement curves were obtained from uniaxial compression tests on the 12 mm diameter spheres. Fig. 5.15 presents a specimen of the results along with a Hertzian curve in which a Young's modulus value, E_1 for the steel platen was assumed to be 200,000 MPa and the Poisson's ratio, ν_1 , was 0.27. In Fig. 15, $\delta = \delta_{pm}$, which is the intercept of the curve on the horizontal axis representing the plastic deformation, δ_{pm} . Measured plastic deformation δ_{pm} was obtained from the plot, and used in computing the hardness value (or mean Hertzian contact pressure) defined as

$$\delta_{pm} = R \left(\frac{3\pi H}{4E} \right)^2 \quad (2.13)$$

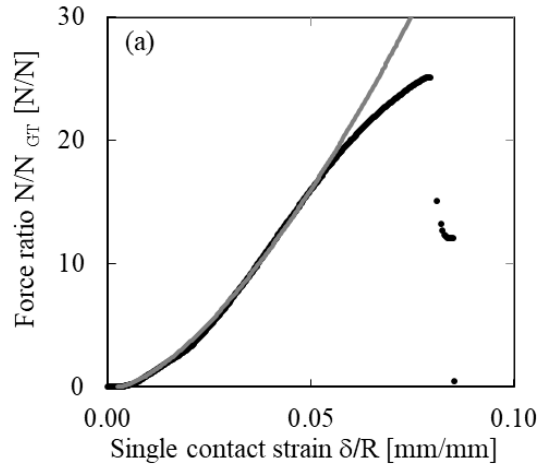
where H is the hardness. The value of Young's modulus was back calculated from the Hertz-Mindlin curve fitting exercise, as discussed in Cavarretta, et al. (2012) on borosilicate glass ballotini.

Equation 2.12 was used in these calculations along with the values of RMS_f determined during the surface roughness measurements. When two particles are compressed against each other, the Hertzian response occurs only within the elastic regime. From Fig. 5.15, the Hertzian threshold occurs at $N = N_{GT}$, which shows the behavior complies with the Greenwood Tripp model of monotonic loading of a rough non-conforming contact. Therefore, according to the GT model, the contacts can be considered as smooth, since they have already experienced elastic deformation of the surface asperities during the initial loading.

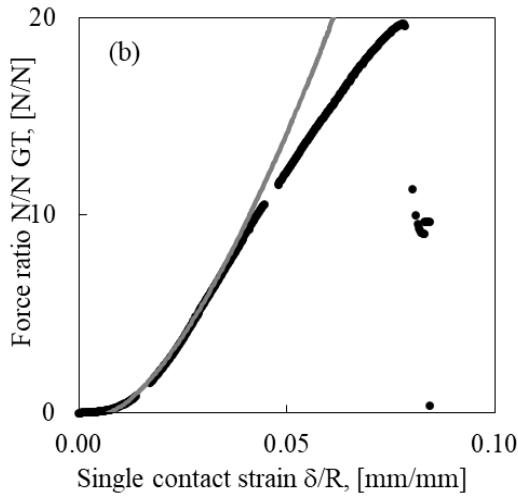
For ten specimen spheres, the Hertzian curve was fitted for the values of $N > N_{GT}$ and the Young's modulus values were determined for the material. The average value of Young's modulus obtained from these fitting exercises was 2900 MPa, which is lower than the Young's modulus value determined for the alkaline ballotini as reported by Cavarretta, et al. (2012). It is to be noted that none of the gypsum spheres tested under uniaxial compression in this study had

a deviation from the GT theory. This shows that these materials are a good candidate for experimental validation studies involving the Hertz-Mindlin contact model.

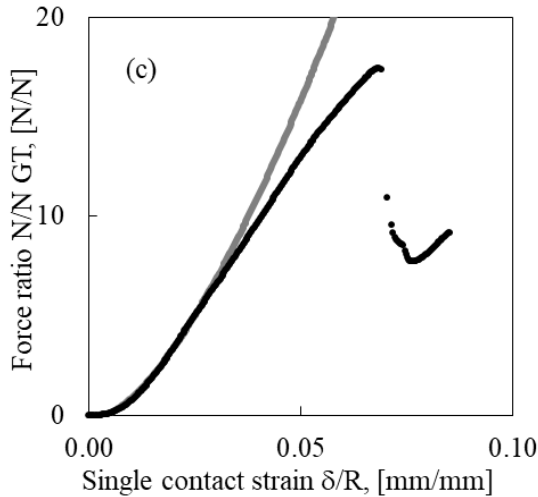
A summary of the crushing load, Young's moduli values for the material, and hardness from the compression tests are presented in Table 5. 4. Overall, the mobilized force for each of these specimens was slightly different, ranging from 3500-3300 MPa. The lowest values for E observed were 2400 MPa. The H values determined for these specimens also showed similar trend, with an average value of 80 MPa. H values were also back-calculated considering the plastic displacement δ_p . Initial plastic displacement obtained ranged from 0.01 – 0.03, with an average of 0.02 mm. The values of δ_p obtained from the curve fitting are closer to the values of δ_p for borosilicate glass ballotini from (Cavarretta, et al., 2012). Current study obtained δ_{pm} and δ_p are equal, hence denoted as δp in the data besides the Fig.s 5.15 (a)-(j). The H values obtained from the curve fitting exercise is compared with the H values determined using Rockwell hardness tests as shown in Table 5. While some variance is observed for the back-calculated Young's modulus values, it is likely that this difference is due to the AM fabrication method in which exact replication may not be as easy as with the fabrication of steel ball bearings or glass ballotini.



Size	d	11.98	mm
Flattened roughness	RMS_f	0.002	mm
Surface Hardness	H	55	MPa
Poisson ratio	ν_2	0.27	
Young's modulus	E	2400	MPa
Plastic displacement	δ_p	0.015	mm
Hertzian constant		8346	MPa(mm ^{-0.5})
Equivalent Young's modulus	E^*	2558	MPa
Relative radius	R	5.99	mm
Hertzian threshold	N_{GT}	79.18	N
Plastic displacement predicted	δ_p	0.015	mm
Crushing load	N_{max}	1988	N

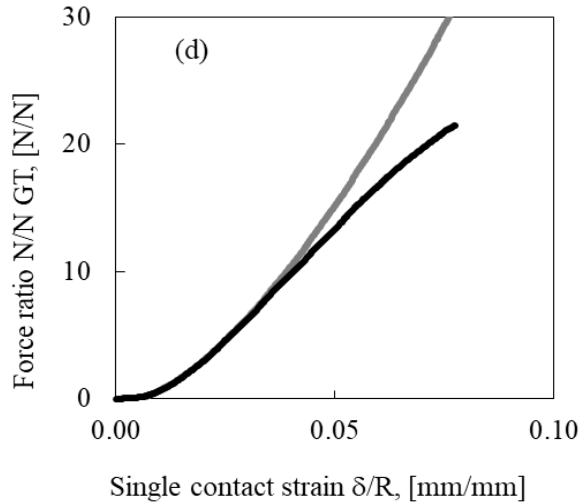


Size	d	12.09	mm
Flattened roughness	RMS_f	0.002	mm
Surface Hardness	H	110	MPa
Poisson ratio	ν_2	0.27	
Young's modulus	E	3000	MPa
Plastic displacement	δ_p	0.040	mm
Hertzian constant		10449	MPa(mm ^{-0.5})
Equivalent Young's modulus	E^*	3188	MPa
Relative radius	R	6.045	mm
Hertzian threshold	N_{GT}	99.13	N
Plastic displacement predicted	δ_p	0.040	mm
Crushing load	N_{max}	1951	N

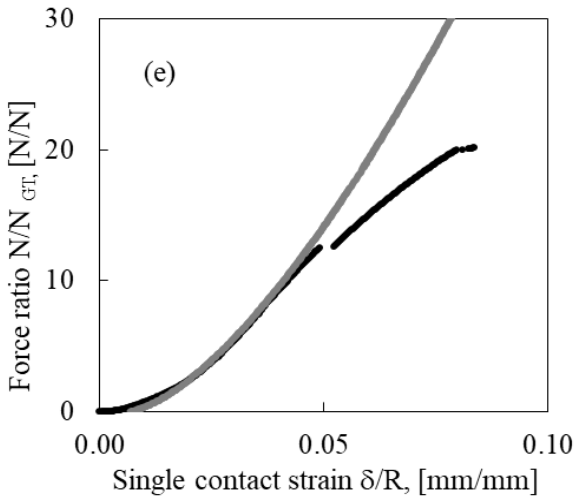


Size	d	12.11	mm
Flattened roughness	RMS_f	0.002	mm
Surface Hardness	H	85	MPa
Poisson ratio	ν_2	0.27	
Young's modulus	E	3300	MPa
Plastic displacement	δ_p	0.020	mm
Hertzian constant		11487	MPa(mm ^{-0.5})
Equivalent Young's modulus	E^*	3501	MPa
Relative radius	R	6.055	mm
Hertzian threshold	N_{GT}	108.97	N
Plastic displacement predicted	δ_p	0.020	mm
Crushing load	N_{max}	1900	N

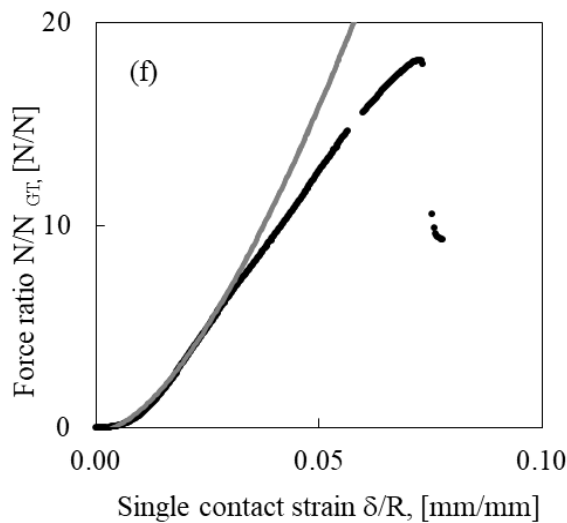
Fig. 5.15 (a)-(j) Uniaxial compression test on gypsum spheres (Contd.)



Size	d	12.11 mm
Flattened roughness	RMS_f	0.002 mm
Surface Hardness	H	89 MPa
Poisson ratio	ν_2	0.27
Young's modulus	E	2900 MPa
Plastic displacement	δ_p	0.028 mm
Hertzian constant		10115 MPa(mm ^{-0.5})
Equivalent Young's modulus	E^*	3083 MPa
Relative radius	R	6.055 mm
Hertzian threshold	N_{GT}	95.95 N
Plastic displacement predicted	δ_p	0.028 mm
Crushing load	N_{max}	2068 N

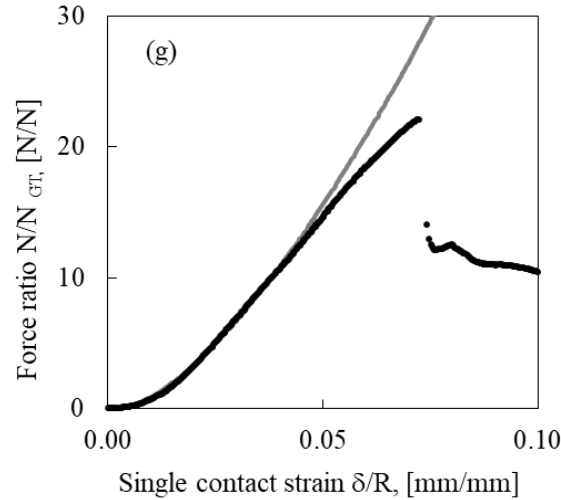


Size	d	12.08 mm
Flattened roughness	RMS_f	0.002 mm
Surface Hardness	H	103 MPa
Poisson ratio	ν_2	0.27
Young's modulus	E	2800 MPa
Plastic displacement	δ_p	0.040 mm
Hertzian constant		9759 MPa(mm ^{-0.5})
Equivalent Young's modulus	E^*	2978 MPa
Relative radius	R	6.04 mm
Hertzian threshold	N_{GT}	92.58 N
Plastic displacement predicted	δ_p	0.040 mm
Crushing load	N_{max}	1840 N

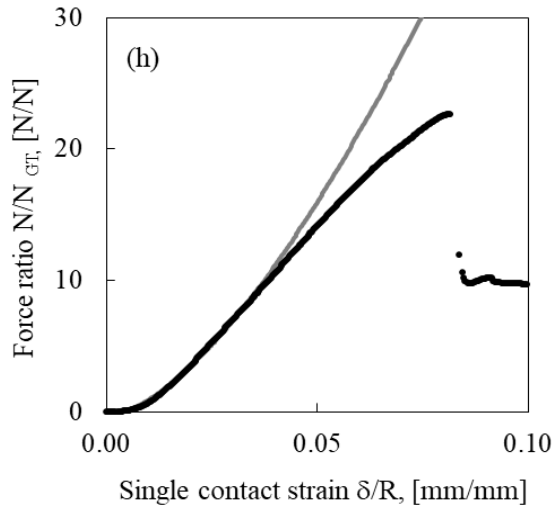


Size	d	12.13 mm
Flattened roughness	RMS_f	0.002 mm
Surface Hardness	H	82 MPa
Poisson ratio	ν_2	0.27
Young's modulus	E	3200 MPa
Plastic displacement	δ_p	0.020 mm
Hertzian constant		11153 MPa(mm ^{-0.5})
Equivalent Young's modulus	E^*	3397 MPa
Relative radius	R	6.065 mm
Hertzian threshold	N_{GT}	105.81 N
Plastic displacement predicted	δ_p	0.020 mm
Crushing load	N_{max}	1924 N

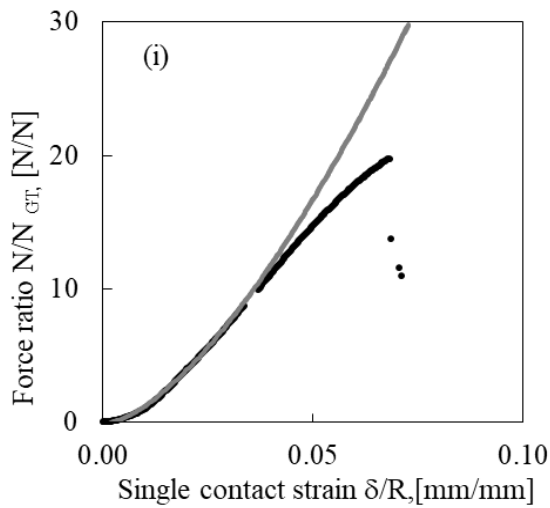
Fig. 5.16 (a)-(j) Uniaxial compression test on gypsum spheres (Contd.)



Size	d	11.98 mm
Flattened roughness	RMS_f	0.002 mm
Surface Hardness	H	65 MPa
Poisson ratio	ν_2	0.27
Young's modulus	E	2500 MPa
Plastic displacement	δ_p	0.020 mm
Hertzian constant		8690 MPa(mm ^{-0.5})
Equivalent Young's modulus	E^*	2663 MPa
Relative radius	R	5.99 mm
Hertzian threshold	N_{GT}	82.44 N
Plastic displacement predicted	δ_p	0.020 mm
Crushing load	N_{max}	1194 N



Size	d	12.09 mm
Flattened roughness	RMS_f	0.002 mm
Surface Hardness	H	64 MPa
Poisson ratio	ν_2	0.27
Young's modulus	E	2600 MPa
Plastic displacement	δ_p	0.018 mm
Hertzian constant		9074 MPa(mm ^{-0.5})
Equivalent Young's modulus	E^*	2768 MPa
Relative radius	R	6.045 mm
Hertzian threshold	N_{GT}	86.09 N
Plastic displacement predicted	δ_p	0.018 mm
Crushing load	N_{max}	1953 N



Size	d	12.12 mm
Flattened roughness	RMS_f	0.002 mm
Surface Hardness	H	52 MPa
Poisson ratio	ν_2	0.27
Young's modulus	E	2800 MPa
Plastic displacement	δ_p	0.010 mm
Hertzian constant		9775 MPa(mm ^{-0.5})
Equivalent Young's modulus	E^*	2978 MPa
Relative radius	R	6.06 mm
Hertzian threshold	N_{GT}	92.73 N
Plastic displacement predicted	δ_p	0.010 mm
Crushing load	N_{max}	1833 N

Fig. 5.17 (a)-(j) Uniaxial compression test on gypsum spheres (Contd.)

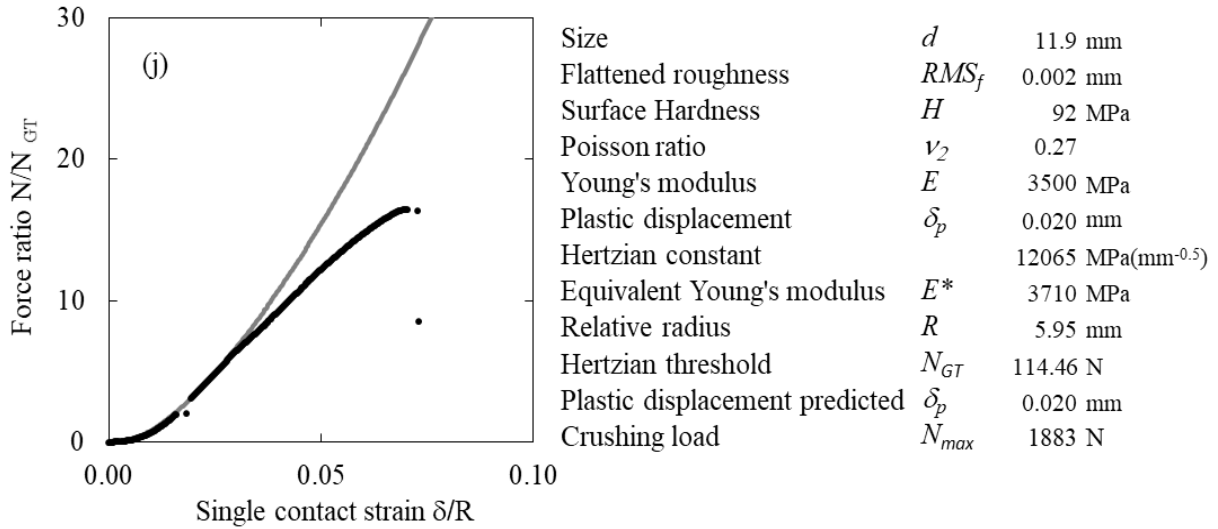


Fig. 5.18 (a)-(j) Uniaxial compression test on gypsum spheres

The average H value obtained for the spherical specimens from the Rockwell testing was 55 MPa whereas the curve fitting exercise obtained an average value of 80 MPa. For the cube specimens, the average H value was 63 MPa (Table 6. 5). The minimum value and maximum values of the H value for the 12 cubes tested ranged from 41 MPa – 81 MPa and the H values for spheres ranged from 43 MPa – 74 MPa. This shows that surface hardness for these particles is rather consistent regardless of the shape of the material tested. For a given relative radius R of contact, the factor influencing initial damage and plastic displacement before the onset of the Hertzian response for a given radius, R , is the ratio $(H/E)^2$ (Cavarretta, et al., 2012). For the gypsum spheres tested in this study, the computed values of $(H/E)^2$ varied from 6.9×10^{-4} to 1.4×10^{-3} MPa/MPa. The obtained values of $(H/E)^2$ were less than the values of 0.01 – 0.02 for natural sand (Cavarretta, et al., 2012); however, they are close to the reported values of $(H/E)^2$ for borosilicate glass ballotini of 4.5×10^{-4} . This may be the reason why the initial plastic behavior of the gypsum spheres was similar to the borosilicate glass ballotini even though the H values of the gypsum spheres were lower than the values of the borosilicate glass ballotini.

Table 5.4 Parameters influencing the deformation and response of gypsum specimens

Test	N_{max}	E	H	δ_{pm}	$(H/E)^2$
	(N)	(MPa)	(MPa)	(mm)	(MPa/Mpa)
Average	1853	2900	80	0.023	7.8E-04
Standard deviation	242	356	20	0.010	8.1E-04
Coefficient of variation	0.13	0.12	0.25	0.43	7.5E-04

Table 5.5 Rockwell hardness values

Shape	Average of distance yp after reloading (HR15Y) (μm)	Average H (MPa)	Average H from the fitting exercise
Cube	39	63	-
Sphere	30	55	80

5.5 Conclusions

Particle characterization of AM gypsum and photopolymer materials were conducted by testing for material properties such as Young's modulus, H, Poisson's ratio, inter-particle friction and surface roughness. While the measured shape factors are favorable when compared to the borosilicate ballotini and steel ball bearings previously used in DEM validation studies, the Young's modulus was significantly lower. Additionally, the inter-particle friction and surface roughness values were higher than those of the borosilicate glass ballotini and steel ball bearings. Even with an increased surface roughness and reduced young's modulus, the material still exhibited a Hertzian behavior, showing that the associated material is feasible for use in DEM validation studies. When conducting DEM simulations of the materials presented herein,

consideration should be given to the variability of the material properties, as well as the compressible nature of the material above a given stress threshold.

While only spherical particles were tested so that comparisons with glass ballotini and steel ball bearings could be made, the use of AM particles allows for significant advancement in physical laboratory testing in which geometric properties may be changed without changes to the associated material property changes. This will also allow for DEM simulations of more realistic particle shapes to be validated so that the results can be used with more confidence.

CHAPTER 6: CONCLUSIONS

6.1 Summary

The two primary objectives for this study were (1) to investigate the effect of boundary plates in direct shear testing of sand specimens and ball bearing specimens using laboratory testing and validated DEM simulations, and (2) to investigate the use of AM particles in experimentally validated DEM studies. For the first objective, laboratory testing was carried out on dense and loose specimens of Ottawa sand and steel ball bearings with a number of different boundary plates. The results of the dense ball bearing specimens with plates with no projections were further compared with simple DEM simulations with a high boundary friction value and a low boundary friction value, to examine the influence of boundary friction on the micromechanical behavior of the idealized granular material. The conclusions based on this comparison are the following:

1. Overall, for dense and loose sand specimens, the results showed that the R1.5 grid boundaries exhibited higher peak shear stress on average when compared to the specimens with other boundary types. Even though dense specimens of ball bearings with the R1.5 grid boundary exhibited slightly higher strength, this trend was not observed for the loose ball bearing specimens. For the dense ball bearing specimens, the specimens with the sawtooth boundary exhibited the lowest overall peak strength.
2. The shear stress-displacement response of the DEM specimens matched the shear stress-displacement behavior (i.e., initial low strain stiffness, and peak stress) of laboratory experiments conducted on dense ball bearings. However, the dilative responses of the DEM simulations and laboratory specimens and the amount of strain-softening differed,

which may be due to the fact that slight rotation of the top cap is allowed in the experiments but was not allowed in the simulations.

3. Comparisons of the DEM simulations of specimens with a boundary friction coefficient of 10.0 and a friction coefficient of 0.0 showed that the macro-scale response (i.e., initial stiffness and peak stress) of the specimens was similar. Although the strain-softening was delayed for the zero friction boundary specimen, it eventually resembled that of the high friction boundary specimen. Localized measurements inside the specimen also showed that there were not significant differences in the particle displacements, although the high friction boundary specimen had a greater number of strong contact force chains.

Localized differences in dilation were also noted within the measurement spheres.

For the second objective, AM particles were fabricated and then underwent a full characterization to examine their suitability as an analogue granular material. The conclusions based on the characterization are as follows:

4. Characterization of AM gypsum and photopolymer materials showed that the shape factors are comparable to the glass ballotini and steel ball bearings, whereas Young's modulus was significantly lower.
5. Inter-particle friction and surface roughness values were higher than those of the borosilicate glass ballotini and steel ball bearings. However, the material still exhibited a Hertzian behavior, showing that the both AM materials tested are likely viable for use in DEM validation experiments. However, care should be taken while conducting DEM simulations of the AM materials presented herein. Consideration should be given to the variability of the material properties, as well as the compressible nature of the material above a given stress threshold.

6. The use of AM particles allows for significant advancement in physical laboratory testing in which geometric properties may be changed without changes to the associated material property changes. This will also allow for DEM simulations of more realistic particle shapes to be validated so that the results can be used with more confidence.

A few points related to the original hypothesis of the research that *the use of suitable idealized granular material can lead to a better understanding of granular behavior in laboratory studies and in DEM validation studies* should also be made. While idealized materials were used in the laboratory study, it is clear that the results were not similar to that of the Ottawa sand, thus a more suitable idealized granular material should be used in the future if the goal is to replicate a natural sand or gravel material. Thus there is a need to develop these more suitable materials as shown in the second part of this study with the AM materials. The results from the DEM simulations on spheres and the experimental studies on the ball bearings agreed quite well which supports the hypothesis of the current research; however, little effect in the macro-scale and micro-scale responses were observed for the two different boundary friction cases. It is possible that the boundary friction has very little influence on the overall response, as suggested by some previous experimental studies, and that the rigid boundary movement is sufficient to force failure on the horizontal plane for dense specimens in direct shear tests.

Additionally, the boundaries with different geometric projections discussed in the experimental study were replicated in the DEM simulations. Based on the laboratory results, it appears that these projections make more of a difference in the behavior of sand (or more angular materials) and may have little effect on specimens of spherical particles. While the DEM simulations could be used to analyze this further, it would likely be more informative of natural granular material behavior if more complex particle shapes were examined in the DEM

simulations (since the ball bearings were not representative of the sand behavior in the first place). While these more complex DEM simulations are outside the scope of this study, the characterization of additive manufactured particles showed that a more suitable validation material can be generated and that they can be used for laboratory testing and simulations which serves as a step forward in the direction of using a novel material to recreate the particles for validating DEM simulations. Hence the characterization also supports the hypothesis. Therefore, while there are still many questions to be answered before the proposed hypothesis can be fully proven true, this study points to several of the limitations with the current idealized granular materials and validation studies and the need for implementation of more complex shapes in validated DEM studies to properly examine natural granular material behavior.

6.2 Recommendations for future work

The DEM models studied herein were only a simple comparison of the boundaries with no projections so that the influence of boundary friction could be examined. Additional models should be developed for consideration of the boundary types used in the experimental study and it is likely that these simulations should also consider more complex shapes in order to be more informative. Additional understanding of the particle motion near these boundaries can likely further explain some of the macro-scale response observations made for the Ottawa sand specimens.

The characterization study conducted in this research shows that the AM materials can be used in laboratory studies and DEM validation studies and that their Hertzian behavior can be modeled using the Hertz-Mindlin contact models in the simulations. Therefore, the effect of particle shape on the response of granular specimens can be investigated in the future using these AM materials. The models shown in this study can be extended to examine these more complex

shapes and laboratory testing in the large-scale direct shear device can be used to obtain the validation data needed. One additional consideration for future work is that the AM materials are significantly rougher than the steel ball bearings. Therefore, a roughness contact model can be developed for a comparison study with the Hertz-Mindlin contact model to investigate the model performance.

REFERENCES

- Alshibli, K. A., & Hasan, A. (2008). Spatial variation of void ratio and shear band thickness in sand using X-ray computed tomography. *Geotechnique*, 58(4), 249-257.
- ASTM D3080 (2012). Standard test method for direct shear test of soils under consolidated drained conditions. *ASTM International*, West Conshohocken, PA.
- ASTM D4253 (2014). Standard test methods for minimum index density and unit weight of soils and calculation of relative density. *ASTM International*, West Conshohocken, PA.
- Bagi, K. (1993). A quasi-static numerical model for micro-level analysis of granular assemblies. *Mechanics of Materials* 16(1–2), 101–110.
- Bagi, K. (2005). An algorithm to generate random dense arrangements for discrete element simulations of granular assemblies. *Granular Matter*, 7(1), 31-43.
- Bardet, J. P., & Proubet, J. (1991). Numerical investigation of the structure of persistent shear bands in granular media. *Geotechnique*, 41(4), 599-613.
- Barla, M., & Barla, G. (2005). Assessing design parameters for tunneling in a cemented granular soil by continuum and discontinuum modeling. In G. a. Barla (Ed.), *Analysis and Design in Geomechanical Applications, proceedings of the 11th International Conference*. 475-484.
- Barreto Gonzalez, D. (2009). *Numerical and experimental investigation into the behaviour of granular materials under generalised stress states*. Ph.D. thesis, University of London, Imperial College of Science, technology and Medicine, Department of Civil Engineering,, London.
- Bernhardt, M. L., Biscontin, G., & O'Sullivan, C. (2016). Experimental validation study of 3D direct simple shear DEM simulations. *Geotechnique* , 56 (3), 336-347.
- Bolton, M. D. (1986). The strength and dilatancy of sands. *Geotechnique*, 36 (1), 65-78.
- Bredt, J. F., Anderson, T. C., Russell, D. B. (1999). Patent No. US 6416850 B1. *Three-dimensional printing materials system*.
- Brinell, J. A. (1901). .: Brinell's method of determining hardness and their properties of iron and steel. ‘‘II. Cong. Int. Methodes d'Essai, Paris,’’(translated to English by A. Wahlberg). 59, 243-298.
- Cavarretta, I. (2009). *the influence of particle characteristics on the engineering behavior of granular materials*. London: Imperial College.
- Cavarretta, I., O'Sullivan, C., Ibrahim, E., Lings, M., & Hamlin, S. (2012). Characterization of artificial particles for DEM simulations. *Particuology*, 10 (2). 209-220

- Cerato, A. B., and Lutenecker, A., J. (2007): "Scale effects of shallow foundation bearing capacity on granular material." *Journal of Geotechnical and Geoenvironmental Engineering*, 133(10), 1192-1202.
- Coetzee, C. J., & Els, D. N. (2009). Calibration of granular material parameters for DEM. *Journal of Terramechanics*, 46, 15–26.
- Coop, M. R., Sorensen, K. K., Bodas Freitas, T. and Georgoutsos, G. (2004). Particle breakage during shearing of a carbonate sand. *Géotechnique* 54(3), 157–163.
- Cui, L. (2006). *Developing a virtual test environment for granular materials using discrete element modelling* (Doctoral dissertation, University College Dublin).
- Cui, L., & O'Sullivan, C. (2006). Exploring the macro and Micro- scale response of an idealized granular material in direct shear apparatus. *Géotechnique*, 56(7), 455-468.
- Cundall, P., & Strack, O. (1979). A discrete numerical model for granular assemblies. *Geotechnique*, 1(29), 47-65.
- Dabeet, A. (2014). *Discrete element modeling of direct simple shear response of granular soils and model validation using laboratory tests* (Doctoral dissertation, University of British Columbia).
- Di Renzo, A., & Di Maio, F. P. (2004). Comparison of contact-force models for the simulation of collisions in DEM-based granular flow codes. *Chemical engineering science*, 59(3), 525-541.
- Dounias, G. T. and Potts, D. M. (1993). Numerical analysis of drained direct and simple shear tests. *J. Geotech. Eng.*, 119 (12), 1870-1891.
- Feng, Y., Han, K., and Owen, D. (2003). Filling domains with disks: An advancing front approach. *International Journal for Numerical Methods in Engineering*, 56(5):699-731.
- Gibson, I., Rosen, D.W., Stucker, B., (2015). *Additive Manufacturing Technologies*, second ed., Springer, 138
- Hall, S. A., Bornert, M., Desrues, J., Pannier, Y., Lenoir, N., Viggiani, G., & Bésuelle, P. (2010). Discrete and continuum analysis of localised deformation in sand using X-ray μ CT and volumetric digital image correlation. *Géotechnique*, 60(5), 315.
- Hanor, A. H., Gan, Y., Revay, M., Airey, D. W., & Einay, I. (2016). 3D Printable Geomaterials. *Géotechnique* , 66 (4), 323-332.
- Hardin, B. (1985). Crushing of Soil Particles. *J. Geotech. Engrg.*, 0.1061/(ASCE)0733-9410(1985)111:10(1177), 1177-1192.
- Härtil, J., and Ooi, J. Y. (2008). Experiments and simulations of direct shear tests: porosity, contact friction and bulk friction. *Granular Matter*, 10(4), 263.

- Houlsby, G. T. (1991). *How the dilatancy of soils affects their behaviour*. Oxford: University of Oxford, Department of Engineering Science.
- Hryciw RD, Irsyam M (1993). Behavior of sand particles around rigid inclusions during shear. *Soils and Foundations*, Vol. 33(3), 1-13.
- Hull, C. W., (1984). Patent No. US 4575330 A, *Apparatus for production of three-dimensional objects by stereolithography*.
- Itasca (2002). *Itasca Manual, Theory and Backround*. Itasca, second edition.
- Itasca Consulting Group (2014). Particle Flow Code in Three Dimensions. Software Version 5.0.
- Iwashita, K. and Oda, M. (2000). Micro-deformation mechanism of shear banding process based on modified distinct element method. *Powder Technology*, 109, 192-205.
- Jaeger, H. (2014). “Granular matter by design”, *Jaeger lab*.
- Jewell, R. A. (1989). “Direct shear tests on sand.” *Geotechnique*, 39(2), 309–322.
- Jiang, Q., Feng, X., Song, L., Gong, Y., Zheng, H., & Cui, J. (2016). Modeling rock specimens through 3D printing: Tentative experiments and prospects. *Acta Mechanica Sinica*, 32(1), 101-111.
- Jodrey, W. and Tory, E. (1985). Computer simulation of close random packing of equal spheres. *Physical Review A*, 32(4), 2347-2351.
- Ju, Y., Xie, H., Zheng, Z., Lu, J., Mao, L., Gao, F., & Peng, R. (2014). Visualization of the complex structure and stress field inside rock by means of 3D printing technology. *Chinese science bulletin*, 59(36), 5354-5365.
- Liang, T., & Knappett, J. A. (2017). Centrifuge modelling of the influence of slope height on the seismic performance of rooted slopes. *Géotechnique*, 67(10), 855-869.
- Lings, M. L. & Dietz, M. S. (2004). An improved direct shear apparatus for sand. *Geotechnique* 54(4), 245-256.
- Mandl, G., De Jong, L. N. J., & Maltha, A. (1977). Shear zones in granular material. *Rock mechanics*, 9(2-3), 95-144.
- Masson, S. & Martinez, J. (2001). Micromechanical analysis of the shear behavior of a granular material. *ASCE J. Engng Mech.* 127(10), 1007–1016.
- McDowell G.R., Bolton M.D., Robertson D. (1996). “The fractal crushing of granular materials.” *Journal of the Mechanics and Physics of Solids*, Volume 44, Issue 12, December 1996, 2079-2101.
- Miskin, M. Z. & Jaeger, H. M. (2013). Adapting granular materials through artificial evolution. *Nature Mater.* 12(4), 326–331.

- Ni, Q., Powrie, W., Zhang, X., and Harkness, R. (2000). "Effect of particle properties on soil behaviour: 3-D numerical modelling of shear box tests." *In Geotechnical special publication, American Society of Civil Engineering, USA.* 58–70.
- Osinga, S., Zambrano-Narvaez, G., & Chalaturnyk, R. J. (2015, November). Study of geomechanical properties of 3D printed sandstone analogue. *In 49th US Rock Mechanics/Geomechanics Symposium.* American Rock Mechanics Association.
- O'Sullivan, O. (2011). "*Particulate Discrete Element Modeling.*" Spoon Press/Taylor & Francis, New York, NY.
- O'Sullivan, C. (2002). "*The application of discrete element modelling to finite deformation problems in geomechanics.*" Ph.D. thesis, University of California, Berkeley.
- O'Sullivan, C. (2002). "*The application of discrete element modelling to finite deformation problems in geomechanics.*" Ph.D. thesis, University of California, Berkeley.
- O'Sullivan, C., & Cui, L. (2009). Micromechanics of granular material response during load reversals: combined DEM and experimental study. *Powder Technology*, 193(3), 289-302.
- Palmeira, E. M., and Milligan, G. W. E., (1989) Scale effects in direct shear tests in sand. *Proceedings of 12th International Conference on Soil Mechanics and Foundation engineering*, 1(1), 739-742.
- Parsons JD (1936) Progress on report on an investigation of the shearing resistance of cohesionless soils, *Proceedings of 1st international conference on Soil Mechanics and Foundation engineering*, 2, 133-138.
- Pavlina, E. J., & Van Tyne, C. J. (2008). Correlation of yield strength from hardness measurements. *17* (6), 888-893.
- Polito, C., Green, R. A., Dillon, E., & Sohn, C. (2013). Effect of load shape on relationship between dissipated energy and residual excess pore pressure generation in cyclic triaxial tests. *Canadian Geotechnical Journal*, 50(11), 1118-1128.
- Potts, D. M., Dounias, G. T., and Vaughan, P. R. (1987). Finite element analysis of the direct shear box test. *Geotechnique*, 37(1), 11–23.
- Potyondy, D. O., and P. A. Cundall. (2004). A bonded-particle model for rock. *International journal of rock mechanics and mining sciences*, 41(8), 1329-1364.
- Roubtsova, V., Chekired, M., Morin B., & Karray, M. (2011). "3D virtual laboratory for geotechnical applications: Another perspective". *In Particles 2011, II International Conference on Particle-based Methods Fundamentals and Applications*, Barcelona, Spain, October 26–28, 2011.
- Sachs, E., Cima, M., Williams, P., Brancazio, D. and Cornie, J. (1992). Three-dimensional printing: rapid tooling and prototypes directly from a CAD model. *Journal of Manufacturing Science and Engineering*, 114(4), 481-488.

- Shibuya, S., Mitachi, T., and Tamate, S. (1997). Interpretation of direct shear box testing of sands as quasi-simple shear. *Geotechnique*, 47(4), 769–790.
- Tabor, D. (1970). The hardness of solids. *Review of Physics in Technology*. 1 (3), 145.
- Taylor, D. W. (1948). *Fundamentals of soil mechanics*. New York: John Wiley & Sons
- Thornton, C. (2000). “Numerical simulations of deviatoric shear deformation of granular media.” *Geotechnique* 50, 43–53.
- Thornton, C., & Yin, K. K. (1991). Impact of elastic spheres with and without adhesion. *Powder technology*, 65(1-3), 153-166.
- Thornton, C., and L. Zhang (2003). Numerical simulations of the direct shear test. *Chemical Engineering and Technology*, 26, 153-156.
- Uesugi M and Kishida H (1986). Influential factors of friction between steel and dry sands. *Soils and Foundations*, 26(2), 33-46.
- Uesugi M, Kishida H and Tsubakihara Y (1988). Behavior of sand particles in sand steel friction. *Soils and Foundations*, 28(1), 107-118.
- Vardoulakis, I. (1980). Shear band inclination and shear modulus of sand in biaxial tests. *International Journal for Numerical and Analytical Methods in Geomechanics*, 4(2), 103-119.
- Wang J, and Jiang M (2011). Unified soil behavior of interface shear test and direct shear test under the influence of lower moving boundaries. *Granular matter*, Vol. 13, No. 5, 631–641.
- Wang, J. and Gutierrez, M. (2010). Discrete element simulation of direct shear specimen scale effects. *Geotechnique*, 60(5), 395-409.
- Wang, J., Dove, J. E. and Gutierrez, M. S. (2007c). Determining particulate–solid interphase strength using shear-induced anisotropy. *Granular Matter* 9, Nos 3–4, 231–240.
- Watters, M. Kittu A. and Bernhardt ML, (2017) Additive manufactured materials as analog soils in geotechnical laboratory testing” (Under review)
- Watters, M. P. (2017). *Feasibility of Additive Manufactured Materials for Use in Geotechnical Laboratory Testing Applications*, University of Arkansas, Fayetteville.
- Watters, M. P., & Bernhardt, M. L. (2017). Modified curing protocol for improved strength of binder-jetted 3D parts. *Rapid Prototyping Journal*, 23(6), 1195-1201.
- Watters, M. P., & Bernhardt, M. L. (2018). Curing parameters to improve the mechanical properties of stereolithographic printed specimens. *Rapid Prototyping Journal*, 24(1), 46-51.

- Wroth, C. P. (1958) *The behaviour of soils and other granular media when subjected to shear*. Ph. D. dissertation, Univ. of Cambridge, Cambridge, UK.
- Yan, Y. and Ji, S. (2009). "Discrete element modeling of direct shear tests on granular material.", *International Journal for Numerical and Analytical Methods in Geomechanics*, vol. 34(9), 978-990.
- Zhang, L. & Thornton, C. (2002). DEM simulations of the direct shear test. *Proc. 15th ASCE Engng Mech. Conf.*, New York, CD-rom
- Zhang, L. and Thornton, C. (2007). "A numerical examination of the direct shear test." *Géotechnique*, 57(4), 343-354.
- Zhang, P., Li, S. X., & Zhang, Z. F. (2011). General relationship between strength and hardness. 2 (7), 62-73.
- Zhu, H. P., Zhou, Z. Y., Yang, R. Y., & Yu, A. B. (2007). Discrete particle simulation of particulate systems: theoretical developments. *Chemical Engineering Science*, 62(13), 3378-3396.

Appendix A. AM Material characterization data

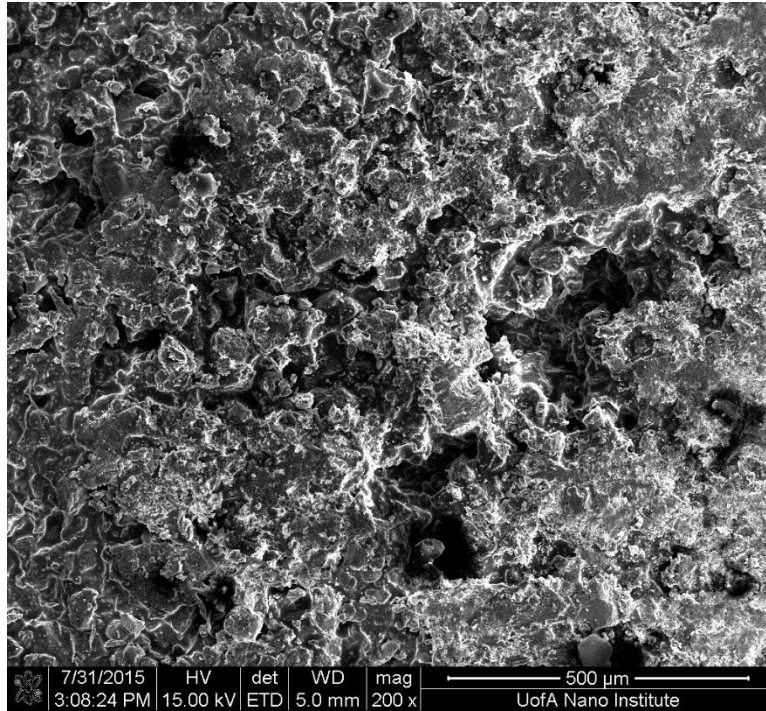


Fig. A.1 SEM image of 10 mm diameter gypsum sphere.

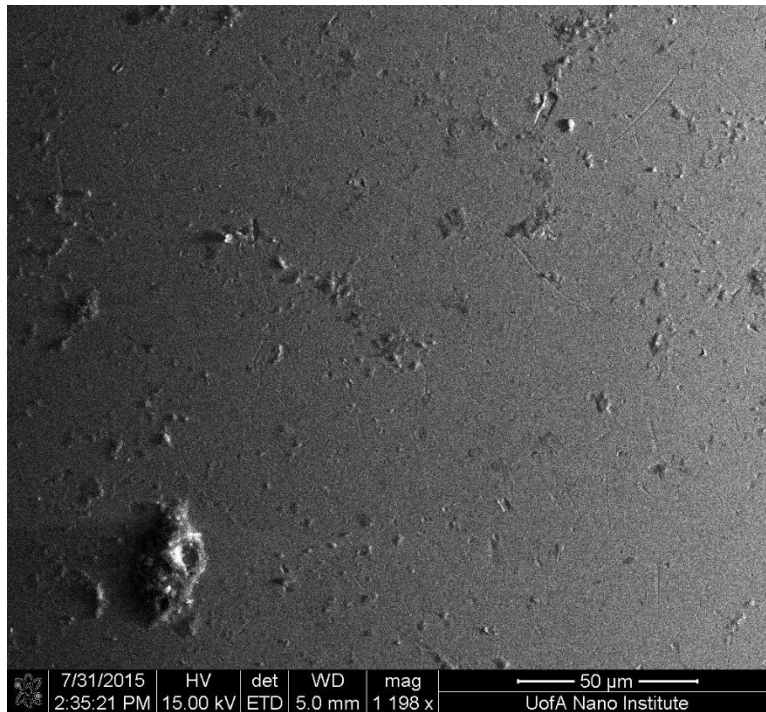


Fig. A.2 SEM image of steel ball bearing

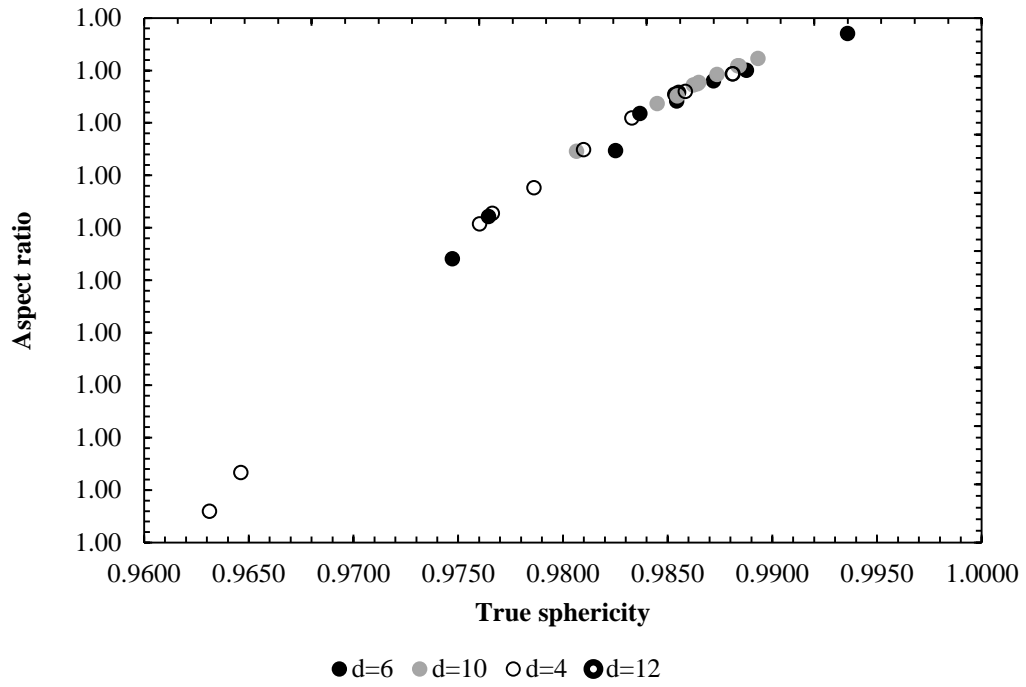


Fig. A.3 Aspect ratio and True sphericity variation of gypsum sphere.

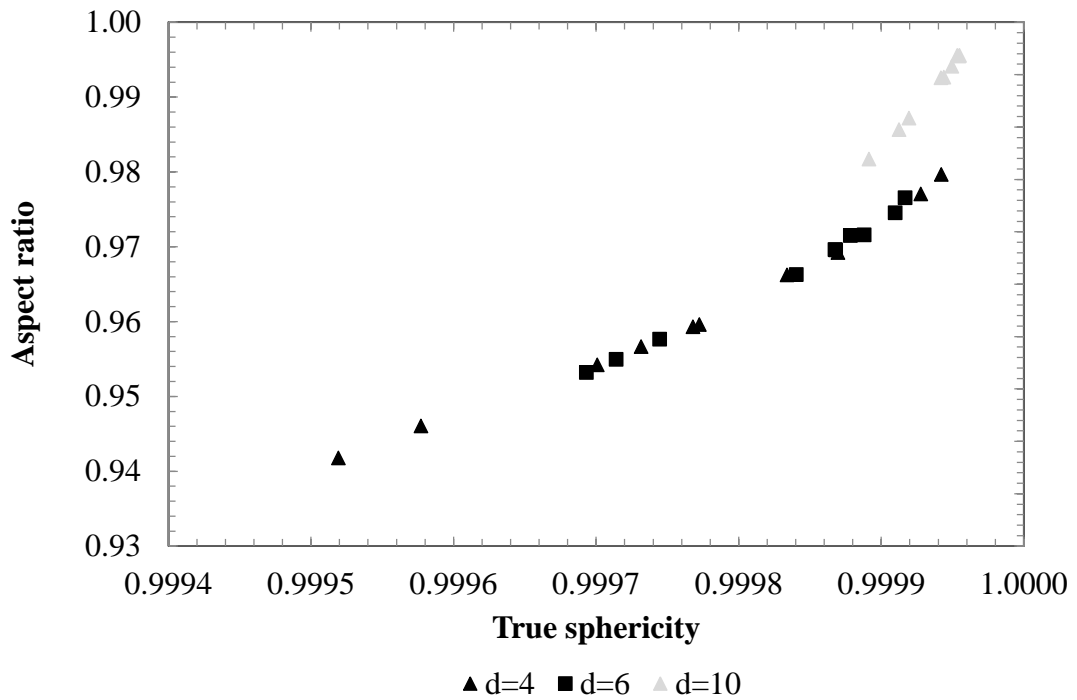


Fig. A.4 Aspect ratio and True sphericity variation of photopolymer sphere.

Table A.1 Post shear surface roughness of gypsum and photopolymer material from confocal microscope for a scan area 50 μm x 50 μm

Material	Diameter	Ra	Ra (flattened)
Gypsum	4	2.90	1.82
Photopolymer	10	3.11	2.44

Table A.2 Post shear surface roughness of gypsum and photopolymer material from interferometer for a scan area 50 μm x 50 μm

Specimen	Diameter	Ra	Ra (flattened)
		μm	μm
Gypsum	4	2.756	1.416
	6		
	10	1.973	0.224
Photopolymer	4	0.619	0.249
	6	2.077	0.802
	10	2.415	1.126

Table A.3 Diameter and aspect ratios of gypsum spheres used in the hardness test

Specimen	d _a	d _b	d _c	d _d	d ₁	d ₂	d ₃	d _{average}	volume	mass	density	aspect ratio
	mm	mm	mm	mm	mm	mm	mm	mm	cm ³	g	g/cm ³	
1	11.8	12	12.1	12	12.1	12	11.8	11.98	0.901	1.49	1.657	0.976
2	12.2	12	12.2	12.1	12.2	12.1	12	12.09	0.926	1.52	1.639	0.988
3	12.1	12.2	12.1	12.2	12.2	12.1	12.1	12.13	0.935	1.52	1.624	0.987
4	12.2	12.2	12	12.1	12.2	12.1	12	12.11	0.929	1.53	1.651	0.986
5	12	12.1	12.1	12.2	12.2	12.1	12	12.08	0.922	1.5	1.621	0.985
6	12.3	12	12	12.2	12.3	12.2	12	12.13	0.934	1.51	1.619	0.978
7	12.1	12.2	12.1	11.9	12.2	12.1	11.9	12.04	0.915	1.51	1.646	0.981
8	12.2	12.1	12	12.1	12.2	12.1	12	12.09	0.924	1.52	1.647	0.988
9	12.2	12	12.2	12.2	12.2	12.2	12	12.12	0.933	1.51	1.619	0.985
10	11.9	11.8	11.8	12	12	11.9	11.8	11.9	0.883	1.46	1.656	0.983

Table A.4 Crushing load details and hardness of gypsum spheres

Test	Crushing Load	Young's modulus	Hardness	Plastic Displacement
	N	MPa	MPa	mm
1	1988	2400	55	0.015
2	1951	3000	110	0.04
3	1900	3300	85	0.02
4	2068	2900	89	0.028
5	1840	2800	103	0.04
6	1924	3200	82	0.02
7	1194	2500	65	0.02
8	1953	2600	64	0.018
9	1833	2800	52	0.01
10	1883	3500	92	0.02

Table A.5 Shape parameter calculation for 4 mm gypsum specimen

Diameter (mm)			Aspect Ratio AR i.e. Sphericity S_{KS}	True Sphericity ⁽⁰⁾ Ψ	Cross section area on principal planes (mm ²)			Cross section perimeters ⁽¹⁾ on principal planes (mm)			2D Circularity			(mean) Circularity
d1	d2	d3	AR	Ψ	1;2	1;3	2;3	1;2	1;3	2;3	C_{12}	C_{13}	C_{23}	
4.19	4.16	4.12	0.98	1.00	13.69	13.56	13.46	13.12	13.05	13.01	1.00	1.00	1.00	1.00
4.24	4.20	4.18	0.99	1.00	13.99	13.92	13.79	13.26	13.23	13.16	1.00	1.00	1.00	1.00
4.21	4.18	4.12	0.98	1.00	13.82	13.62	13.53	13.18	13.09	13.04	1.00	1.00	1.00	1.00
4.17	4.12	4.07	0.98	1.00	13.49	13.33	13.17	13.02	12.94	12.87	1.00	1.00	1.00	1.00
4.34	4.26	4.18	0.96	1.00	14.52	14.25	13.99	13.51	13.38	13.26	1.00	1.00	1.00	1.00
4.28	4.23	4.18	0.98	1.00	14.22	14.05	13.89	13.37	13.29	13.21	1.00	1.00	1.00	1.00
4.20	4.16	4.15	0.99	1.00	13.72	13.69	13.56	13.13	13.12	13.05	1.00	1.00	1.00	1.00
4.24	4.17	4.09	0.96	1.00	13.89	13.62	13.40	13.21	13.09	12.98	1.00	1.00	1.00	1.00
4.21	4.20	4.16	0.99	1.00	13.89	13.76	13.72	13.21	13.15	13.13	1.00	1.00	1.00	1.00
4.21	4.18	4.13	0.98	1.00	13.82	13.66	13.56	13.18	13.10	13.05	1.00	1.00	1.00	1.00
Min dia		Max dia	Avg.	Avg.										Avg
4.07		4.34	0.98	1.00										1.00

Table A.6 Shape parameter calculation for 6 mm gypsum specimen

Diameter (mm)			Aspect Ratio AR i.e. Sphericity S_{KS}	True Sphericity ⁽⁰⁾	Cross section area on principal planes (mm ²)			Cross section perimeters ⁽¹⁾ on principal planes (mm)			2D Circularity			(mean) Circularity
d1	d2	d3	AR	Ψ	1;2	1;3	2;3	1;2	1;3	2;3	C_{12}	C_{13}	C_{23}	
6.05	6.09	6.14	0.99	1.00	28.94	29.18	29.37	19.07	19.15	19.21	1.00	1.00	1.00	1.00
6.19	6.18	6.29	0.98	1.00	30.04	30.58	30.53	19.43	19.60	19.59	1.00	1.00	1.00	1.00
6.22	6.29	6.37	0.98	1.00	30.73	31.12	31.47	19.65	19.78	19.89	1.00	1.00	1.00	1.00
6.23	6.22	6.16	0.99	1.00	30.43	30.14	30.09	19.56	19.46	19.45	1.00	1.00	1.00	1.00
6.25	6.21	6.22	0.99	1.00	30.48	30.53	30.34	19.57	19.59	19.53	1.00	1.00	1.00	1.00
6.23	6.25	6.17	0.99	1.00	30.58	30.19	30.29	19.60	19.48	19.51	1.00	1.00	1.00	1.00
6.13	6.07	6.03	0.98	1.00	29.22	29.03	28.75	19.16	19.10	19.01	1.00	1.00	1.00	1.00
6.33	6.17	6.28	0.97	1.00	30.67	31.22	30.43	19.64	19.81	19.56	1.00	1.00	1.00	1.00
6.22	6.18	6.13	0.99	1.00	30.19	29.95	29.75	19.48	19.40	19.34	1.00	1.00	1.00	1.00
6.18	6.16	6.09	0.99	1.00	29.90	29.56	29.46	19.38	19.27	19.24	1.00	1.00	1.00	1.00
Min dia	Max dia		Avg.	Avg.										Avg
6.03	6.37		0.98	1.00										1.00

Table A.7 Shape parameter calculation for 10 mm gypsum specimen

Diameter (mm)			Aspect Ratio AR i.e. Sphericity S_{KS}	True Sphericity Ψ	Cross section area on principal planes (mm ²)			Cross section perimeters ⁽¹⁾ on principal planes (mm)			2D Circularity			(mean) Circularity
d1	d2	d3	AR	Ψ	1;2	1;3	2;3	1;2	1;3	2;3	C ₁₂	C ₁₃	C ₂₃	
10.36	10.29	10.22	0.99	1.00	83.73	83.16	82.60	32.44	32.33	32.22	1.00	1.00	1.00	1.00
10.36	10.31	10.24	0.99	1.00	83.89	83.32	82.92	32.47	32.36	32.28	1.00	1.00	1.00	1.00
10.17	10.1	10.03	0.99	1.00	80.67	80.11	79.56	31.84	31.73	31.62	1.00	1.00	1.00	1.00
10.33	10.24	10.17	0.98	1.00	83.08	82.51	81.79	32.31	32.20	32.06	1.00	1.00	1.00	1.00
10.32	10.27	10.17	0.99	1.00	83.24	82.43	82.03	32.34	32.19	32.11	1.00	1.00	1.00	1.00
10.32	10.26	10.18	0.99	1.00	83.16	82.51	82.03	32.33	32.20	32.11	1.00	1.00	1.00	1.00
10.3	10.24	10.18	0.99	1.00	82.84	82.35	81.87	32.26	32.17	32.08	1.00	1.00	1.00	1.00
10.34	10.24	10.14	0.98	1.00	83.16	82.35	81.55	32.33	32.17	32.01	1.00	1.00	1.00	1.00
10.3	10.25	10.19	0.99	1.00	82.92	82.43	82.03	32.28	32.19	32.11	1.00	1.00	1.00	1.00
10.29	10.23	10.16	0.99	1.00	82.68	82.11	81.63	32.23	32.12	32.03	1.00	1.00	1.00	1.00
Min dia	Max dia	Avg.	Avg.	Avg.										Avg
10.03		10.36	0.99	1.00										1.00

Table A.9 Shape parameter calculation for 4 mm photopolymer specimen

	Diameter (mm)			Aspect Ratio AR i.e. Sphericity	True Sphericity ⁽⁰⁾	Cross section area on principal planes (mm ²)			Cross section perimeters ⁽¹⁾ on principal planes (mm)			2D Circularity			(mean) Circularity
	d1	d2	d3	S _{KS}	□	1;2	1;3	2;3	1;2	1;3	2;3	C12	C13	C23	
				AR											
	3.93	3.86	3.77	0.96	1.00	11.91	11.64	11.43	12.24	12.10	11.99	1.00	1.00	1.00	1.00
	3.95	3.84	3.72	0.94	1.00	11.91	11.54	11.22	12.24	12.05	11.88	1.00	1.00	1.00	1.00
	3.93	3.86	3.75	0.95	1.00	11.91	11.57	11.37	12.24	12.07	11.96	1.00	1.00	1.00	1.00
	3.89	3.75	3.68	0.95	1.00	11.46	11.24	10.84	12.00	11.89	11.67	1.00	1.00	1.00	1.00
	3.9	3.84	3.78	0.97	1.00	11.76	11.58	11.40	12.16	12.06	11.97	1.00	1.00	1.00	1.00
	3.92	3.87	3.83	0.98	1.00	11.91	11.79	11.64	12.24	12.17	12.10	1.00	1.00	1.00	1.00
	3.93	3.9	3.85	0.98	1.00	12.04	11.88	11.79	12.30	12.22	12.17	1.00	1.00	1.00	1.00
	3.96	3.87	3.8	0.96	1.00	12.04	11.82	11.55	12.30	12.19	12.05	1.00	1.00	1.00	1.00
	3.92	3.81	3.75	0.96	1.00	11.73	11.55	11.22	12.14	12.05	11.88	1.00	1.00	1.00	1.00
	3.85	3.81	3.72	0.97	1.00	11.52	11.25	11.13	12.03	11.89	11.83	1.00	1.00	1.00	1.00
	Min dia	Max dia		Avg.	Avg.										Avg.
	3.68	3.96		0.96	1.00										1.00

Table A.10 Shape parameter calculation for 6 mm photopolymer specimen

			Aspect Ratio AR i.e. Sphericity S_{KS}	True Sphericity ⁽⁰⁾	Cross section area on principal planes (mm ²)			Cross section perimeters ⁽¹⁾ on principal planes (mm)			2D Circularity			(mean) Circularity	
d1	d2	d3	AR	Ψ	1;2	1;3	2;3	1;2	1;3	2;3	C ₁₂	C ₁₃	C ₂₃		
5.89	5.83	5.74	0.97	1.00	26.97	26.55	26.28	18.41	18.27	18.17	1.00	1.00	1.00	1.00	
5.99	5.83	5.72	0.95	1.00	27.43	26.91	26.19	18.57	18.40	18.14	1.00	1.00	1.00	1.00	
5.92	5.86	5.74	0.97	1.00	27.25	26.69	26.42	18.50	18.32	18.22	1.00	1.00	1.00	1.00	
5.91	5.79	5.73	0.97	1.00	26.88	26.60	26.06	18.38	18.29	18.10	1.00	1.00	1.00	1.00	
5.96	5.83	5.79	0.97	1.00	27.29	27.10	26.51	18.52	18.46	18.25	1.00	1.00	1.00	1.00	
5.96	5.82	5.85	0.98	1.00	27.24	27.38	26.74	18.50	18.55	18.33	1.00	1.00	1.00	1.00	
5.93	5.85	5.73	0.97	1.00	27.25	26.69	26.33	18.50	18.32	18.19	1.00	1.00	1.00	1.00	
5.98	5.88	5.81	0.97	1.00	27.62	27.29	26.83	18.63	18.52	18.36	1.00	1.00	1.00	1.00	
5.9	5.74	5.65	0.96	1.00	26.60	26.18	25.47	18.28	18.14	17.89	1.00	1.00	1.00	1.00	
5.98	5.84	5.7	0.95	1.00	27.43	26.77	26.14	18.57	18.35	18.13	1.00	1.00	1.00	1.00	
Min dia	Max dia		Avg.	Avg.											Avg.
5.65	5.99		0.97	1.00											1.00

Table A.11 Shape parameter calculation for 10 mm photopolymer specimen

			Aspect Ratio AR i.e. Sphericity S_{KS}	True Sphericity ⁽⁰⁾	Cross section area on principal planes (mm ²)			Cross section perimeters ⁽¹⁾ on principal planes (mm)			2D Circularity			(mean) Circularity
d1	d2	d3	AR	Ψ	1;2	1;3	2;3	1;2	1;3	2;3	C ₁₂	C ₁₃	C ₂₃	
9.88	9.77	9.68	0.98	1.00	75.81	75.11	74.28	30.87	30.73	30.55	1.00	1.00	1.00	1.00
9.93	9.79	9.69	0.98	1.00	76.35	75.57	74.51	30.98	30.82	30.60	1.00	1.00	1.00	1.00
9.87	9.79	9.69	0.98	1.00	75.89	75.12	74.51	30.88	30.73	30.60	1.00	1.00	1.00	1.00
9.88	9.79	9.69	0.98	1.00	75.97	75.19	74.51	30.90	30.74	30.60	1.00	1.00	1.00	1.00
9.84	9.77	9.64	0.98	1.00	75.51	74.50	73.97	30.80	30.60	30.49	1.00	1.00	1.00	1.00
9.9	9.84	9.79	0.99	1.00	76.51	76.12	75.66	31.01	30.93	30.83	1.00	1.00	1.00	1.00
9.89	9.76	9.64	0.97	1.00	75.81	74.88	73.90	30.87	30.68	30.47	1.00	1.00	1.00	1.00
9.9	9.8	9.72	0.98	1.00	76.20	75.58	74.81	30.94	30.82	30.66	1.00	1.00	1.00	1.00
9.97	9.84	9.69	0.97	1.00	77.05	75.88	74.89	31.12	30.88	30.68	1.00	1.00	1.00	1.00
9.91	9.85	9.73	0.98	1.00	76.67	75.73	75.27	31.04	30.85	30.76	1.00	1.00	1.00	1.00
Min dia		Max dia	Avg.	Avg.										Avg.
9.64		9.97	0.98	1.00										1.00

CURRICULUM VITAE

EDUCATION

Master of Science (December 2013)

Major: Civil Engineering, Oklahoma State University, Stillwater

Thesis - "Surface energy characteristics of granite and limestone aggregates with respect to 2D and 3D surface roughness measurements"

Bachelor of Technology, (May 2007)

Major: Civil Engineering, Mahatma Gandhi University, India

PROFESSIONAL EXPERIENCE

Graduate Research Assistant (May 2014 – October 2017)

Department of Civil Engineering, University of Arkansas, Fayetteville.

Graduate Research Assistant (January 2012 – December 2013)

Department of Civil and Environmental Engineering, Oklahoma State University, Stillwater.

Civil Engineer (July 2009 – March 2010)

EKK & Co Private Limited., Kerala, India (Project: Upgradation of Roads for Thrissur Corporation)

Civil Engineer (December 2008 – June 2009)

Roman Tarmat Limited, Kerala, India (Project: Recarpeting of runway and related pavement upgradation work)

Senior Planning Engineer (August 2007 – December 2008)

Sobha Developers Limited, Karnataka, India (Projects: Sobha Corporate Office, Sobha Beryl I&II and Sobha Daffodil)

PUBLICATIONS/PRESENTATIONS

Kittu, A., Watters, M., Cavarretta, I., and Bernhardt, M.L. "Characterization of 3D printed particles for DEM validation studies" (Under preparation)

Kittu, A., Eskew, J., and Bernhardt, M. L. "Experimental evaluation of the influence of direct shear boundary types on granular material response" (submitted)

Kittu A., Eskew, J., and Bernhardt, M. L. "Effects of common boundary types in direct shear testing" (GeoFrontiers, 2017)

Kittu, A., R. Bulut, and S. Harimkar. "Comparison of contact angle measurements on granite with respect to surface roughness" (International Journal of Pavements, 2013)

Kittu A., R. Bulut and S. Harimkar. "Comparison of surface energy values of limestone with respect to different 3D surface roughness measurements" (GeoShanghai International Conference 2014, China)

Kittu A., R. Bulut and J. Puckette, "Effects of surface roughness on contact angle measurements on a limestone aggregate" (Geohubei International Conference 2014, China)